AGH University of Krakow

FIELD OF SCIENCE ENGINEERING AND TECHNOLOGY

SCIENTIFIC DISCIPLINE MATERIALS ENGINEERING

DOCTORAL THESIS

Corrosion resistance of coated and uncoated biodegradable magnesium alloys

Mgr Iryna Kozina

supervisor: prof. dr hab. Halina Krawiec

AGH University of Krakow, Faculty of Foundry Engineering, Department of Chemistry and Corrosion of Metals

Kraków, 2024

Akademia Górniczo-Hutnicza im. Stanisława Staszica w Krakowie

DZIEDZINA NAUK INŻYNIERYJNO-TECHNICZNYCH
DYSCYPLINA INŻYNIERIA MATERIAŁOWA

ROZPRAWA DOKTORSKA

Odporność korozyjna pokrytych i niepokrytych powłokami biodegradowalnych stopów magnezu

Autor: Mgr Iryna Kozina

Promotor rozprawy: prof. dr hab. Halina Krawiec

Praca wykonana: Akademia Górniczo-Hutnicza im. Stanisława Staszica w Krakowie,
Wydział Odlewnictwa, Katedra chemii i korozji metali

Kraków, 2024

Acknowledgements:

The author would like to thanks to European Commission for financial support in the frame of project H2020-MSCA-ITN-2017, grant agreement no. 764977 –mCBEEs, and AGH University of Krakow subsidy grant number 16.16.170.654.

Horizon 2020
European Union Funding
for Research & Innovation

mCBEEs

Contents

Chapter III Surface Modification Techniques Used for Biomedical Mg Alloys…………………47

Chapter IV Surface Modification of Mg alloys by Using Biopolymer Coatings………….…….66

Corrosion resistance of coated and uncoated biodegradable magnesium alloys

Abstract

In recent years, magnesium alloys have been intensively investigated for possible applications as biodegradable implants. The main limitation of the use of magnesium alloys as implants is their rapid corrosion in physiological solutions. The main goal of this research was to investigate the corrosion mechanism of uncoated and coated Mg20Zn and Mg19Zn1Ca alloys. Chitosan-based coatings were chosen as a natural material to slow down the corrosion rate. Moreover, the antibacterial properties of chitosan played an important role in selecting the coating materials. To enhance the corrosion resistance of magnesium alloys in Hanks' solution, different types of chitosan – based coatings were used.

Corrosion tests revealed that the chitosan-based coatings such as chitosan/TiO_2, chitosan_WG (chitosan with addition of Na_2SiO_3 and water glass), Ca-P and the double layer coating Ca-P/chitosan_WG significantly reduced the corrosion rate of magnesium alloys in Hanks' solution. Because of their interaction with the amine groups present in the chitosan molecules, the TiO_2 nanoparticles were uniformly distributed in the polymer matrix. The chitosan/TiO_2 coating limited the contact of the magnesium alloy with Hanks' solution and limited its corrosion. The best corrosion protection is provided by the double layer coating Ca-P/chitosan_WG. During the deposition of chitosan_WG on the Ca-P coating, insoluble calcium silicate ($CaSiO_3$) is formed. This compound forms a barrier layer on the surface of the Mg alloy and protects its against corrosion. Generally, the corrosion of bare magnesium alloys is caused by dissolution of the matrix and deposition of corrosion products on their surface. In the case of coated alloys, the coating undergoes degradation, the alloy is dissolved, and corrosion products are deposited on the electrode surface.

The modification of the chitosan coating with the addition of silver nanoparticles (NPs) and ZnO (NPs) improved the corrosion resistance of Mg19Zn1Ca. Moreover, these coatings exhibited a slight antibacterial property. The coating chitosan/Ag(NPs) exhibited an antibacterial effect against the *Escherichia coli* (E. C.) and *Staphylococcus aureus* (S. A.) bacteria.

Streszczenie

W ostatnich latach, stopy magnezu były intensywnie badane pod kątem ich możliwych zastosowań jako biodegradowalne implanty. Jednak, szybka korozja magnezu i jego stopów w roztworach fizjologicznych ogranicza ich zastosowanie jako implanty. Głównym celem pracy doktorskiej było zbadanie mechanizmu korozji niepowlekanych i powlekanych stopów Mg20Zn i Mg19Zn1Ca. Aby zwiększyć odporność na korozję stopów magnezu w roztworze Hanka, zastosowano różne rodzaje powłok na bazie chitozanu. Powłoki na bazie chitozanu zostały wybrane jako naturalny materiał polimerowy spowalniający szybkość korozji stopów magnezu. Co więcej, właściwości antybakteryjne chitozanu odegrały ważną rolę w wyborze materiałów powłokowych.

Testy korozyjne wykazały, że powłoki na bazie chitozanu, takie jak chitozan/TiO_2, chitozan_WG (chitozan z dodatkiem Na_2SiO_3 i szkła wodnego), Ca-P i dwuwarstwowa powłoka Ca-P/chitozan_WG znacznie zmniejszyły szybkość korozji stopów magnezu w roztworze Hanka. Ze względu na interakcję z grupami aminowymi obecnymi w cząsteczkach chitozanu, nanocząstki TiO_2 były równomiernie rozmieszczone w matrycy polimerowej. Powłoka chitozan/TiO_2 ograniczyła kontakt stopu magnezu z roztworem Hanka oraz spowolniła jego korozję. Najlepszą ochronę antykorozyjną zapewnia dwuwarstwowa powłoka Ca-P/chitosan_WG. Podczas osadzania warstwy chitozanu zawierającej szkło wodne i Na_2SiO_3 (chitozan_WG) na powłoce Ca-P, powstaje nierozpuszczalny krzemian wapnia ($CaSiO_3$). Związek ten tworzy warstwę barierową na powierzchni stopu magnezu i chroni go przed korozją. Zasadniczo, korozja stopów magnezu jest spowodowana rozpuszczaniem osnowy i osadzaniem się produktów korozji na ich powierzchni. W przypadku stopów pokrytych powłokami, powłoka ulega degradacji, stop jest rozpuszczany, a produkty korozji osadzają się na jego powierzchni.

Modyfikacja powłoki chitozanowej z dodatkiem nanocząstek srebra (NPs) i ZnO (NPs) poprawiła odporność na korozję stopu Mg19Zn1Ca. Ponadto, powłoki te wykazywały niewielkie właściwości antybakteryjne. Powłoka chitozanu zawierająca nanocząstki srebra Ag(NPs) wykazywała działanie antybakteryjne wobec bakterii *Escherichia coli* (E. C.) i *Staphylococcus aureus* (S. A.).

Introduction

In recent years, much attention has been paid to investigating bioresorbable, biodegradable implant materials to connect broken bones. Though in earlier times most bone diseases were associated primarily with elderly people, nowadays the problem comes up without respect for age difference and is occurring increasingly frequently among the younger generation. Therefore, creating a natural biodegradable implant material for orthopedics has become a new challenge. Magnesium and its alloys are one of the most promising biodegradable implant materials to connect broken bones or to promote bone-healing effects. Magnesium exhibits a Young's modulus which is close to that of human bones, and magnesium's density is near bone values. Moreover, magnesium takes part in many processes in the human body. Magnesium is neither toxic nor an allergic material, it has no negative influence on the human body, instead having positive effects. However, like many other bone implant materials, this metal has different characteristics which need to be improved. The main issue with magnesium and its alloys is its rapid corrosion rate in physiological solutions. The challenge is to slow down the corrosion process while avoiding completely stopping the process. The idea of the material under study is for the implant to dissolve after its healing effect has run its course and for it to be excreted from the human body naturally, avoiding a second surgery.

Magnesium is a very reactive metal, especially in aggressive environments rich in chloride ions. There are a few ways to improve these materials for implant applications, namely with the addition of alloying elements and with coating applications. This work has chosen two alloys to study – Mg20Zn binary alloy and Mg19Zn1Ca ternary alloy. The addition of Zn to alloys increases the corrosion resistance of the magnesium. The presence of a small amount of Ca causes the refinement of the microstructure. Moreover, Zn and Ca influence the improvement of the mechanical properties of the magnesium alloys. Both metals are body friendly, as is magnesium, and are active participants in the human organism's life processes.

Chitosan-based coatings are an attractive option for the corrosion protection of magnesium alloys due to their natural origin and range of properties: biocompatibility, biodegradability, osteoconductivity, antimicrobial properties, non-toxicity, and hypoallergenic nature. The addition of inorganic compounds to chitosan coatings influences their microstructure and adhesion properties. Moreover, this increases corrosion protection due to the formation of a protection layer and the retardation of penetration of chlorides into the magnesium alloy surfaces. This work studied the corrosion protection of two magnesium alloys (Mg20Zn and Mg19Zn1Ca) in Hanks' solution with a controlled pH and temperature, close to the human body, covered by chitosan-based coatings enriched with inorganic compounds (chitosan_WG coating) and (chitosan/TiO2). The roughness and thickness of the coatings and their influence on the corrosion resistance of the alloys was examined. The microstructure of uncoated magnesium alloys was studied. Electrochemical tests were performed to understand the corrosion properties of bare alloys and covered samples.

Chapter I

Characteristic of magnesium and its alloys

1.1. Properties of Magnesium and its Alloys

Magnesium is the 9th most abundant element in the universe. Around 2% of the Earth's crust is made up of this metal. Magnesium is not found in elemental form in nature, but mainly in mineral forms, such as magnesite $MgCO_3$ (27% Mg), dolomite $MgCO_3$x $CaCO_3$ (13% Mg) and carnallite KCl x $MgCl_2$ x $6H_2O$ (8% Mg) [1]. Magnesium belongs to the group of alkaline earth metals. The metals in this group are all silver-colored and soft, with low densities, melting points, and boiling points, relative to others. An image of pure magnesium is shown in Fig. 1.1. Pure magnesium can be obtained during the electrolysis of a molten mixture of the following salts: anhydrous magnesium chloride, sodium chloride and calcium chloride at a temperature of approximately 1000°K. Magnesium can be obtained by direct reduction of MgO by carbon, reaction (1.1).

$$MgO + C = Mg + CO \tag{1.1}$$

In chemical terms, all alkaline metals react with the halogens to form the alkaline earth metal halides, all of which are ionic crystalline compounds.

Figure 1.1. Image of pure magnesium [2].

The chemical activity of magnesium is related with its electron configuration. As we can see in Fig.1.2, the valence electrons are located at the orbital 3s. To obtain a stable electron configuration like neon [Ne], magnesium gives two electrons to atoms of other chemical elements. Therefore, magnesium forms the ionic compounds during reactions with other chemical elements. The most popular chemical compounds of magnesium are: magnesium oxide MgO, magnesium hydroxide $Mg(OH)_2$, magnesium chloride $MgCl_2$, magnesium carbonate $MgCO_3$ and magnesium sulphate $MgSO_4$.

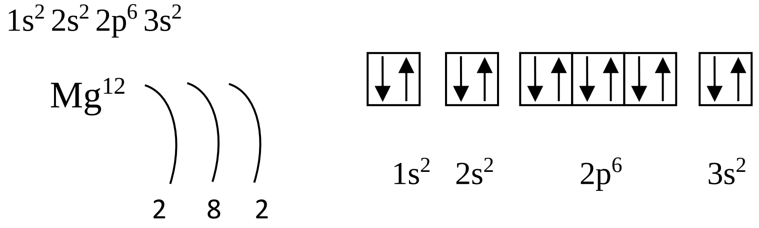

Figure 1.2. The electron configuration of magnesium

Magnesium oxide occurs in nature as a mineral called periclase. Magnesium oxide (MgO) is alkaline and forms magnesium hydroxide when reacting with water. This oxide is used in the production of refractory materials. Magnesium hydroxide $Mg(OH)_2$ has weak solubility in water, but the pH of this solution is alkaline. Magnesium chloride forms hydrates $MgCl_2{\cdot}nH_2O$, where n can be in the range from 1 to 12. This salt is highly soluble in water. Magnesium carbonate is an inorganic salt that can exist in the anhydrous form $MgCO_3$ and in the hydrated form $MgCO_3{\cdot}nH_2O$, where n can be equal to 1, 2, 3 or 5. Anhydrous magnesium carbonate is practically insoluble in water, acetone, and ammonia. Both anhydrous and hydrated forms of magnesium carbonate react with acids. Magnesium sulphate ($MgSO_4$) is an inorganic and anhydrous salt. However, because of the anhydrous form being unstable, this salt exists as a hydrated salt with the chemical formula $MgSO_4{\cdot}nH_2O$, where the "n" can have various values such as 1,2, 3...7, etc. Magnesium sulphate salt is water-soluble, but insoluble in organic solvents. Anhydrous magnesium sulphate is used as a desiccant.

Magnesium in contact with oxygen from the air quickly tarnishes because a layer of magnesium oxide forms on its surface, the reaction (1.2).

1) With oxygen:

$$2Mg + O_2 = 2MgO \qquad (1.2)$$

Mg reacts with water forming magnesium hydroxide $Mg(OH)_2$, reaction (1.3).

2) With water:

$$Mg + 2H_2O = Mg(OH)_2 + H_2\uparrow \qquad (1.3)$$

The standard electrochemical potential for magnesium is -2.34 V. Such a low value of standard electrochemical potential indicates that magnesium is a very active metal. When magnesium reactions with acids, hydrogen gas is released, reaction (1.4).

3) With acids:

$$Mg + 2HCl = MgCl_2 + H_2 \uparrow \tag{1.4}$$

Pure magnesium has the following properties: low density, high specific strength, elasticity modulus close to human bones, high amortization capability, high thermal conductivity, and biodegradability [3]. Magnesium alloys could, therefore, be determined as the lightest structural metallic materials, and that makes them interesting for applications in different sectors like aerospace, automotive [4], electronics [4] and biomedical [5]. One of the effective ways to improve the mechanical properties and corrosion resistance of magnesium alloys is the addition of rare earth elements [6]. In the literature it has been revealed that rare earth (RE) elements have significant effects on the high temperature strength and creep resistance of Mg alloys. Moreover, rare earth elements can considerably improve corrosion resistance of Mg-based alloys [7-9]. In addition, Mg-RE alloys are receiving increasing attention in biomedical applications. They exhibit good biodegradability and suitable mechanical properties and can be used for biodegradable implants [10]. Due to the toxicity of lanthanum and cerium compared to other rare earth elements, Mg-RE alloys should be used with great care [11]. The beneficial effect of RE elements on the corrosion behaviour of Mg alloys has been explain by the following factors:

1) RE elements reduce the effect of impurities in the melt metal by forming intermetallic compounds [12],

2) RE elements reduce the grain size and the amount of second phases caused by the formation of homogeneous microstructures, and decrease the probability of micro-galvanic corrosion [13],

3) RE elements can reduce the hydration of the corrosion products and improve their protective performance [14].

1.2. Design of Mg Alloys for Biomedical Application

Metallic materials play a critical role in developing degradable biomaterials compared to alternative materials such as ceramics, polymers, or bioactive glasses. The Young's modulus, or the tensile strength of biodegradable implants, should be close to human bones [15]. Mg and its alloys are very interesting for using in the biomedical sector because of its suitability to towards a temporary influence on bone-healing and their progressive dissolution in body liquid. Moreover, magnesium has nontoxic and non-allergic properties. The density and Young's modulus of Mg are very closer to human bone compared to other metallic materials used in biomedical applications. In addition, Mg ions seem to have positive effects on bone formation. Magnesium is a cofactor in more than 300 enzyme systems that regulate diverse biochemical reactions in the body, including protein synthesis, muscle and nerve function, blood glucose control, and blood pressure regulation [16]. Therefore, magnesium and its alloys are considered as a great candidate for use as a potential temporary implant material. Crystalline alloys containing biocompatible elements such as magnesium are now in high interest for orthopedic implants or substitutes for cranial bones, especially in pediatric surgery [17]. The advantage of a temporary Mg implant is the avoidance of a second surgery to later remove it, reducing the possibility of inflammation, stress-shielding and release of toxic metal ions which could occur with permanent metal implants [18,19]. The benefits are a reduction of medical costs and associated risks of a second surgical process and a decrease of patient trauma [20]. However, due to the low corrosion resistance, high chemical reactivity and fast hydrogen gas production [21,22,23] of Mg, its biomedical applications continue to be limited. To minimize these drawbacks, implants made of Mg and its alloys coated with a variety of biocompatible materials and numerous coating techniques have been put forward with varying degree of success and outcomes. It is therefore important to find a method of increasing the corrosion resistance of Mg alloys before promoting their widespread use in biomedical implants.

Corrosion behavior of Mg and its alloys could be improved in two ways:

- ✓ by using alloying elements to modify chemical composition and microstructure
- ✓ by using surface treatments or protective coatings (ceramic, polymer and composite materials) [24].

1.2.1. Selection of Alloying Elements for Biomedical Mg Alloys

One of the main advantages of magnesium alloys is the implant's ability to promote the healing effect and, as a result, the formation of new bone [25]. The addition of alloying elements determines the properties of the magnesium alloy. It is therefore extremely important to select non-toxic alloying elements to design magnesium-based implants that will be characterized by:

- ✓ high mechanical properties;
- ✓ excellent biocompatibility;
- ✓ excellent biodegradability;
- ✓ a high degree of body-friendliness (non-toxic and non-allergic);
- ✓ good corrosion resistance;
- ✓ and homogeneous degradation performance.

All of these factors make these materials suitable for orthopedic implants [26]. In recent years, much research has been conducted on binary systems such as Mg-Ca, Mg-Sr and Mg-Zn [27]. The addition of alloying elements to magnesium can improve its strength through a grain refinement mechanism. The addition of even small amounts (less than 5% wt.) of alloying elements such as yttrium, silver or strontium significantly accelerates the corrosion of magnesium alloys. In contrast, the addition of calcium or zinc up to 5% wt. slightly accelerates the corrosion of magnesium alloys. Gadolinium at less than 10% wt. slows the corrosion of magnesium, while at higher gadolinium contents the corrosion rate of magnesium increases dramatically. Only the addition of dysprosium (up to 20% wt.) does not significantly accelerate the corrosion of magnesium. Biodegradable implants made of magnesium alloys must contain non-toxic alloying elements. Alloying elements such as calcium, zinc, silicon, tin or strontium are considered non-toxic, with some of them even essential for human life e.g. calcium. Table 1 gives the solubility limit of the main alloying elements used to produce biodegradable magnesium alloys.

Table 1 shows the solubility limits of the main alloying elements in magnesium [28].

Table 1. Solubility limits of main alloying elements in magnesium (wt %) [28].

Element	Solubility
Ca	1.34
Si	~0
Zn	6.2
Sn	14.5
Zr	3.8

- **Calcium**

The reason why Ca is a good candidate to be used in Mg alloys as an alloying element is its biological effects. Magnesium and calcium are two of the most important metals for the human body and take part all main processes necessary for life. Human bones and teeth consist of almost 99% calcium and it is also a biocompatible, nontoxic and biodegradable element. Moreover, calcium is one of the most suitable alloying elements for biomedical applications, especially for orthopedic implants [24]. The release of calcium ions during the degradation of the implant improves bone healing [29]. Ca is an alkaline earth metal and has similar chemical properties to Mg, but it is more chemically active due to its electron configuration. Moreover, calcium has a low density of 1.55 g/cm^3, comparable to the density of Mg (1.74 g/cm3), which will maintain its specific properties [24]. The addition of a certain amount of calcium to a magnesium alloy can enhance its metallurgical quality, alleviating oxidation both in the melt and casting during heat treatment [27]. The addition of Ca can refine grains in the magnesium alloy and thus improve its strength and creep resistance.

- **Silicon**

In recent years, it has been proven that Si plays an important part in the human body. It was reported that Si plays an essential role in aiding the healing process [30] and bone formation because of its ions being involved in the calcification process of young bones. Si was also found to help build the immune system [30]. When silicon is added to the Mg-Ca alloy, two phases are formed: Mg_2Si and CaMgSi. The Mg_2Si phase looks like a needle and is distributed along the grain boundaries [32]. The addition of a small amount of Ca (less than 1wt.%) to an Mg-Si alloy causes the refinement of the Mg_2Si phase and the grain size.

- **Zinc**

Zn is one of the crucial elements for the human body. Zinc plays a relevant role in many biological functions such as normal growth, immune functions, protein and DNA synthesis, and wound healing [33]. It takes part in the metabolic process and is a component part of human tissues. Zn as an alloying element can improve the anti-corrosion and mechanical properties of Mg alloys, such as flexibility and toughness [34]. Zn exhibits antibacterial properties, which makes it extremely attractive as an alloying component for orthopedic implants. According to in vivo studies it was reported that zinc can promote osteoblast cell adhesion, distribution, differentiation (simulate bone formation) and inhibit bone resorption [35]. Zn is considered to have a moderate corrosion rate between Fe and Mg-based materials because of its standard electrode potential [27]. The standard electrochemical potential is -0,76 V for zinc and -2.36 V for magnesium, respectively. The addition of Zn to magnesium alloys increases their mechanical properties and modifies the corrosion resistance. The Mg−Zn alloy shows significantly lower hydrogen evolution volume compared to bare Mg [36]. Moreover, zinc decreases the impurities, such as nickel and iron present in magnesium alloys, and thanks to this enhance their corrosion resistance.

- **Tin**

It is not surprising that tin takes part in important living processes in the human body [30], and because of that tin is an extremely critical alloying element in Mg alloys used as a material to produce orthopedic implants. It was reported in some studies that the amount of Sn should range from 1 to 7 wt%. Tin improves the castability and corrosion resistance of Mg alloys [37]. Sn is a biocompatible element that is relatively non-toxic [38]. There are not many studies about Mg-Sn alloys, compared to other alloying elements for Mg alloys because Sn and its compounds provide low absorbance and accumulation in human tissues. Tin is rapidly excreted, mainly by kidneys [39]. Mg-Sn binary alloy fabrication is not that popular, but there are interesting results when such binary alloys are modified via deposition of hydroxyapatite (HA) coatings [40]. The main constitutional phases of Mg-Sn/HA composites were α-Mg and Mg_2Sn phases. Yield strength, ultimate compression strength and hardness were found to be increased with the addition of Sn in Mg/HA composites. Furthermore, the addition of Sn also played an important role in improving the corrosion resistance of the Mg-Sn/HA composite. The addition of Sn to magnesium alloy causes a refinement of grain size and the formation of

Mg_2Sn phases along the grain boundaries. Moreover, the addition of Sn improves both mechanical and corrosion properties of ternary and multi elemental alloys [41].

- **Zirconium**

Zircon is a safe and nontoxic element for human body. The addition of Zr helps in increasing the strength and decreasing the corrosion rate of the as-cast Mg–1Zr alloy. The results of hemocompatibility and cytotoxicity tests indicate that the Mg–1Zr alloy shows higher amounts of adhered platelets and shows no significant toxicity to osteoblasts. Moreover, the Mg–1Zr alloy has higher specific damping capacity than other metallic alloys and is therefore a promising candidate for a biomedical alloy [42, 43]. Zr-enriched magnesium alloys usually feature higher corrosion resistance than zirconium-free alloys.

1.3. Development of Binary and Ternary Mg Alloys Used as Degradable Metallic Biomaterials

1.3.1. Characteristics of Binary Mg-Ca and Mg-Zn Alloys

1.3.1.1. Mg-Ca alloys

The solubility of Ca in magnesium is relatively limited and is approximately 1.34 wt% under equilibrium conditions [27]. The main information about the microstructure of Mg-Ca alloys can be obtained from Mg-Ca phase diagram and from X-ray Diffraction measurements (XRD). The phase diagram of Mg-Ca alloys is presented in Fig. 1.3. It can seen that the main phases formed in the Mg-Ca alloy are an α-Mg matrix and Mg_2Ca in the ambient environment, and when the amount of Ca is less than 33,3 wt%, Figure 1.3. It is also evident that when Ca content is reduced to 10.6 wt%, an eutectic reaction takes place at the temperature of 517◦C (point e_7).

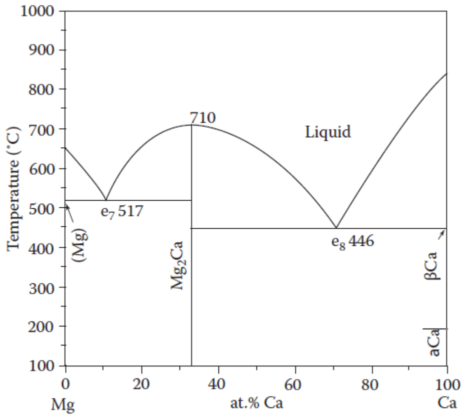

Fig. 1.3. Mg-Ca binary phase diagram [27]

The morphology of the second phase (Mg_2Ca) is depicted in Figure 1.4. It can be seen that the second phase Mg_2Ca is distributed mainly along the grain boundaries of the α-Mg matrix, but a few particles can also be located within the grain, Figure 1.4. (b). The eutectic, which means the mixture of two phases α-Mg and Mg_2Ca is presented in Figure 1.4. (c, d).

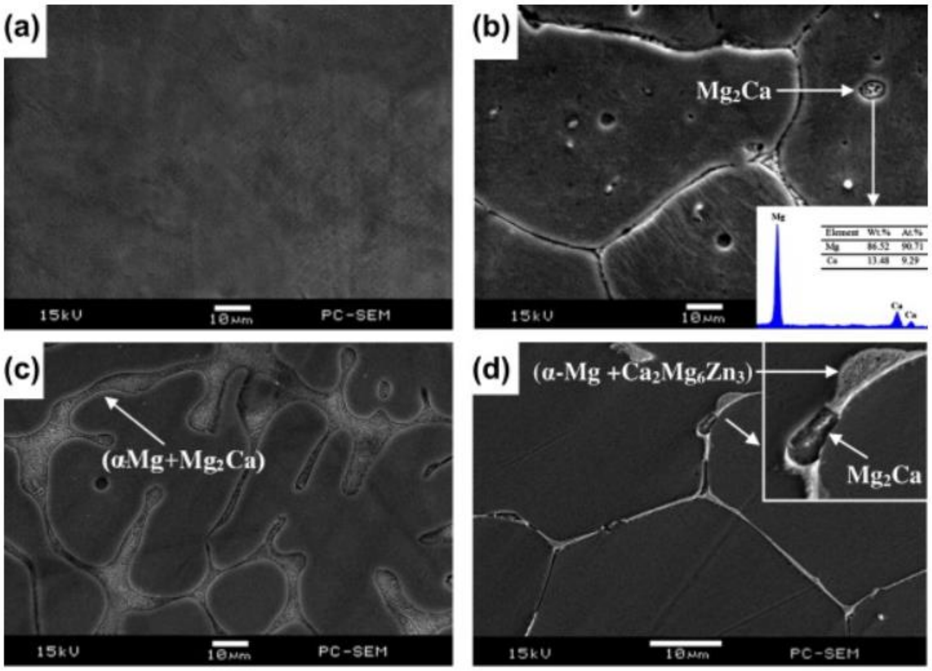

Fig. 1.4. SEM micrographs of (a) pure Mg (b) Mg–2Ca, (c) Mg–4Ca, (d) Mg–0.5Ca–0.5Mn–Zn [44]

It was found that the addition of calcium reduces the grain size of the Mg-Ca alloy [45] while an increase in calcium causes the formation of a continuous network structure of the Mg_2Ca phase [46]. The Mg_2Ca phase improves the mechanical properties, but also significantly increases the corrosion rate of Mg-Ca alloys. The fast corrosion of the Mg-Ca alloy is caused by the formation of galvanic coupling between the α-Mg matrix and the Mg_2Ca phase, which resulted in the release of hydrogen [27].

Binary Mg-Ca alloys, with low Ca content (0.6–3 wt.%), have demonstrated to be promising for orthopedic applications but they have a faster biodegradation rate than what is required for trauma implants [47]. The mechanical properties of Mg-Ca alloys depend on their calcium content [27]. Due to the grain refinement mechanism, the addition of Ca to Mg can both increase the strength and the elongation rate. Moreover, the addition of Ca to those types of alloys improved creep resistance at elevated temperatures and promotes hot tearing [48]. Calcium can refine the grain size and disperse the particles, breaking down the dendritic morphology of the particles into round and well-distributed small particles. Various publications have shown that the yield strength, ultimate tensile strength, and elongation of Mg-Ca alloys decreased with increasing Ca content, while the hardness of Mg-Ca alloys exhibited the reverse. In conclusion, it can be stated that the Mg-1Ca binary alloy shows very good mechanical properties and is a good material to produce biodegradable implants. Nevertheless, the sole use of Mg and Ca can cause brittleness, high sensitivity to oxidation and a rapid degradation of the magnesium alloy in the human body, leading to consequences such as osteolysis and stress-shielding problems [17]. Providing extra strength to biomedical implants that contain Mg alloys with Ca also requires the use of a restorative element such as Si.

1.3.1.2. Mg-Zn alloys

The binary phase diagram for Mg-Zn alloys is presented in Figure 1.5. As it shows, the maximum solid solubility of Zn in Mg is about 6.2 wt.%. Depending on the content of Zn, the Mg-Zn alloys can be divided into three different groups. The first one is one with a low amount of Zn, from 0.5 to 6% wt.%, which is below the solubility limit of Zn in Mg. The microstructure of low Zn content alloys mainly consists of a α-Mg solid solution, which improves the formability and machining property at elevated temperatures. Therefore, these alloys can be easily formed into their final shapes by hot working processing. The second group of Mg-Zn alloys has a chemical composition that is close to the deep eutectic point of the Mg-Zn system [49]. These alloys exhibit high glass-forming ability and can form an amorphous structure during rapid cooling. The third group is Zn-Mg alloys in which the Mg concentration is limited.

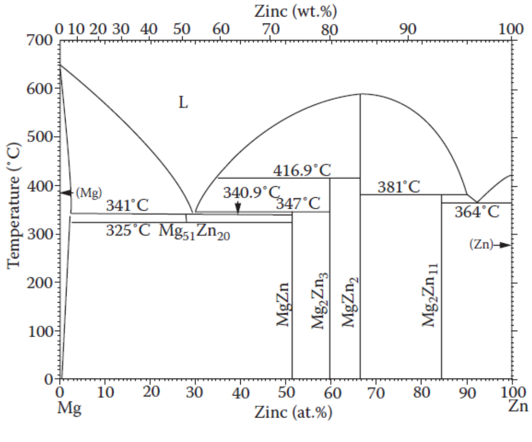

Fig. 1.5. Binary phase diagram of Mg-Zn alloys [27]

Ultimate strength in yield, tension, and compression of Mg-Zn binary alloys increases with increasing zinc content up to 5%. When the Zn content is less than 5%, the Zn mainly dissolves into an α-Mg matrix, which generates solid solution strengthening [27]. It means that the Mg-Zn phase runs from the α-Mg matrix along the grain boundaries and can promote the strength by dispersion strengthening. When the Zn content increases up to 7%, a network structure with dendritic segregation is formed along the grain boundaries. After this, residual defects and a sharp decrease in the strength and elongation of the Mg-Zn binary alloy take place [27]. However, the presence of an interdendritic Mg-Zn phase in alloys with a greater amount of Zn increases the corrosion rate. Corrosion behavior of the Mg-Zn alloys mainly depends on the Zn content and the distribution of the Mg-Zn phase [27]. Zinc has a high standard potential (-0.76V) compared to magnesium (-2.36V). Thus, the addition of zinc to magnesium alloys significantly reduces the release of hydrogen during their corrosion. The presence of zinc in magnesium alloys can improve their corrosion resistance. On the other hand, the corrosion rate in MgZn alloys can be high due to the formation of galvanic couples (micro galvanic corrosion) between the α-matrix and the MgZn-type intermetallic phases. The corrosion rate depends on the zinc content in the MgZn alloy, the chemical composition of the intermetallic phases and their distribution. Figure 1.6. demonstrates a microstructure of MgZn alloys with different contents of alloying elements in magnesium alloys.

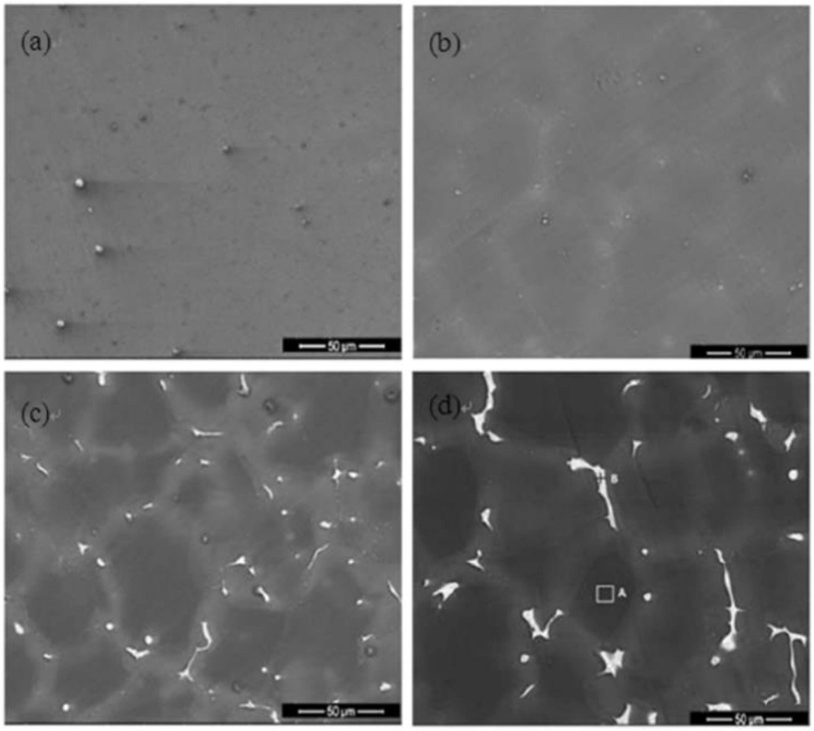

Fig. 1.6. BSE-mode SEM micrograph of surface morphologies of pure Mg (a), Mg-1Zn (b), Mg-5Zn (c) and Mg-7Zn (d) [50]

1.3.2. Characteristic of Ternary Mg Alloys

1.3.2.1. Mg-Ca-Zn ternary alloys

Calcium is one of the surface-active elements influencing surface composition of Mg binary and ternary alloys. This element ehances the oxidation and corrosion rate of magnesium alloys [51].

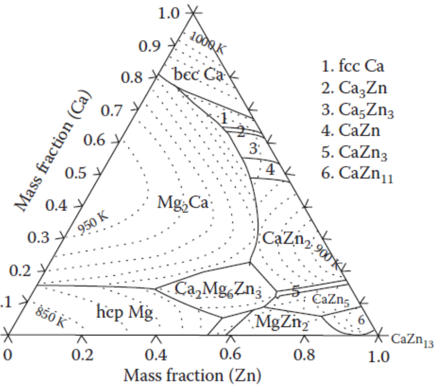

Fig. 1.7. Ternary phase diagram of the as-cast Mg-Ca-Zn alloys [27].

The ternary phase diagram of as cast alloy Mg-Ca-Zn is presented in Figure 1.7. The presence of Zn has significant influence on the microstructure of the Mg-Ca alloy. From the phase diagram, it can be seen that when the ternary Mg-Ca-Zn alloy melts cool down, the following eutectic reaction occurs (1.5.):

$$L \rightarrow \alpha - Mg + Mg_2Ca + Ca_2Mg_6Zn_3 \qquad (1.5.)$$

It has been reported that the eutectic composition depends on the Zn/Ca atomic ratio [52]. When the Zn/Ca atomic ratio is more than 1.2 (α-Mg + $Ca_2Mg_6Zn_3$) phase is formed, and when the Zn/Ca ratio is less than 1.2 the eutectic (α-Mg +Mg_2Ca + $Ca_2Mg_6Zn_3$) phase precipitates. The addition of Zn in the Mg-Ca-Zn alloys can lead to grain refinement [53]. If the ternary Mg-Ca-Zn alloy contains less than 4% of Zn, the secondary phases are mainly distributed along the grain boundary. When the content of Zn is higher than 4%, small-sized second phase particles can be found in grain interiors.

The addition of calcium to MgZn alloys results in the refinement of grains. It has been reported that hydrogen evolution in physiological solutions can be decreased during the degradation process or even absolutely prevented using MgZnCa alloys [54]. Figure 1.8 shows an SEM image of Mg-1.2Zn-0.5Ca as a cast alloy [55] where a dendritic microstructure of the alloy and a determined α-Mg – matrix and intermetallic phase – $Ca_2Mg_6Zn_3$ are clear.

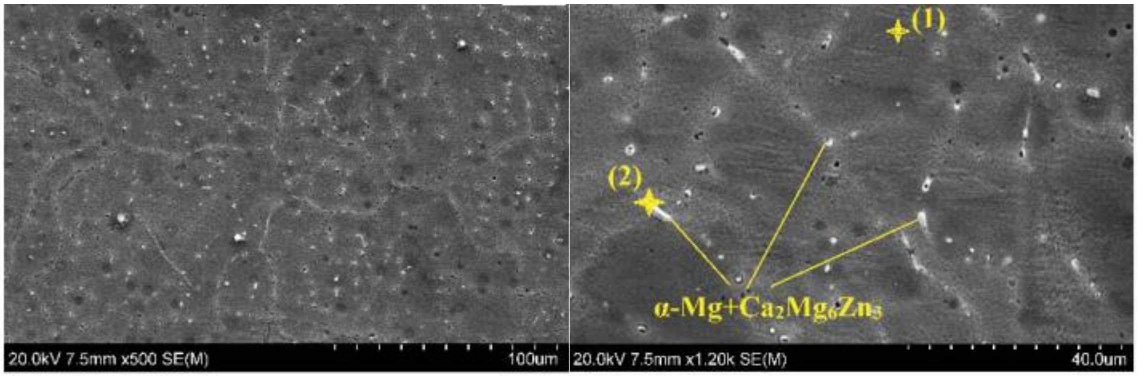

Figure 1.8. SEM image MgZnCa as cast alloy [56].

The Mg-Zn-Ca alloy is improving important mechanical properties of alloying elements, namely strength and ductility [55]. As with most Mg alloys and pure magnesium, the MgZnCa alloy has rapid reduction in strength through degradation. From one side it might be a problem, but not in case of degradable implant materials due to the main task of these materials – to provide temporary support for broken bones, but not to be a total substitute [57]. Glassy MgZnCa alloy has a range of advantages compared to crystalline structure of Mg alloys – lower ductility, higher strength and a higher elastic limit as well as a Young’s modulus value that is lower and closer to the human body. These characteristics makes MgZnCa alloy very attractive for new biomedical implant materials applications [57].

1.3.2.2. Mg-Ca-Si ternary alloys

Mg-Ca-Si ternary alloys are an attractive material for biomedical applications as orthopedic implants because of the presence of both alloying elements (Ca and Si) in the human body as well as taking place in natural processes connected with bone regeneration [58]. Mg-0.2Ca-0.6Si alloys mainly consist of needle like Mg_2Si and CaMgSi phases. The needle Mg_2Si phase tended to distribute along the grain boundary. The addition of Ca influences the refinement of the Mg_2Si and grain size [27]. Moreover, the presence of Mg_2Si phase influences the enhancing mechanical properties of the ternary alloy [59].

Apart from their function in the body, Ca and Si can improve the mechanical properties of Mg-based alloys and facilitate their production process. The low solubility of Ca in Mg results in the formation of the intermetallic phase Mg_2Ca. When located at grain boundaries, this compound can result in grain refinement of the Mg matrix. Si has a lower solubility in Mg (0.006 wt%). A very small addition of Si into Mg results in a pronounced increase in ductility, while the tensile strength remains almost unaffected. For larger amounts of Si, the hardness and the tensile strength are improved by the presence of small Mg_2Si precipitates (<2 μm). Si is known to increase the fluidity of the melt, which is important for casting [15].The final microstructure and mechanical properties of cast alloys strongly depend on the solidification process.

The Mg_2Si phase formed during the solidification via eutectic reaction has a coarse lamellar structure. It breaks the α-Mg matrix under tensile or compressive conditions. Mg_2Si phase must be modified because of improvement of mechanical properties. It was reported that the addition of Ca to Mg-Si alloys refines grain size, modifies the Mg_2Si phase to a short bare shape. Presence of Ca in those types of alloys reduces the fraction of Mg_2Si to form the CaMgSi phase. Both of these phases are brittle, which is why the amount of Ca inside the alloy has to be a very low at about 0,2 wt%, because when it is between 0.2-0.4 there’s no improvement in elongation and tensile strength [27].

Chapter II

Corrosion Degradation of Mg Alloys

2.1. Thermodynamic aspects of corrosion of magnesium and its alloys

Corrosion is the spontaneous degradation of a material due to its interaction with an environment [60]. Corrosion occurs in metals, alloys, semiconductors, polymers, and even ceramic materials [61].

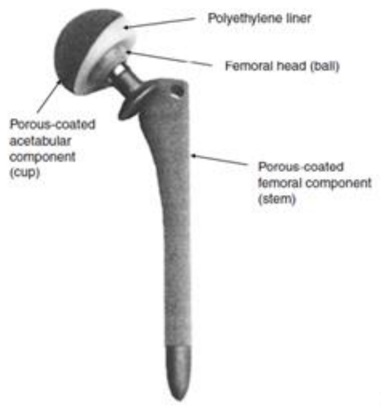

Fig. 2.1. An artificial hip used in hip-replacement surgery [64]

When metallic or constructional materials are damaged in contact with seawater or body human fluids, this damaging process is known as biocorrosion [62]. Biocorrosion is generally caused by the presence of microbes and the interaction of metals with the aggressive ions present in the environment. Fig. 2.1 shows a typical hip implant that could undergo corrosion during its lifetime after microbial or bacteria influence, and that could provide implant rejection as a result. Nowadays it is highly used titanium, titanium alloys, and chromium-based alloys as bone implants. In the past two decades, there has been significant emphasis on studying the corrosion degradation of magnesium alloys, which can be used in potential biodegradable implants. The main obstacle for the application of magnesium alloys in medical and other sectors is their fast corrosion rate. Many factors have an influence on the corrosion rate of metallic implants.

Critical factors for corrosion process are shown in Figure 2.2. The corrosion of alloys depends on many factors such as:

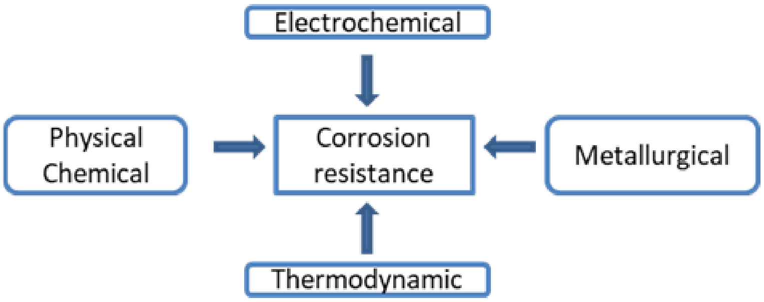

Fig. 2.2. Factors affecting corrosion resistance of a metal [63]

- the microstructure of the alloy, which depends on the chemical composition of an alloy and its manufacturing method (casting method, heat treatment, mechanical treatment, etc.)
- the chemical composition of the corrosive environment
- physical parameters, e.g. temperature, flow rate of liquids
- the presence of bacteria in the corrosive environment

- mechanical factors, such as the presence of mechanical stresses (tensile, compressive stress).

Thermodynamically, magnesium is a very active metal. Its electrochemical potential is -2.37 V at 25°C. For corrosion of magnesium and other metals, the following thermodynamic aspects should be considered [64]:

- When a solution pH increases, the nature of corrosion products changes,
- For most of the metals in neutral or close to neutral solutions, corrosion products are no longer in ionic form – solid reaction (oxides-hydroxides) products start to form. This formation and the nature of the corrosion products can control the corrosion process
- The stability region of these products and ionic species is dependent on potential and pH.

Pourbaix diagrams map the conditions of potential and pH where different ionic and solid species are stable. . In Fig.2.3 Pourbaix diagram is shown for Mg in water at constant temperature (25°C).Magnesium is a very active metal and can corrode in pure water. During this reaction the magnesium hydroxide and hydrogen gas are formed, reaction 2.1.

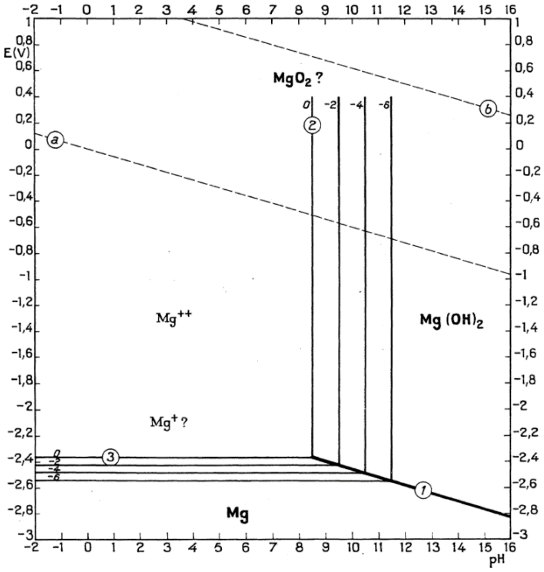

Fig. 2.3 Potential equilibrium diagram for the system Mg-water at 25^0 C [65]

$$Mg + 2H_2O \rightarrow Mg(OH)_2 + H_2 \qquad (2.1)$$

Magnesium is a very base metal and powerful reducing agent [65]. It has a high affinity for oxygen and reacts with it to form magnesium oxide, reaction 2.2 [66].

$$Mg + 1/2\, O_2 \rightarrow MgO \qquad (2.2)$$

The standard Gibbs free energy changes (ΔG^0) are -369 kJ/mol and -569 kJ/mol for reactions 2.1 and 2.2, respectively. Such low values of ΔG^0 confirm that magnesium in the natural environment has a high tendency to occur in the oxidized state. Magnesium is more stable in in an oxidized state than in its metallic state.

The stability of magnesium species can be predicted from E-pH diagram (Pourbaix diagram). As shown in Fig. 2.3, the area of thermodynamic stability of magnesium is very narrow (the area marked Mg). Magnesium is stable over a wide pH range, but only at low potentials. In strongly alkaline media, a magnesium hydroxide layer is formed on the magnesium surface (the area labeled $Mg(OH)_2$). In the Pourbaix diagram, Fig. 2.3, the area of thermodynamic stability of water is also marked and is located between the lines “a” and “b”. The line “a” represents the reversible potential for the hydrogen electrode, equations (2.3) and (2.4).

$$2H^+ + 2e \rightarrow H_2 \tag{2.3}$$

$$E_{rev} = -0.059\,pH \tag{2.4}$$

The line “b” represents the reversible potential of the oxygen electrode, equations (2.5) and (2.6).

$$O_2 + 4H^+ + 4e \rightarrow 2H_2O \tag{2.5}$$

$$E_{rev} = 1.23 - 0.059pH \tag{2.6}$$

The area of thermodynamic stability of water located between “a” and “b” lines gives the range of potentials and pH in which water molecules are stable at 25°C and 1 atm pressure.

Pourbaix diagrams have been determined for almost all metals, making it possible to determine in which pH and potential range a metal corrodes. It should be noted that E-pH diagrams were created based on thermodynamic calculations and allow to determine under what conditions the system will reach equilibrium, but they do not allow for the determination of how quickly this equilibrium state will be reached. Therefore, Pourbaix diagrams do not give information about the kinetics of metal corrosion processes.

2.2. Composition and protectiveness of surface film

Due to contact with air or water, the surface of magnesium is covered with a layer of magnesium oxide or hydroxide. The corrosion resistance of Mg and its alloys is extremely dependent on the formation of a protective film on the surface of the metal/alloy. Critical factors for surface film formation depend on the nature of the solution, formation conditions, purity of metal, or chemical composition of the magnesium alloy. Mg alloys corrode faster than high-purity (HP) Mg. The impurity elements which can be found in magnesium are (Fe, Ni, Cu, and Co). In the case of (HP) magnesium, the impurity elements are below their (alloy-dependent) tolerance limit [67-70]. If the content of impurity elements is above the tolerance limit, the corrosion rate of magnesium is high. The chemical composition and pH of the corrosive environment also have a significant impact on the structure of the surface layer. In an aqueous environment with a pH of about 7 according to the E-pH diagram, a surface layer should not form. Under such conditions, however, magnesium dissolution occurs leading to alkalization of the metal surface, hydrogen evolution, and formation of a surface layer containing magnesium hydroxide [65]. From the thermodynamic point of view, the most stable species of magnesium are MgO and $Mg(OH)_2$. In dry atmospheric conditions, magnesium oxide is the main component of the surface film formed by magnesium and its alloy. If water vapor is present in the air, magnesium hydroxide is formed on the surface of magnesium or its alloy. The schematic diagram of magnesium surface film microstructure is presented in Fig. 2.4.

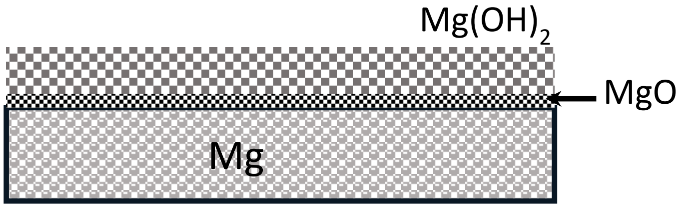

Fig. 2.4. Diagram of Mg surface microstructure.

The surface layer of magnesium and its alloys consists of two layers: an inner compact layer containing magnesium oxide and an outer porous layer composed of magnesium hydroxide. This is a very simple model of surface layer structure for Mg. The structure of the surface layer is, in fact, more complex, especially for magnesium alloys. Carbon dioxide in the air can combine with moisture to form a weak carbonic acid that further reacts with magnesium hydroxide and magnesium carbonate ($MgCO_3$) or hydrated magnesium carbonate $MgCO_3 \cdot xH_2O$ ($x = 3, 5$) is formed [71-73]. Industrial air pollutants such as SO_2 and SO_3 can react with magnesium hydroxide, which can then cause hydrated magnesium sulfate $MgSO_4 \cdot 6H_2O$ to form on the metal surface. For magnesium alloys containing various alloying elements, the surface layer also contains oxides of these elements in small amounts. Magnesium alloys usually contain Al, Zn, Mn, and Zr as alloying elements. Magnesium has a much higher affinity for oxygen than other alloying elements found in magnesium alloys. As a result, magnesium oxide and hydroxide are mainly formed on their surface. The surface layer produced on magnesium in aqueous solutions is not as stable as, for example, the surface layer on pure aluminum. The structure of the surface layer formed on both metals (Mg, Al) is similar. Aluminum hydroxide is stable in weakly acidic, neutral, and weakly alkaline environments due to its amphoteric properties. Magnesium hydroxide, however, is not stable in acidic, neutral, or weakly alkaline solutions according to the E-pH diagram. Consequently, the surface layer formed on magnesium is not compact and offers only limited protection against corrosion.

2.3. Anodic and cathodic processes

2.3.1. Anodic dissolution and negative different effect (NDE)

The anodic dissolution process of Mg exhibits different behaviors compared to other metals due to the unique electrochemistry of magnesium. For most metals, increases in anodic potential cause an increased anodic dissolution rate and simultaneously a decreased cathodic hydrogen evolution rate. For Mg and its alloys, however, the hydrogen evolution rate increases when the polarization potential becomes more positive in the anodic region. Such behavior is associated with the negative difference effect (NDE). According to the definition, the difference effect is the difference, between the hydrogen evolution rate at the open-circuit potential, I_{OCP}, and the hydrogen evolution rate, I_A, at a given anodic polarization potential, equation (2.7).

$$\Delta = I_{OCP} - I_A \tag{2.7}$$

When Δ is negative this phenomenon is termed the negative difference effect (NDE).

The hydrogen evolution process is always involved in the anodic dissolution of Mg and its alloys [74].

In the case of corrosion of magnesium and its alloys, two types of hydrogen evolution are distinguished: anodic hydrogen evolution (AHE), and cathodic hydrogen evolution (CHE) which is associated with the cathodic reduction reaction [75]. In general, the hydrogen evolution from a corroding surface of Mg and its alloys consists of both ‘anodic’ and ‘cathodic’ processes [74]. The cathodic hydrogen evolution (CHE) emanates mainly from the non-corroded area of a magnesium alloy (usually an intermetallic phase) and is represented by the cathodic branch of the polarization curve for the alloy. The anodic dissolution of a Mg alloy, meanwhile, is associated with the anodic hydrogen evolution (AHE) from the corroding areas of the alloy (usually a matrix). The anodic dissolution and AHE are represented by the anodic branch of the polarization curve for the alloy.

The anodic dissolution of Mg in an aqueous solution can be described by reaction (2.8).

$$Mg \rightarrow Mg^{2+} + 2e \tag{2.8}$$

This reaction proceeds through an intermediate step involving a mono-valence Mg^+, reaction (2.9).

$$Mg \rightarrow Mg^{+} + e \tag{2.9}$$

Mg^+ ion is not stable and can rapidly change into the more stable ion Mg^{2+}, reaction (2.10).

$$Mg^{+} \rightarrow\ Mg^{2+} + e \tag{2.10}$$

The overall dissolution of Mg in the aqueous solution proceeds according to the reaction (2.8).

Because of the high instability in aqueous solution, Mg^{+} may change into other intermediate species through disproportionation and hydration reactions [74]. The disproportionation reaction of Mg^{+} leads to the formation of the $Mg{\cdot}Mg^{2+}$, reaction (2.11).

$$Mg^{+} \rightarrow Mg + Mg^{2+} \rightarrow Mg \cdot Mg^{2+} \tag{2.11}$$

The $Mg{\cdot}Mg^{2+}$ product is deposited on the surface of Mg and then can react with water forming the final products, reactions (2.12) and (2.13).

In acidic solution:

$$Mg \cdot Mg^{2+} + 2H^{+} \rightarrow 2Mg^{2+} +\ H_2 \tag{2.12}$$

In neutral or basic solution:

$$Mg \cdot Mg^{2+} + 2H_2O \rightarrow Mg(OH)_2 +\ Mg^{2+} +\ H_2 \tag{2.13}$$

Direct hydration of Mg^{+} ions generates the evolution of hydrogen, reactions (2.14) and (2.15).

In acidic solution:

$$2Mg^{+} + 2H^{+} \rightarrow 2Mg^{2+} +\ H_2 \tag{2.14}$$

In neutral or basic solution:

$$2Mg^{+} + 2H_2O \rightarrow\ OH^{-} + 2Mg^{2+} +\ H_2 \tag{2.15}$$

2.3.2. Cathodic reduction reactions

For many metals and alloys, oxygen reduction and hydrogen evolution are two typical cathodic reduction reactions in an aqueous solution. In neutral or alkaline solutions, the oxygen reduction reaction is usually more dominant than the hydrogen evolution reaction, but this is not the case for magnesium and its alloys. In these solutions, an oxygen reduction reaction can occur, but the concentration of dissolved oxygen is very low. Therefore, the reduction of oxygen can be ignored, and the hydrogen evolution reaction is considered a significant cathodic reduction reaction in an aqueous environment. The cathodic hydrogen evolution on Mg proceeds according to the reactions (2.16) and (2.17) for the acidic and neutral or alkaline solutions, respectively.

$$2H^{+} + 2e \rightarrow H_2 \qquad \text{(in acidic solution)} \qquad (2.16)$$

$$2H_2O + 2e \rightarrow H_2 + 2OH^{-} \qquad \text{(in neutral or basic solutions)} \qquad (2.17)$$

The mechanism of hydrogen evolution is complex and some intermediates species such as Mg^{+} and MgH_2 can catalyze this process. Intermediate magnesium ion Mg^{+} can participate in the cathodic process. If the Mg^{2+} ions are present in the solution, first they are reduced into intermediate Mg^{+} on the surface of the magnesium, reaction (2.18).

$$Mg^{2+} + e \rightarrow Mg^{+} \qquad (2.18)$$

Then Mg^{+} reacts with water and hydrogen is generated, a reaction (2.19).

$$2Mg^{+}\ 2H_2O \rightarrow 2Mg^{2+} + 2OH^{-} + H_2 \qquad (2.19)$$

The equilibrium potential of the reaction (2.18) is –2.067 V is more negative than the normal standard hydrogen evolution potential and the corrosion potentials of Mg. Therefore, the Mg^{+} intermediate mechanism is likely only when the Mg or magnesium alloy electrode is strongly cathodically polarized and the Mg^{2+} ions are present in the solution. During the cathodic process, the magnesium ions Mg^{2+} and $Mg(OH)_2$ can be reduced according to reactions (2.20) and (2.21).

$$Mg^{2+} + 2H^{+} + 4e \rightarrow MgH_2 \qquad (2.20)$$

$$Mg(OH)_2 + 2H^{+} + 4e \rightarrow MgH_2 + 2OH^{-} \qquad (2.21)$$

Then, the MgH_2 can be oxidized, and hydrogen gas and Mg^{2+} are generated, a reaction (2.22).

$$MgH_2 + 2H_2O \rightarrow Mg^{2+} + 2OH^{-} + 2H_2 \leftrightarrow Mg(OH)_2 + 2H_2 \qquad (2.22)$$

The MgH_2 is unstable and in contact with water undergoes decomposition and H_2, Mg^{2+}, or $Mg(OH)_2$ are formed according to equation (2.22).

The standard electrochemical potentials for the reactions (2.20) and (2.21) are $E^0 = -1.114V$ and $E^0 = -1.256V$, respectively. These values are much more positive than the electrochemical potential for the reaction (2.18). Hence, when the cathodic polarization potential is not very negative, the cathodic hydrogen process may follow the MgH_2-catalyzed hydrogen evolution mechanism. Four electrons are involved in reactions (2.20) and (2.21), therefore, the probability of these reactions occurring is very low in practice.

2.4. Influence of Alloying Elements on Corrosion Resistance of Mg Alloys

According to the Pourbaix diagram, it has been shown that Mg corrodes in a wide range of pH, and hydrogen evolution is observed [76]. There are a few ways to improve the corrosion resistance of Mg:

- The addition of different alloying elements (metals, non-metals) in different amounts or percentages
- The application of protective coatings (organic, inorganic),
- The applications of heat treatments.

Alloying elements present in Mg alloys improve their mechanical properties, casting, and corrosion protection. Depending on the applications, Mg is generally alloyed with aluminum, zinc, lithium, rhenium, thorium and silver with minor additions of manganese, zirconium, and cerium [76]. Aluminum and zinc improve mechanical properties and enhance the corrosion resistance of magnesium alloys. Aluminum is incorporated in the surface layer formed on magnesium alloy. It has been stated that an increase in the Al content of the Mg alloy above 4% causes an increase in Al content of the inner surface layer. The thickness of the inner layer is reduced by almost one order of magnitude. It has been proven that the reduced thickness leads to reduced hydration evolution and better corrosion resistance [77]. The addition of zinc into magnesium alloys may increase the potential of hydrogen evolution on their surface. This means that the addition of Zn will not lead to an increased corrosion rate of the α phase (matrix) of magnesium alloys [78]. Contrary to that, Fe, Co, Ni and Cu will reduce the corrosion resistance of Mg alloys and decrease the mechanical properties of the material [27].

In recent years, a lot of research has been devoted to the effect of rare earth elements on the corrosion resistance of magnesium alloys. The incorporation of erbium in the $Mg(OH)_2$ lattice caused a significant improvement in the corrosion resistance of MgAlEr alloys [79]. Zhou et al. have revealed that the formation of intermetallic phases containing holmium, which is less cathodic than other intermetallic phases, slows down the corrosion rate of MgAlHo alloy. On the surface of MgAlHo alloy, the corrosion products were deposited, and they restrain further corrosion [80]. The addition of Ca, La, and Ce to AZ91 alloy caused the formation of the reticular Al_2Ca phase, which acted as a barrier against corrosion [81]. Cerium added in the as-cast AZ91 alloy caused significant changes in its microstructure. The refinement of the beta phase and formation of Al_4Ce intermetallic phase led to decreases in corrosion current density in AZ91 alloy [82,83]. The potentiodynamic polarization curves plotted in 0.01M NaOH solution for wrought AZ91 alloy containing Ce have shown, that the anodic current density is twice higher than for AZ91 alloy without Ce. This result indicates that the stability of the passive film is worst with the addition of Ce in AZ91 alloy. The passive film consists of two layers inner and outer. The inner passive film consists of oxides (mainly MgO and CeO_2), whereas the outer part of the passive film consists of metal hydroxides. The electrochemical impedance measurements have shown that the existence of CeO_2 in the inner layer had two effects on the passive, behavior of wrought AZ91 alloy. First, CeO_2 acted as a barrier film and made mass transport through the passive film follow tangent hyperbolic impedance for AZ91 alloy with Ce, while for AZ91 alloy without Ce the mass transport proceeded with Warburg impedance. Second, the transformation from $Ce(OH)_3$ to CeO_2 led to the increase of defect density (Nd) in the passive film, which was the main reason for the passive current density increase for wrought AZ91 alloy containing Ce [74]. The influence of La, Nd, Ce, Gd, and Dy on the corrosion resistance of magnesium alloys has been investigated in the 3.5 wt% NaCl solution. It has been shown that the corrosion resistance of the Mg-RE alloys is increasing in the following order: Mg-1.43La, Mg-1.44Nd, Mg-0.3Ce, Mg-0.63Gd, and Mg-0.41Dy. The highest resistance against corrosion has been determined for magnesium alloy containing dysprosium. The formation of the Dy_2O_3 oxide prevents the Mg-0.41Dy alloy from pitting corrosion. A complete protective layer covers the Mg-0.41Dy alloy surface which indicates a uniform corrosion mechanism. While the Mg-1.43La alloy exhibits a micro-galvanic corrosion mechanism caused by the pitting corrosion. The presence of $Mg_{12}La$ intermetallic phase along the grain's boundaries in the Mg-1.43La alloy causes severe pitting corrosion by acting as an anodic phase [84].It has been shown that some rare earth elements improve the corrosion resistance of magnesium alloys. Some researchers proposed the production of single-phase magnesium alloys containing REEs like Ho, Er or Lu. Magnesium alloys with single-phased microstructures exhibit good corrosion resistance and comparable mechanical properties to the clinically proven Mg based implants [85].

2.5. Types of Corrosion

Corrosion of metallic materials has many forms. By looking at the extent of corrosion on the surface of the material (metal, alloy), we can distinguish uniform and localized corrosion. Regarding the mechanism of corrosion, we distinguish between chemical and electrochemical corrosion. Corrosion can take place in acidic solutions, alkaline solutions, seawater, organic environments, molten salts, etc. In the case of uniform corrosion, anodic and cathodic reactions occur over the entire surface of the sample, but not in the same place at the same time. The electrolyte concentration is generally constant or very close to constant, and the metal is homogeneous [86]. Corrosion caused by the simultaneous action of mechanical stress and corrosive environment is called stress corrosion cracking. Material damage can also occur due to mutual friction of the surfaces of two materials in a corrosive environment. This type of corrosion is called tribocorrosion.

According to previous comments and based on literature [60-66, 86], the following types of corrosion can be identified:

- Uniform or general corrosion;
- Galvanic corrosion;
- Pitting;
- Crevice corrosion;
- Filiform corrosion;
- Stress corrosion cracking;
- Intergranular corrosion;
- Selective leaching;
- Erosion corrosion;
- Hydrogen damage [87].

In 1982, Dilon [88] classified corrosion into two groups respective to different ways of examination.

Group I: Corrosion detected by visual examination – uniform corrosion, galvanic corrosion and localized corrosion (pitting, crevice, and filiform corrosion).

Group II: Corrosion studies that depend on additive indentations and examinations: erosion corrosion, intergranular corrosion, selective leaching (composition changes of the alloys due to selective dissolution), environmental cracking and microbial corrosion [87].

2.5.1. Galvanic Corrosion

Galvanic corrosion occurs when two or more metallic materials are electrically connected and placed into an electrolyte solution [89]. In such a case, a corrosion cell is formed in which the metal or alloy having a higher electrochemical potential works as the cathode while the other with a lower potential as the anode. In Fig. 2.4. are shown galvanic couple and corrosion between them on the seam of two different metallic materials. In this corrosion type, the critical factor is to obtain the difference of potentials between the metals [90]. The driving force of galvanic corrosion is the potential difference between the cathode and the anode.

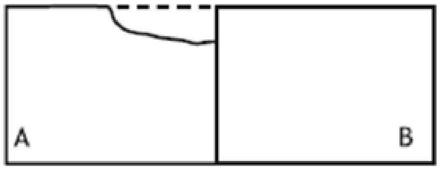

Figure 2.4. Galvanic corrosion on a seam of two metals.

At the anode, anodic oxidation of the metal occurs, while at the cathode, cathodic reduction reactions (reduction of oxygen, hydrogen ions or water molecules) take place. The corrosion mechanism in galvanic corrosion depends on the metal's nature. Less corrosion resistant metal becomes anode while more corrosion resistant metal becomes the cathode [90]. Compared to other corrosion types, galvanic corrosion is more visible on the seam between metals or, in the case of alloys, at the interface between the intermetallic phase and the matrix. Critical factors that affect the rate of galvanic corrosion are:

- distance between the anode and the cathode - when rising the galvanic corrosion slows down;
- conductivity of the solution – the more conductive the solution, the higher the corrosion rate;

- cathode-anode ratio – in the case when the cathode surface is large and the anode surface is small, galvanic corrosion is very fast.

In this work, the corrosion resistance of magnesium alloys in the Hank’s solution has been investigated. The electrochemical potential of Mg is very low compared to the potential measured for many metals. In this regard, pure magnesium in contact with other metals works as a local anode [91]. The galvanic is very common in magnesium alloys. The formation of galvanic pairs between the matrix (α-Mg) and other intermetallic phases can also be observed during the corrosion of one of the most popular cast magnesium alloys, AZ91. Measurements of local corrosion potential have shown very large potential differences between the matrix and sites containing the matrix and the β-Mg17(Al, Zn)12 or AlMn intermetallic phases. Corrosion potential differences between the matrix and other intermetallic phases were in the range of tens even up to 300 mV [92].

To prevent galvanic corrosion, the connected materials must be properly selected to avoid the formation of galvanic cells. If materials that can form a strong corrosion cell must be combined, then proper insulation must be selected to prevent current flow between the cathode and anode. In addition, the ratio of anode to cathode area in galvanic corrosion is also very important. A large surface area is critical for the design of an anode surface.

2.5.2. Localized Corrosion

Localized corrosion has clearly expressed cathodic and anodic places on the alloy's surface [93]. The main difference between the uniform (a) and localized corrosion (b) is shown in Fig. 2.5.A localized corrosion phenomenon is much more difficult to have under control, compared to the uniform variety. Localized corrosion occurs in specific places on the metallic surface because of material damage or a combination of different types of materials. Furthermore, the corrosion environment can promote holes, pits or crevices.

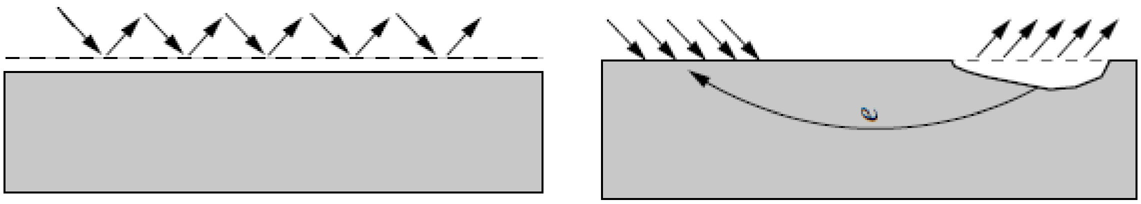

Figure 2.5 a) uniform corrosion b) localized corrosion on the metal surface [93]

In the case of localized corrosion, both anodic and cathodic zones can be detected [93]. It is necessary to mention that the local corrosion phenomenon is more common in nature and industry due to the presence of many factors that promote local damages of metals and alloys. Even the presence of microorganisms such as bacteria, fungi, and microalgae could provide localized corrosion – pitting, dealloying, erosion and galvanic corrosion [76]. The main problem of local corrosion caused by microorganisms is the difficulty in detecting where the corrosion begins as well as a high corrosion rate [76]. The most common forms for localized attack are pitting, crevice corrosion, stress-corrosion cracking and filiform corrosion [64].

2.5.3. Pitting Corrosion

Pitting corrosion is one of the most destructive types of local corrosion that typically occurs on passivated metals and alloys [94]. Pits visible on the surface of an alloy are very small but deep, and usually, cause a drastic reduction in the mechanical properties of the material. The diameter of the pits is much smaller than their depth [87]. Pitting corrosion is very difficult to observe because pits are often covered with corrosion products. The pit itself is a local anode where the metal dissolution takes place, while cathodic reactions take place on the surface of the alloy or at the metal around the pit. The mass loss of the metal or alloy due to pitting corrosion is so small that the occurrence of pitting corrosion and its rate cannot be determined from gravimetric tests. The susceptibility of a material to pitting corrosion depends on many factors such as the presence of aggressive ions in the corrosive environment, pH, temperature, oxygen concentration, the presence of oxidants and the microstructure of the alloy [87, 95-100]. Alloys immersed in corrosive environments containing halogen ions (F^-, Cl^-, Br^-, I^-) are most susceptible to pitting corrosion [101], [102], and the presence of S^{2-} and SO_4^{2-} ions can also cause pitting corrosion. In Fig. 2.6. different forms of pits are illustrated. During pitting corrosion, pits of various shapes are formed. The morphology of the pits depends on the potential value, the concentration of aggressive ions, the pH of the electrolyte solution, the microstructure of the alloy, the structure of the passive layer and the chemical composition of the corrosion environment [87].

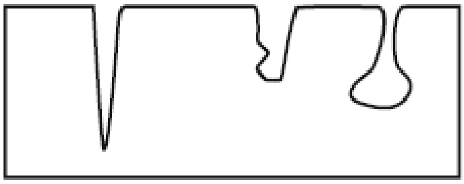

Figure 2.6. Morphology of pits

Pits can be wide and shallow, narrow but very deep, elliptical, undercut, or subsurface, and it is possible to find pits that are formed by horizontal or vertical attacks of grain boundaries [103].

Pitting corrosion occurs in an environment containing aggressive ions and proceeds in several stages.

1) In the first stage, the passive layer is penetrated by chloride ions, and the pit nucleates.
2) In the second stage, a pit is formed.
3) In the third stage, a metastable pit develops and grows.
4) In the fourth stage, a stable pit is formed and grows.
5) In the last stage, the pit's growth stops.

Fig. 2.7 shows the chemical reactions which procced during the formation of the pit at the surface of magnesium or its alloy.

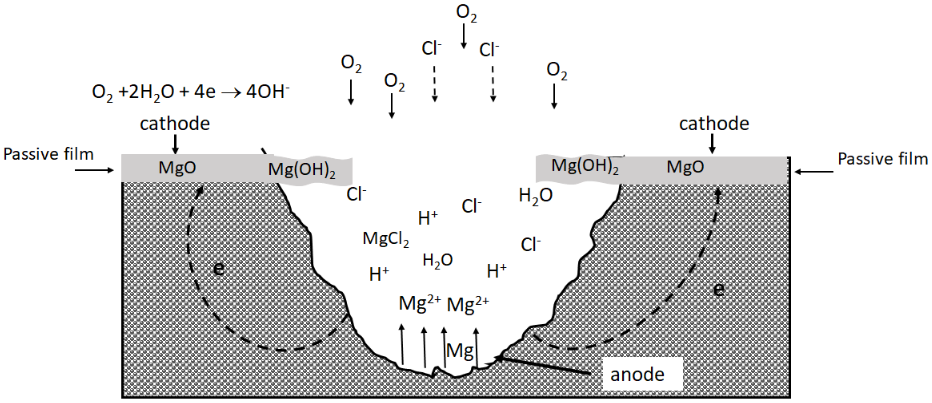

Fig.2.7. Diagram of the formation and growth of a stable pit on the surface of magnesium immersed in an aerated solution containing chloride ions.

Inside the pit, magnesium dissolution reaction takes place, reaction equation (2.8). Magnesium cations are formed inside the pit, then they react with chloride ions and the $MgCl_2$ salt is formed, reaction (2.23).

$$Mg^{2+} + 2Cl^- \rightarrow MgCl_2 \tag{2.23}$$

Magnesium chloride undergoes a hydrolysis reaction (reaction equation (2.24)) during which hydrogen ions are formed.

$$Mg^{2+} + 2Cl^- + 2H_2O \rightarrow Mg(OH)_2 + 2H^+ + 2Cl^- \tag{2.24}$$

The formation of hydrogen ions in the reaction (2.24) leads to the acidification of the solution inside the pit’s, resulting in the acceleration of magnesium dissolution and the growth of the pit’s. Electrons released during the anodic dissolution reaction migrate to the magnesium surface outside the pit, and they are consumed there in the cathodic reaction (2.17). The surface of the metal outside the pits works as a cathode, and here the cathodic oxygen reduction reaction takes place, equation (2.25).

$$O_2 + 2H_2O + 4e \rightarrow 4OH^- \tag{2.25}$$

The hydroxyl ions react with the magnesium surface and $Mg(OH)_2$ is formed as a corrosion product. The formation of OH^- ions during cathodic processes contributes to an increase in pH in areas working as cathodes.

There are a few ways to prevent pitting corrosion:

- Remove chlorides and oxidizers, such as from dissolved oxygen, from the environment. In the case when corrosion occurs in the human body it is impossible to remove those ions from the solution because body solutions contain high concentrations of Cl^-
- Application of proper material selection, alloying and heat treatment.
- Avoiding stagnant (without flow) conditions, which help to develop aggressive conditions inside the pits. The human body always has flows of blood and other liquids.
- Using inhibitors. It is known that SO_4^{2-} and NO_3^- ions provide the reduction of pitting corrosion. However, in the case of biomedical applications it is difficult to introduce corrosion inhibitors into the body fluids.
- Application of cathodic protection – application of protective coatings.
- Application of proper surface treatment.

To prevent the pitting corrosion of magnesium alloys in the body fluids it is possible to choose a suitable chemical composition of Mg alloys and/or the application of a proper surface treatment.

2.5.4. Crevice Corrosion

Crevice corrosion is a type of localized corrosion that occurs inside small crevices, at welds and other shielded areas on a metal surface exposed to aggressive environments [94]. A crevice is generally related to a small volume of stagnant solution caused by holes, gasket surfaces, lap joints or surface deposits. This type of corrosion occurs when there are some entrances to the crack for the aggressive solution, as well as a narrow exit that traps the corrosion products inside the crack [87]. Oxygen access to the crevice is impeded, however the oxygen present in the crevice is quickly consumed during the cathodic reduction. This causes the solution in the crevice to be deplted of oxygen molecules, making it difficult to maintain the passive state, which leads to the metal's dissolution [94]. In the Fig. 2.8. are illustrated crevice corrosion – a) schematic illustration where corrosion starts; b) example of corrosion that had happened in favorable conditions. Factors that affect the kinetics of crevice corrosion include the chemical composition of the alloy, the alloy's ability to passivate, the type of crevice, the geometry of the crevice, the chemical composition of the corrosive environment, the presence of oxygen, and mass transport in and out of the crevice.

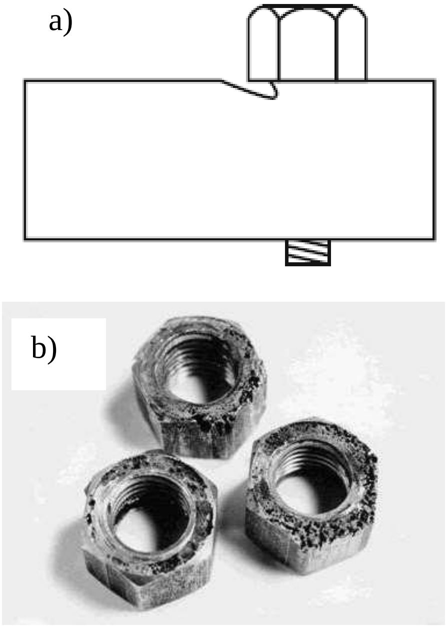

Figure 2.8. Crevice corrosion. a) place, where corrosion starts; b) nuts destroyed within crevice corrosion [64].

It is very important whether a crack forms between two metallic surfaces, between a metal and a non-metal, between a metal and a mud deposit or a layer of growing biological organisms. Each of these surfaces affects the kinetics of crevice corrosion. The alloy's passivation ability is a very important factor that can slow down crevice corrosion. Crevice corrosion is closely related to any changes in pH. When the pH of the electrolyte decreases inside the crevice or hole, the corrosion rate increases, but at the same time it works for cathodic protection of the external cathodic surface of the metallic material. Furthermore, the separation of the cathodic reaction on the surface and the anodic reaction inside the crevice promotes corrosion [87]. Crevice corrosion generally emerges in an environment containing a high number of Cl^- ions such as in seawater or body fluids, as well as in small details where holes or crevices could appear. Other factors that may have an influence on corrosion production are sand, dirt, corrosion products and other solids [63]. Crevice corrosion can appear because of contact between metal and nonmetallic surfaces – wood, plastics, rubber, glass, concrete, asbestos, wax and fabrics [63]. The mechanism of crevice corrosion is similar to that of pitting corrosion.

For biodegradable implants, crevice corrosion is a very serious problem. The connection of the implant to the bone results in the formation of small gaps. Studies of crevice corrosion of pure magnesium joined to resin were performed in phosphate-buffered saline (PBS) with different crevice widths. The corrosion rate of the magnesium plate was 8 times higher in a 1.5-mm-wide crevice compared to a freely corroding Mg wafer (0 mm width) [104]. With increasing crevice width, the corrosion rate of magnesium increased. The main products of crevice corrosion were hydrated magnesium and potassium hydroxyphosphates: $Mg_2(PO_4)(OH) - 3H_2O$ and $MgK(PO_4)(OH) - 3H_2O$.

To achieve resistance of crevice corrosion it is important to control active-passive states of the metal:

- a narrow active-passive transition
- a low critical current density
- a continuous passive region [63].

Crevice corrosion cannot be eliminated but it can be effectively reduced. Crevice corrosion can be prevented by joining materials with welds, sealing gaps with non-conductive materials, and by avoiding metal contact with hygroscopic materials, plastic, debris, or sediment. The construction or object should be designed to avoid sharp edges, sharp angles and recesses where sediment could accumulate. Crevice corrosion can also be prevented by an appropriate selection of materials that exhibit high corrosion resistance, such as titanium alloys or steels containing alloying elements, such as chromium and molybdenum. In the systems operating in seawater the water flow rate should be kept at such a level that no sediment is deposited on the construction to avoid crevice corrosion.

2.5.5. Filiform Corrosion

Filiform corrosion is a type of corrosion that takes place in coated or plated samples. Generally, this type of corrosion is typically associated with a metal surface covered by protective coatings, lacquers, "quick-dry" paints or highly resistant oxide films. When the moisture penetrates through a coating to the metallic material, filiform corrosion begins to form [94]. To avoid this problem, the coating should provide excellent adhesion and demonstrate a high resistance to water vapor [94].

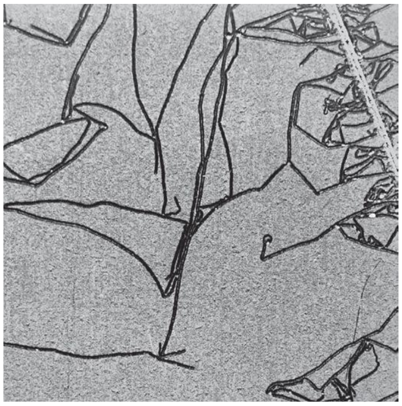

Figure 2.9. Filiform corrosion

Filiform corrosion has been observed under several paints on different metals – steel, zinc, aluminum, magnesium and chromium-plated nickel [76]. In Fig. 2.9 is illustrated example of filiform corrosion on clear varnish on steel [76].

Corrosion filaments consist of a mobile head filled by electrolyte and a tail of a dry, porous corrosion product. The electrolyte in the head contains metal cations and aggressive anions (such as Cl^-). Filiform corrosion (FFC) head regions typically exhibit a low pH due to the hydrolysis of a cation. The driving force for filament is differential aeration, arising from mass transport of gaseous O_2 through the filament-tail. The oxygen concentration cell formed directs anodic metal dissolution towards the leading edge of the filament-head, while the cathodic oxygen reduction lies towards the trailing edge of the active head. Chloride anions (Cl^-) and water are in the filament head electrolyte and corrosion filaments are propagated for long periods of time (a few months).

Compared to previous corrosion types. filiform corrosion is much easier to detect during the early stages and is much easier to solve for when it comes to the damaged places.

Filiform corrosion control:

- ✓ takes care of pretreatments before coating application on the metal surface;
- ✓ galvanizing metal surface with zinc or chromate compounds – for specific applications, not a case for biomedical implant materials;
- ✓ double coating system – applications of two different coatings on one material;
- ✓ humidity control, about 60% [105].

One of the ways of decreasing filiform corrosion is via phosphate surface pretreatments and chromate coats. This will help to limit filiform corrosion, but not completely eliminate it [76]. Chromates provide a bad influence on the human body, so it is not used to apply as a pretreatment for biomedical materials (implants).

Chapter III

Surface Modification Techniques Used for Biomedical Mg Alloys

Corrosion is a phenomenon that starts on the surface of metals or alloys. Scientists and material science engineers have always been searching for surface analysis techniques to detect when corrosion begins to take place [60]. To improve the corrosion resistance of metals and alloys, their surface must be modified. For biomedical applications, surface modification of alloys is one of the critical factors that determine whether an implant will be accepted or rejected by the human body. Traditional materials for implants such as stainless steel, Ni-, Ti-, and Co-based alloys are bioinert, unlike Mg and its alloys which are not bioinert [27]. Biocompatible Mg based materials could be surface treated in three general ways: via mechanical treatment, physical modification or chemical modification.

Surface modification is the process that affects surface properties to enhance desirable properties of the material (in the case of Mg alloys for biomedical applications this means a decrease in corrosion rate). Surface treatments are oriented toward improving material and biological responses through changing material surface chemistry, energy, charge and topography without changing the bulk properties of the implant [106] [107]. The main purpose of the surface modifications of biomaterials is to improve corrosion resistance, bioadhesion, antibacterial properties and biocompatibility as well as to improve mechanical properties. The idea is that surface modifications will promote interaction between the implant material and the cells of the biological environment [106].

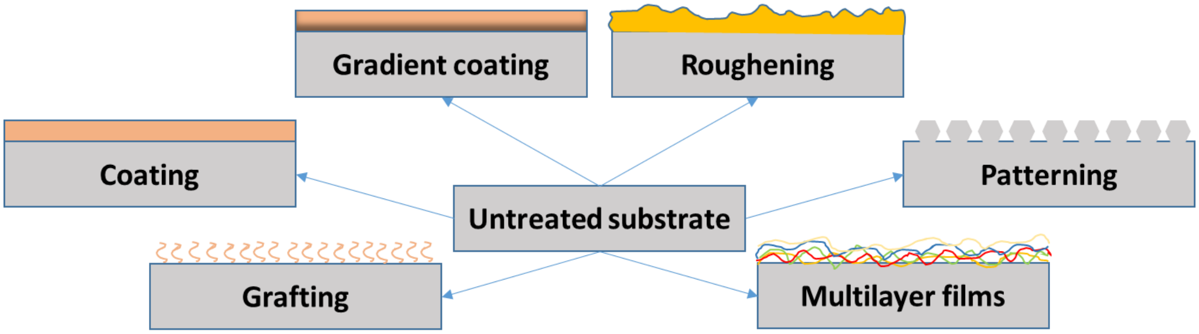

Figure 3.1 Schematic diagrams of surface modification techniques [108].

Fig.3.1 is shown the schematic diagrams of surface modification techniques, classified by Zhi-Ye Qiu and others in their paper [108], and modified according to the needs of this work. This work is more oriented on the surface treatment typical for Mg and its alloys. Critical factors to choose the most suitable method of surface modification depend on the substrate material, the final application of the material, design and geometry of the material as well as the financial aspects such as the cost of the preparation and production and also of the surface engineering process and coating thickness [109]. Surface preparation of Mg alloys should always start with surface cleaning. A perfectly clean sample surface promotes better adhesion, especially when coatings are applied. It is important to remove the MgO layer that covers the surface of the Mg alloys because it is responsible for coating adhesion [110]. There are two types of surface modifications – physical and chemical or electrochemical treatment, which are classified into smaller groups, as is presented in Fig.3.2. These surface treatments can be applied for modification of Mg and its alloys used for biomedical applications [109].

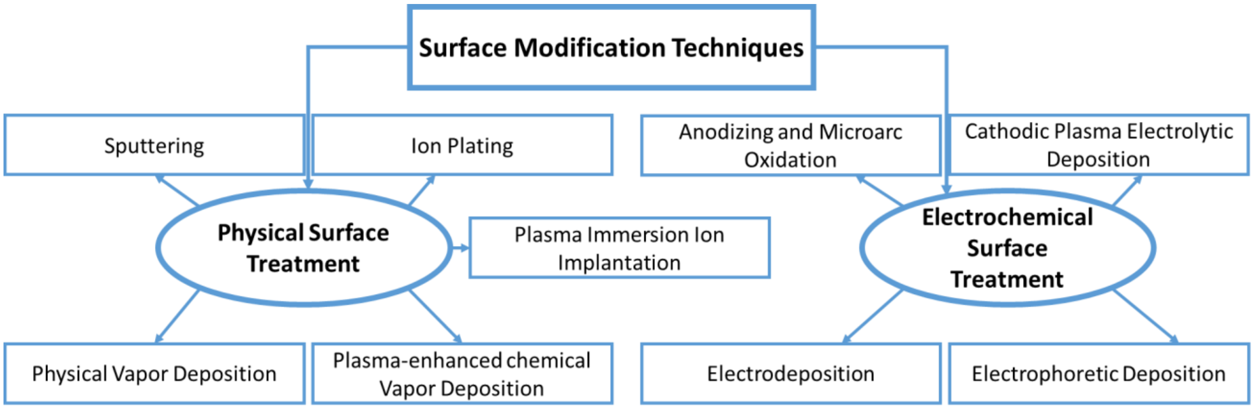

Figure 3.2. Classifications of surface modification techniques for Mg and its alloys for biomedical applications.

In previous chapters, it was mentioned that there are a few ways of corrosion control of magnesium alloys for biomedical applications – compositional modification via the addition of different alloying elements [111] (elements that are body-friendly, non-toxic, non-allergic, biocompatible metals or non-metals), surface treatments either physical or chemical [112] and surface modifications by using biopolymer coatings [113].

3.1. Physical Surface Treatment

The critical characteristics of magnesium alloys such as poor wear resistance and low corrosion resistance may limit its applications in different fields, especially in biomedical applications. To solve these problems, the physical surface modification of magnesium alloys can be used. This could be made by commonly used plasma surface treatment or the plasma spraying technique [114]. Fig. 3.3. is shown the classification of physical surface modification techniques.

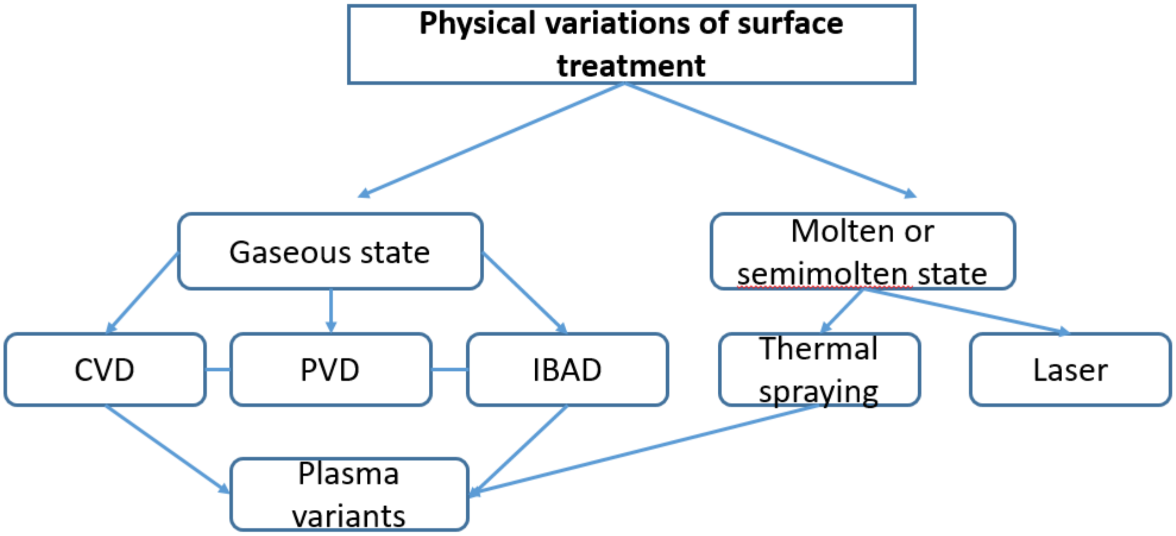

Figure 3.3. Classification of physical surface modifications [115].

3.1.1. Plasma Surface Treatment

In Figure 3.2 is shown methods of plasma surface modifications, which will be, described more in detail in this paragraph. Plasma is the fourth state of matter, similar to matter as a liquid, gas and solid [116]. Plasma is an ionized gas [117]. Plasma is made of positive ions, free electrons, high-energy atoms and molecules in specific conditions (atmospheric, high-pressure, and low-pressure conditions) [116] [118]. It is formed by ionizing atoms or molecules of plasma gas to produce free electrons and positive ions. This ionization for plasma generation is mostly carried through electrical power but can also be created by shock wave excitation [118]. Specific plasma surface modification techniques such as Plasma Deposition and Plasma Implantation may modify the surface of the material. It is possible to influence adhesion (increase or decrease), corrosion resistance and wear resistance of the material [117].

There is a classification of plasma treatment related to their degree of equilibrium and exploitative pressure [116]. The thermal equilibrium of the plasma is determined by the corresponding temperature of electrons, ions, and other parts inside the plasma. It is attributed to the degree of equilibrium. Due to these factors, plasma is divided into thermal or hot (high temperature) plasma and non-thermal (cold plasma). Thermal plasma has electrons and heavy particles at the same temperature, that is, they are in thermal equilibrium with each other. Non-thermal plasma, on the other hand, has ions and inert particles at a temperature much lower (generally room temperature) than that of the electrons. Compare to thermal - non-thermal plasma is not in thermal equilibrium. In this case, the plasma temperature is determined by the temperature of ions (that is close to gas temperature) and that value is much lower than the temperature of electrons [116]. Low-temperature plasma surface modification is extremely attractive in the case of polymeric materials. It helps increase surface properties such as adhesion, wettability, biocompatibility, and permeability avoiding thermal damage [119]. The next important classification of plasma is made by exploring pressure. Thermal plasma is operating at high pressure and non-thermal plasma - at low pressure, respectively. Moreover, it has been reported that non-thermal plasma could operate under atmospheric pressure [120]. Because the low-pressure density of gaseous molecules and atoms is also low and that is affecting on the collision rate and making it lower as well [120]. In these conditions, electrons reached thermodynamic equilibrium much faster than ions and neutral particles. According to those facts, it is used to work with non-thermal plasma as a surface modification for biomedical implants. It is reasonable to mention that there is an expressive difference between plasma surface modification of hard and soft tissues. Hard tissues are attributed to mineralized tissues, such as bones and joints. Soft tissues unlike hard tissues are responsible for other body structures like fibrous tissues [121-123].

Plasma treatment technologies are used to modify metallic biomaterial surfaces at the atomic and molecular scale (physical and chemical transformations of the surfaces) and through coating materials surfaces with different chemical compositions [124]. Plasma surface modification techniques of Mg and its alloys for biomedical implants have many advantages such as:

- Easy preparation;
- Good adhesion between coating and substrate;
- Uniform film chemistry;

- Excellent penetration;
- Conformal films;
- Sterile conditions of preparations [107,120].

The supplied power to the plasma and the nature of the substrate material has an influence on the penetration of the ions through the plasma sheath and applied energies [125].

3.1.1.1. Physical vapor deposition

Physical Vapor Deposition is a method of material deposition in which the deposited material is converted from a condensed phase to a vapor phase and then back to a thin film condensed phase. During the condensation of vapor, a thin film of material is deposited on the substrate. Physical vapor deposition can be used to produce thin films and coatings. PVD films could be reactive or non-reactive. There are advantages that are making PVD favored for physical surface modifications: high coating density, strong adhesion between coating and substrate, multicomponent layers, low substrate temperature and numerous combinations of coatings and substrate materials [107].

On Fig. 3.4. is schematically illustrated the production of PVD coatings [126]. The PVD method includes three stages: evaporation, sputtering and ion plating [127].

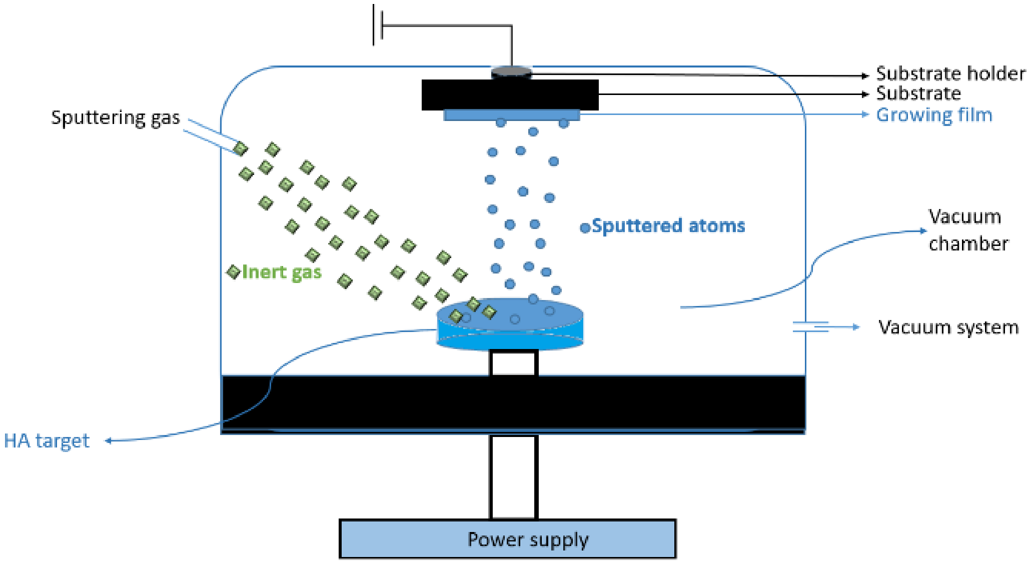

Figure 3.4. A schematic illustration of Physical Vapor Deposition (PVD) for HA coating deposition [126].

Evaporation and sputtering processes, depending on the composition of the materials for the film production provide the possibility to manufacture coatings with specific functional properties in the atomic or nanoscale [107]. In PVD, the influence of temperature and pressure on the morphology of the coating and the material's surface topography can be controlled. The production of coatings by means of the PVD technique allows for the control of corrosion and wear resistance of materials [107]. The ability to control temperature during the coating production process makes the PVD method more attractive for surface modification of materials. However, decreasing the temperature to room conditions could lead to the formation of defects [110]. The reduction in temperature during the PVD process is particularly intriguing for thin film formation on Mg or its alloy substrates. It is possible to produce a coating that, on one hand, improves corrosion resistance but, on the other hand, may deteriorate the mechanical properties of the material [110]. The application of PVD surface modification is limited in Mg and its alloy applications due to the inherent softness of Mg. While magnesium is a soft metal, it is possible to modify its physical properties through alloying and increasing material hardness, thus identifying suitable applications for these alloys. In principle, the use of PVD for modifying magnesium surfaces is not an ideal solution, especially for bioimplants [128].

3.1.1.2. Chemical vapor deposition

Chemical Vapor Deposition (CVD) is a method of surface modification in which the substrate is exposed to one or more volatile precursors, which react on the substrate surface to produce the desired deposit. The solid material is deposited from vapor by a chemical reaction occurring on the heated substrate surface. During the deposition by means of CVD, volatile by-products are frequently produced, which are then removed by gas flow through the reaction chamber [127]. It is necessary to control the reactions that proceed between coating and substrate as well as between substrate and by-products [129]. By means of CVD, it is possible to get a thin film of highly pure materials. Furthermore, using this method it is possible to produce single, multilayer, composite materials with controlled shapes and unique structures as well as low processing temperatures [127]. It is possible to use metals, alloys, semiconductors and heat resistant substances as deposits on the material's surfaces [129]. CVD has been used for refractory metals production (Ni, Ti, Zr, Ta), due to the possibility of getting high purity metals after the application of this process [127]. On Fig.3.5 is illustrated the simplified scheme of the CVD reactor used for the production of carbon nanotubes (CNTs) coatings [130].

During the CVD process, there are three steps that take place at the same time at the substrate, and it is impossible to control independently each of them:

- Production of vapor from the chemical compound or element that will be deposited;
- Transporting the gas or vapor between the source and the material's substrate;
- Film formation due to the vapor condensation process [129].

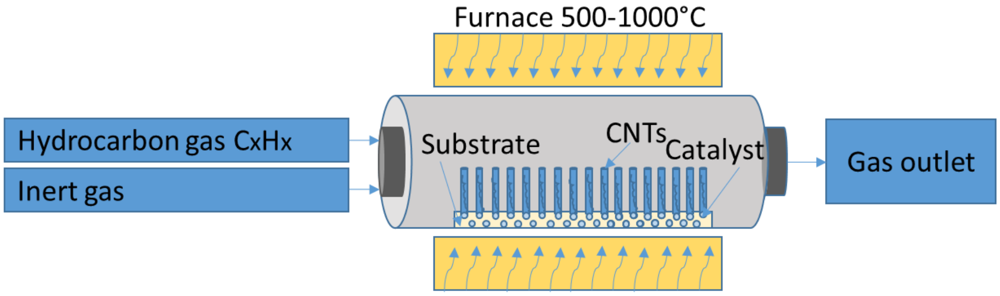

Figure 3.5. Simplified scheme of a CVD reactor for CNTs synthesis [130].

The critical parameter for film formation by means of CVD is a substrate temperature that has an effect on the final microstructure and on the properties of the deposited material [115, 129].

There are various modifications of the CVD method, such as atmospheric-pressure chemical vapor deposition (APCVD), low-pressure chemical vapor deposition (LPCVD), plasma-enhanced chemical vapor deposition (PECVD) and laser-enhanced chemical vapor deposition (LECVD) [131].

Advantages of the CVD method:

- Possibility to deposit highly dense and pure film.
- Possibility to produce uniform films with good adhesion within the substrate.
- The CVD method can be applied to coat non-line surfaces, with different shapes and orientations of the substrate with uniform thin film growth.
- CVD can be applied to produce inorganic nanostructures.
- It is easy to control the nanofeatures, crystal structure and surface morphology through controlling CVD parameters.
- The costs for the CVD process are affordable.

- A ide range of chemical precursors (halides, hydrates, and organometallics) can be used to form films using the CVD method.

Disadvantages of the CVD method:

- Fast gas flow is claimed.
- The deposition takes place everywhere.
- The properties of the produced film are based on its homogeneity.
- If the substrate is brittle, it could be damaged during the deposition.
- It is important to clean the reactors constantly. It is difficult to deposit multi-component coatings because it is desirable to use different precursors.
- It is extremely important to follow safety restrictions, because for some films formations use toxic, corrosive, and flammable (explosive) precursors [127], [116].

"Summarizing the advantages and drawbacks of this surface modification method, it can be concluded that the CVD process has found applications in the fabrication of microelectronic devices, in coating production with complex geometries, and has carved a niche for itself in altering the mechanical properties of titanium and its alloys for biomedical applications. However, the CVD process has not found application in the surface modification of Mg and its alloys [132]."

3.1.1.3. Sputtering

Sputtering is a commonly used surface treatment method to deposit thin film coatings that provide improvement of surface properties such as corrosion resistance, biocompatibility, and increased bioactivity [132]. Sputtering is a physical vapor deposition technique used for the formation of thin films. The solid material (target material) is bombarded by energetic particles of plasma or gas, then microscopic particles of solid material are ejected from its surface. The ejected particles

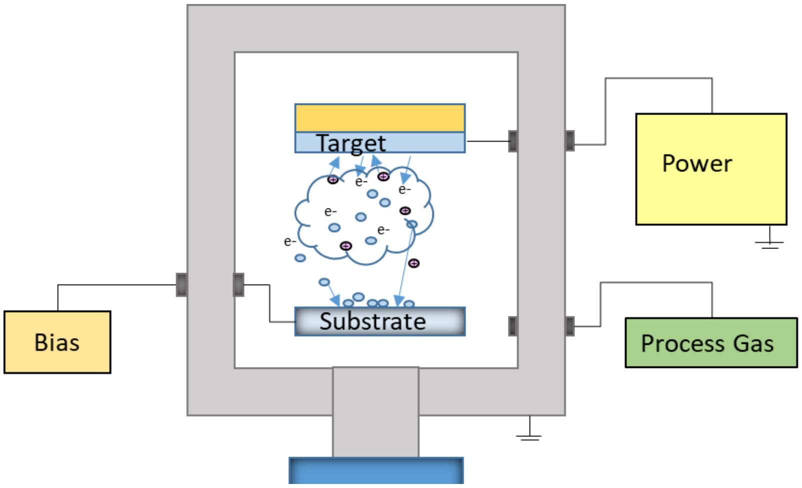

Figure 3.6. Schematic illustration of spattering principle

from the target are deposited on the substrate. Sputtering also can be explained as a relation between the number of sputtered atoms to the number of energized particles, mainly ions [94, 129].

Spattering is a multipurpose process for coating deposition of metal alloys, compounds, and non-conductors on the materials surfaces [62]. In Fig. 3.6. is shown the principle of spattering process.

This surface modification method has been commonly used in industrial hard and protective coatings [60]. It is possible to deposit nitrides and carbides with the help of the sputtering method to derive dense films. Those films have high hardness, low porosity, good conductivity and are chemically inert. Simultaneously to existing technology, there is research oriented on the improvement of the sputtering method for the modification of hard ceramics from poorly coated surfaces, without damage to the material [60].

"The most significant technique in sputtering is magnetron sputtering. This technique serves as the foundation for magnetron discharge [129]. The sputtering process has become more efficient with the development of high-performance magnetron sputtering sources. These sources have enabled comparatively high deposition rates over substantial areas while maintaining low substrate heating [132]." The advantages of the magnetron sputtering technique is adaptability in adjusting the thin film composition and its thickness [133]. Because of the advantages of the technique, magnetron sputtering acquired widespread use in the production of thin films [134]. During the magnetron sputtering deposition process, reactive gases such as O_2, N_2, C_2H_2 are used. This has made it possible to perform the deposition of thin films with complex chemical composition. In addition, sputtering uses inert plasma operation, which can promote some impurities from the plasma gas that support the layer growth process [62]. Due to the possibility of using low temperatures during the deposition process, most metallic layers (Al, Cu, Ni) for functional applications are produced by electroplating or sputtering instead of PVD or CVD [127].

3.1.1.4. Ion beam-assisted deposition

Ion beam assisted deposition (IBAD) is a surface modification technique that is focused on growing thin films with energetic ions. The idea is that the substrates are smooth, without texture, while the textured coatings are applied directly on the surface to provide epitaxial growth of the films [135]. It is extremely convenient that during the IBAD process, it is possible to alter deposition conditions such as ion energy and deposition velocity. This capability enables the creation of various film structures and the mixing of binary metal materials, similar to what can be achieved using the ion-beam mixing method [136]. IBAD is a vacuum surface modification technique that combines two other techniques – PVD and ion implantation [108]. In Fig. 3.7. is demonstrated the graphical principle for IBAD coatings production. Coatings produced by IBAD are much thicker (thickness in the range of microns) compared to the coatings gained by ion implantation. Moreover, thin films deposited by this method show better adhesion than PVD coatings, which could be explained by the partial melding of the film with the material substrate by an energetic ion source [64]. The IBAD technique has been widely used for the surface modifications of biomedical materials in recent decades. The main application of the technique is the production of hydroxyapatite coatings on metal surfaces, such as Ti or its alloys, or the production of metallic, bioceramic and composite thin film coatings for different biomaterials as an implant material [137], [138]. In the case of Mg biomedical alloys, IBAD is used to deposit CaP protective coatings [139]. Those coatings (CaP) provide good adhesion between the coating and the substrate as well as higher corrosion resistance and longevity compared to uncoated alloys [139]. The main disadvantage of the IBAD technique is that it is used for straight or line surfaces, so in the case of convex surfaces this method of coating application is inappropriate [108]. One of the substantial applications of the IBAD process is the improvement density of the coatings and the improvement of the refraction index of various oxide films used for optical coatings [27].

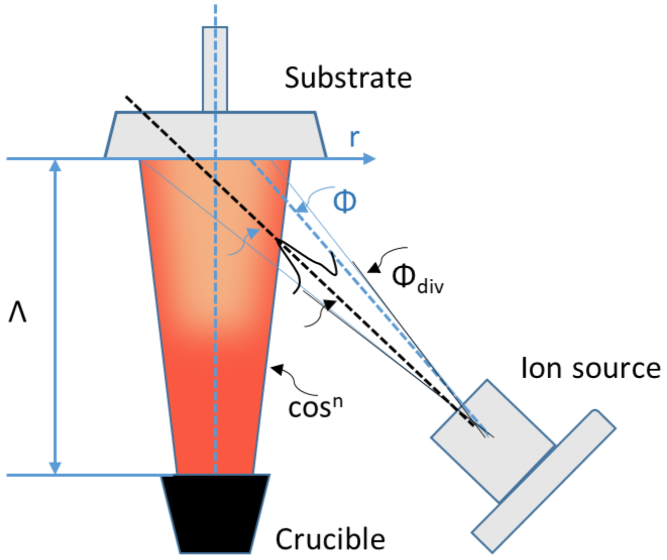

Figure 3.7. Schematic illustration of IBAD principle.

3.1.2. Laser Surface Treatment

Laser methods of production or surface modifications of Mg alloys enhance the corrosion resistance and mechanical properties of biomedical Mg alloys [140]. Applications of laser surface treatments (laser surface alloying, pulsed laser deposition and laser surface melting) to alter the surface properties or coatings on Mg alloys are environment-friendly methods of surface modification. Moreover, laser surface treatment significantly reduces the risk of waste [59]. The application of those methods in industry is limited. That said, those methods make it possible to modify the material composition and produce the needed structure to improve wearing, reconstruct the shot part of the material, work in high temperature conditions, increase corrosion resistance and improve mechanical properties [60].

Laser surface treatment has many advantages unlike physical and chemical surface treatments, such as:

- Can be applied to samples with different sizes and shapes.
- Provide excellent adhesion between material and deposited coating.
- Has lower heat-stricken area.
- It is easy to control and reproduce the treatment process.
- It is easy to calculate and predict the appearance of the coating [141].

3.1.2.1. Laser surface alloying

During laser surface alloying (LSA), high heat energy is used to melt the metal coating through a laser and a portion of the underlying substrate. "The laser surface alloying method, when used in conjunction with an inert gas flow, is employed for materials that are prone to oxidation. Deposition speeds are determined by laser power, powder supply rates, and traverse rates [60, 141]. There are exceptions to using this method for easily oxidizing materials, such as aluminum, due to the presence of a brittle oxide layer, which can lead to the formation of cracks and stratification. Like all other surface modification methods, laser surface alloying has certain limitations. In this case, the coating surface must have specific dimensions, as the working area is restricted due to the small size of the laser beam [60]. The principle of the laser alloying process is the production of a new alloy with the help of a laser by mixing substrate with a coating or renovation of an existing alloy/coating that has been partially destroyed [142].

3.1.2.2. Pulsed laser deposition

The principle of the pulsed laser deposition (PLD) method is based on the interaction between the laser beam and a target. As a result of this interaction, the material is transported via a plasma plume to the collector, where thin films are formed [143]. In the PLD method, a high-power pulsed laser beam strikes a target of the material that is to be deposited. Then, this material is vaporized from the target and is deposited as a thin film on a substrate. This process can occur in an ultra-high vacuum or in the presence of a gas, such as oxygen, which is commonly used during the deposition of oxides films. The pulsed laser deposition (PLD) surface treatment method has found application in the deposition of calcium phosphate for the modification of biomedical materials [109, 144]. PLD is a surface modification method that enables the deposition of thin films [145], which are crystalline and exhibit high adhesion levels [146]. It is primarily used to deposit hydroxyapatite onto the surfaces of biomedical materials through high-temperature processing [145]. PLD has various advantages, which are making this method quite popular among many surface treatment methods. The main advantages of the PLD method are:

- The laser is placed out of the chamber as a result, there is no need for frequent cleaning of the reactor.
- It is easy to control the deposition process, because of laser parameters, such as the repetition of laser pulses, wavelength, and others.
- The coating thickness is simultaneously controlled with the deposition process through the quantity of the pulse’s attack target material.
- The opportunity to produce new materials in metastable states [143].

It is reasonable to mention that traditional plasma surface modification methods and laser surface treatment methods that used to be applied on classic biomedical alloys such as Ni, Ti alloys, and only occasionally on stainless steels, could be used for biomedical Mg alloys [27]. Unlike them, PLD has found its application in the surface treatment of Mg biomedical alloys [143].

3.1.2.3. Selective laser melting

Selective laser melting (SLM) is a laser surface modification technique or additive manufacturing technique used for accomplishing strong metallic structures [147]. SLM is a localized surface treatment method [148] that is mainly used for advanced surface finishing [140]. SLM is supported by a fast-melting process of the thin surface layer of the metal following rapid solidification and simultaneous deposition of a new modified layer on the surface of the material. The fast-cooling rate of around 106-107 K/s results in a reduction of the grain size of the material [140]. Consequently, corrosion resistance, microhardness and wear resistance properties are strongly connected with the microstructure of material. The grain's refinement substantially improved these properties. This is not the only advantage of SLM surface treatment, furthermore, there are:

- By means of SLM, it is possible to deposit thin films.
- It is possible to control scanning laser trajectory, which will help to avoid damages or deformations which could be concomitantly generated during the process because of thermal stress.
- SLM surface treatment is an environment friendly method, which does not produce harmful substances, and has no negative effects on human health.
- SLM reduces material usage compared to other manufacturing methods.

Disadvantages of SLM:

- Only metals and materials with good flow characteristics can be used for in SLM.
- SLM is a high-energy process, leading to temperature gradients that can create the formation of stress in the material.
- SLM requires a source of inert gas
- SLM parts have a rough surface finish and they require post-processing.

Therefore, this method is used to process biomedical materials, including Ti-Al-Mg alloys, Ni-based alloys, stainless steels, and various other advanced alloys [147]. Biomedical Mg alloys are also no exception to this method [140].

3.2. Chemical Surface Treatment

The chemical surface treatment produces hydrogen on the surface of magnesium alloys especially in acidic conditions such as during phosphatizing pretreatments [100]. There are numerous chemical surface modification methods utilized for the improvement of biomedical Mg alloys, such as chemical conversion coatings, electrochemical treatments, sol-gel coatings and biomimetic, organic, and polymeric coatings [27]. The chemical reactions which occur on the surface of Mg alloys cause the modification of their properties. The main idea of chemical surface modification for biomedical materials is to support the desirable adhesion of proteins, cellular and tissue while providing for the penetration of body fluid through the coating to the implant [117]. Moreover, many efforts and a great deal research are focused on the production of coatings that exhibit antibacterial properties.

3.2.1. Chemical Conversion Coating

Chemical conversion coatings are the type of coatings that can convert an active material surface to a passive one [125]. Chemical conversion coatings are part of the smart self-healing coatings. The principle of formation of chemical conversion coatings is the production of a protective oxide layer via immersion of the material into a chemical solution [149]. The reaction between the metal surface and the components of the solution causes the oxidation of the metal and the formation of the oxide film. These coatings are distinguished from other surface modification methods because of the uncomplicated process and low costs of production [150]. Chemical conversion coatings can be divided into different groups depending on the main chemical compound present in the coating: chromate conversion coating, stannite, phosphate, and organic-acid conversion coating, which are generally deposited on industrial Mg alloys – AZ91, AZ31, AM60 [151]. Chromate conversion coatings increase the corrosion resistance of Mg and its alloys. Due to the toxicity of chromate ions, these coatings cannot be used for biomedical applications [110]. Unlike the chromate conversation coatings, the phosphate coatings found various applications in improving the corrosion resistance of metals, especially for magnesium biomedical alloys [152]. Moreover, phosphate coatings are simple to deposit, need comparably low costs for their production, have no bad influence on the human body and are also non-toxic [150]. Chemical conversion coatings may be deposited to improve the corrosion resistance of the materials, as well as increase adhesion between the material and other protective coatings [153]. The advantages of this surface modification method are the possibility to create a coating on various materials' geometries, an opportunity to adapt temperature, and the elimination of the need to use high voltage or specific equipment to get a protective layer [154].

3.2.2. Electrochemical Treatment

Electrochemical surface treatment is a method of surface modification during which protective oxide layers are formed. Electrochemical surface treatment for biomedical applications can be performed in four different ways:

- Anodic oxidation;
- Cathodic polarization (ELD);
- Electrophoretic deposition (EPD) [117]
- Electrodeposition.

Anodic oxidation (or anodizing) is the electrochemical surface modification method where two electrodes, operating as an anode and cathode, are immersed in the electrolyte and connected to a power source. The application of anodic voltage to one of these electrodes causes the formation of an oxide layer on its surface. Anodizing reinforces the oxide film that is formed on the metal surface and improves the corrosion resistance of the material. The oxide layers can also serve a decorative function [100]. It is possible to control film growth during the anodizing process by adding a few drops of color pigment to the working solution. Anodic oxidation is widely used to reinforce natural oxide films that are formed on valve metals (Ta, Nb, Zr, Al, Ti, Hf, W) owing to their low electrochemical potential and excellent reactivity with water or oxygen [155]. With the help of anodizing, it is possible to deposit a thick and stable oxide film on a metal or alloy surface to enhance the chemical, physical or mechanical properties of the material used for engineering applications [109]. This surface modification method is used to increase the thickness of the protective oxide layer [94], improve corrosion and wear resistance [109] and enhance adhesion between the metallic material and the protective coating. Moreover, films that are produced by anodic oxidation are biocompatible [156]. Anodizing does, however, have a drawback – the porous structure of the oxide film, which should be sealed [156]. The presence of porous anodizing oxide film has a negative influence on the corrosion resistance of the metal and its alloys. In the last few years, it has been widely investigated for orthopedic biomaterials covered by nanotubes and nanostructures layers. Anodization is one suitable method to produce those nanomaterials [157]. The most attractive nanomaterials used for biomedical applications are TiO_2, ZnO, Ag nanoparticles and titanium dioxide nanotubes.

Cathodic polarization or as it is sometimes called **electrolytic deposition (ELD),** is a surface modification method where two anode and cathode electrodes are immersed in an electrolytic bath. The material on which the inorganic film will be deposited works as a cathode. During electrolysis, the inorganic film grows on the cathode surface because of the electrochemical [117]. "This method has primarily been applied in the production of calcium phosphate (CaP) coatings on the surfaces of implants used in cardiovascular applications, such as stents [158]. The cathodic polarization method is commonly employed to enhance the corrosion resistance and mechanical properties of Ti-Ni biomedical alloys, which are less sensitive to pH fluctuations compared to Mg and its alloys. Consequently, Mg alloys are not suitable for surface modification via electrolytic deposition due to the high pH values observed at the cathode surface during the electrochemical deposition process [159]."

Electrophoretic deposition (EPD) has been selected as a convenient surface treatment method to obtain uniform, thin and dense coatings (ceramic, polymer, composite) on metal/alloy surfaces for various applications including orthopedic implant materials [160]. Electrophoresis is based on the migration of colloidal particles suspended in a liquid medium under an electric field which are then deposited onto an electrode [161]. This method is extremely attractive for the bioactive surface modification of metallic materials and can be used for various biomedical applications. The following advantages of the electrophoretic deposition method (EPD) can be listed:

- the coatings deposited by means of EPD are uniform and exhibit good consolidation [146];
- by using the EPD method, it is possible to deposit coatings on various surfaces and shapes of samples. Coatings can be deposited on materials with complex geometries. [160];
- it is easy to control the coating deposition parameters [162];

- the financial side of the process is very attractive – low cost production as well as the simplicity of the deposition process [163].

In addition, it is possible to deposit nanoparticles (for example, TiO_2, ZrO_2, Al_2O_3) to modify the metal surface and improve its biocompatibility [164]. Hydroxyapatite coatings can be easily deposited on the surface of magnesium alloys by electrophoretic deposition [146]. Hydroxyapatite (HA) coatings improve the corrosion resistance of biomaterials and the adhesion of biomolecules.

The electrodeposition process involves applying an appropriate difference of potential between two electrodes immersed in an electrolyte and forming a protective coating on one of the electrodes, usually the cathode. The coating is deposited due to electrochemical reactions occurring at the electrodes (cathode and anode) [59]. The main advantage of this method is that the thickness and chemical composition of the deposited layers can be controlled by varying the chemical composition of the electrolyte, potential or current, and deposition time [109]. Electrodeposition can be carried out in a potentiostatic or galvanostatic manner. The pulsed current option makes electrodeposition more attractive compared to direct current and offers the possibility of producing high-quality coatings. Furthermore, it has been investigated that the use of very high voltages during the electrodeposition process promotes poor corrosion properties of coatings [164]. The kinetics of the electrochemical reactions occurring during electrochemical deposition depend on the concentration of metal ions in the electrolyte solution, temperature, potential or current values and the presence of complex compounds [100]. Electrodeposition is a well-suited method to produce small details and has found widespread use in the automotive [59] and electronics industries [100]. In the case of Mg alloys, electrodeposition in a range of other surface treatments can help to control excessive corrosion rate by forming protective and corrosion resistive layers that can concomitantly improve its functional facilities [165]. It has been investigated that Mg alloys with poor corrosion resistance do not gain the benefit of enhanced corrosion resistance due to electrodeposition surface modification [166].

Figure 3.8 summarises the general requirements for surface modification techniques that should be considered in the surface treatment of mainly metallic materials.

Various surface modification techniques are used for increasing corrosion protection properties of Mg alloys used as biomedical implants. All of these methods are employed to control the corrosion rate of magnesium alloys and enhance the corrosion resistance of these materials. It is of paramount importance to select the most appropriate surface modification treatment based on the intended application of biomaterials. Furthermore, it is essential to consider the solutions applied to the metal surface to alter its properties. For instance, electrodeposition is recommended for producing hydroxyapatite coatings on Mg alloys. Additionally, it has been reported that anodic electrochemical deposition can increase the corrosion resistance of Mg and its alloys in simulated body solutions [109]. However, it is worth noting that costs directly influence the choice of the surface modification method [108].

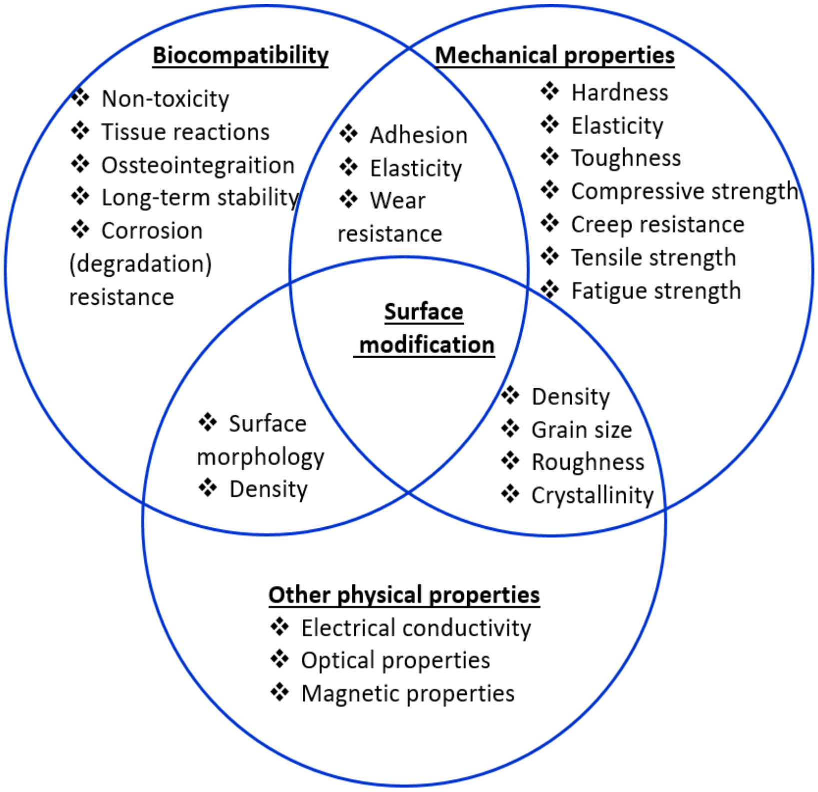

Figure 3.8. General demand of metallic biomaterials obtained through surface modifications [116]

Chapter IV

Surface Modification of Mg alloys by Using Biopolymer Coatings

4.1. Chitosan coatings

In recent years, interest in natural compounds that can be used to modify the surface of metallic materials has increased enormously. Polysaccharides are an important group of natural polymers that are used in medicine, pharmaceuticals, hygiene, oil extraction and other industries due to their attractive properties [167]. Polysaccharides in combination with other chemicals (organic, inorganic) influence, among other things, the biocompatibility of the final product. One of the critical factors for protective polymer coatings used on magnesium alloys in orthopedics is their permeability. Permeability is the ability of a substance to permeate another substance. For coated biodegradable and biocompatible orthopedic implants, permeability is very important. It makes it possible to deliver drugs and substances with antimicrobial effects to the affected tissue. There are widely used natural polymers in tissue engineering such as chitosan, collagen, silk, elastin and gelatine [168] and the synthetic polymers polylactic acid (PLA), polyglycolic acid (PGL), and polycaprolactone (PCL) [125]. There are a few ways to fabricate polymeric coatings on magnesium alloy substrate such as via the spin coater, dip coating, electrospinning and electrophoretic deposition methods [125]. The way of coating application depends on the nature of the polymeric material – natural or synthetic, however, the substrate preparation or pretreatment is the critical factor for the deposition of each type of polymeric coating.

Chitosan is a natural biopolymer, a marine linear cationic polyheterosaccharide [169] composed of repeated units of 2-amino-2-deoxy-D-glucopyranose units and residual 2-acetamido-2-deoxy-D-glucopyranose [170] [171]. Chitosan is the second most proliferated polysaccharide after cellulose [172, 173]. It is named marine polysaccharide because chitosan can be received from mollusk skeletons (crabs and shrimp) rich in chitin. Chitosan is obtained from alkaline hydrolysis (deacetylation) of chitin.

Fig. 4.1. shows the chemical reaction of chitosan production by deacetylation of chitin $(C_8H_{13}O_5N)_n$ [171].

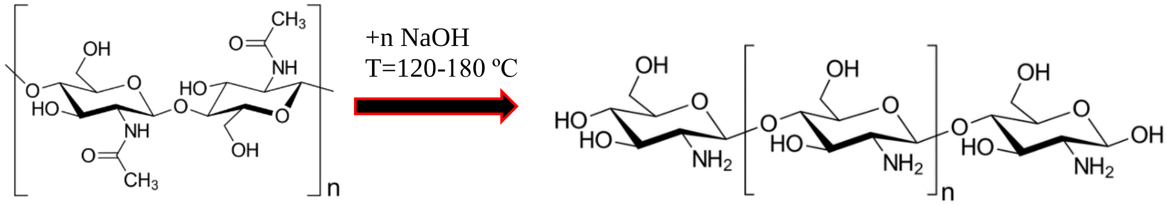

Figure 4.1. Chemical reaction of chitosan production.

This reaction takes place in an alkaline environment in the NaOH solution and at temperatures ranging from 120-180 ºC. Thanks to the presence of functional groups such as primary amine (NH) and primary and secondary hydroxyl groups (OH). Fig.4.1, chitosan can be chemically modified without changing its degree of polymerization [174]. Chitosan has several attractive properties such as biodegradability, biocompatibility, low toxicity, low immunogenicity, the ability to accelerate wound healing and antimicrobial properties [168]. In acidic environments, hydrogen ions attach to the amino groups and chitosan is converted to a cationic form [170]. Due to the natural origin of chitosan, it has found wide application in the food and pharmaceutical industries. Chitosan is also a promising material for biomedical applications, being a good drug carrier [170], and is used to produce protective coatings on magnesium alloys [168]. A summary of the main applications of chitosan and chitin is presented in Table 4.1. The metallic materials are often coated with modified chitosan-based coatings. Depending on the application, various organic (gelatine [171]) and inorganic (TiO_2, ZnO, SiO_2, CaP, ZrO, NaF, and others) compounds can be added to the chitosan matrix. Such modified chitosan coatings can protect the metal covered with them against corrosion, deliver drugs, have antibacterial properties, etc. Thanks to these new properties of chitosan coatings, materials covered with them can find a wider application. Chitosan as a polymer binder in combination with bioactive glass makes it possible to control the rate of dissolution of the magnesium alloy covered with such a coating. Bioactive glass together with chitosan increases the bioactivity of the surface of magnesium alloys. In addition, this type of coating improves the corrosion resistance of metallic materials, especially magnesium alloys, in simulated body solutions [175]. The incorporation of TiO_2 nanoparticles into chitosan coatings improves the antibacterial properties of the polymer coating [169, 176], which is particularly important in the case of orthopedic implants coated with chitosan/TiO_2.

Despite all the advantages of chitosan, it also has a few marked disadvantages. The main one is the slow bone regeneration at the first stages of receiving the chitosan-coated implant. This process can take up to several months. Therefore, it is important to use catalysts that will accelerate the bone growth process, which will improve the effectiveness of chitosan-based materials. It was mentioned earlier that chitosan is a pH-sensitive polymer, and this fact is both an advantage and a disadvantage. Moreover, chitosan-based coatings have low mechanical properties and are not intended for long-term use. This may promote rejection of the implant material or inflammation after implantation [177].

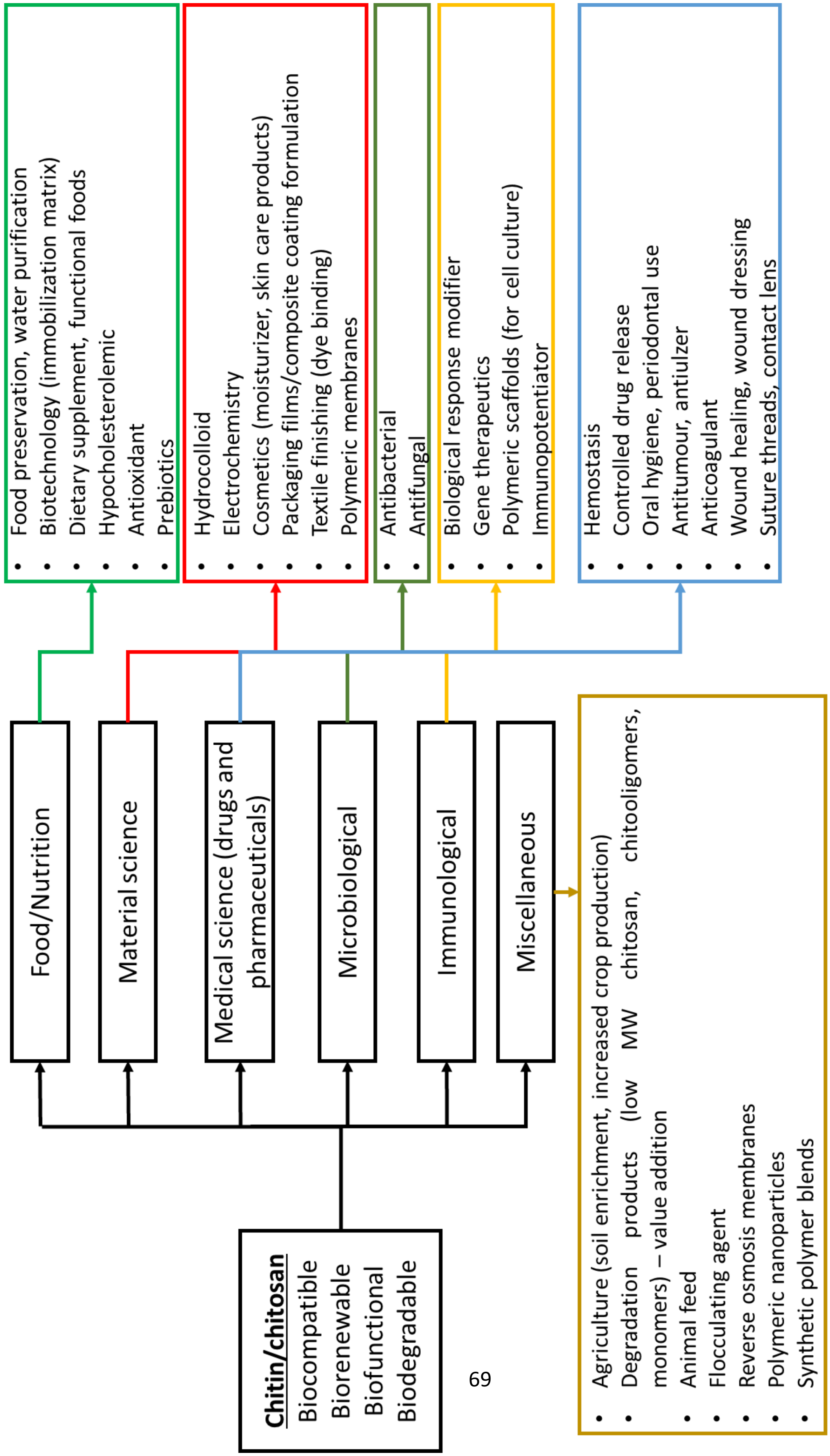

Table 4.1. Applications of chitin and chitosan

4.2. Stearic Acid Modification.

Stearic acid (SA), otherwise known as octadecanoic acid ($CH_3(CH_2)_{16}COOH$, is a saturated fatty acid, which consists of 18 straight-chain carbon atoms. This acid is a component of animal and vegetable fats [178]. Figure 4.2 demonstrates the crystal structure of stearic acid [178]. The melting point of stearic acid is 69.6°C. SA has a polar head group that can react with the metal cations whereas a nonpolar carbon chain determines the solubility of stearic acid in organic solvent [179]. This acid is biocompatible and nontoxic, and is therefore a good compound for the preparation of nontoxic coatings on the metallic material [180]. Stearic acid has found its applications in different branches, in particular in pharmaceuticals or biomedical as a drag delivery component [180], therapeutic aid in soap production, the cosmetics industry and in detergents [179]. SA, as with other fatty acids, can be used as lubricants and softening agents in the rubber industry and applied as surface modifiers [181]. Due to amphiphilic molecules, fatty acids molecules contain hydrophilic and hydrophobic groups which makes them promising surface modifiers within many fields [178].

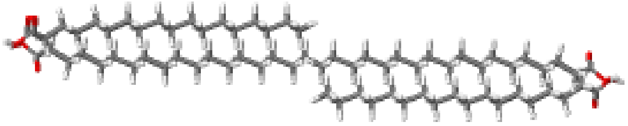

Figure 4.2. Crystal structure of stearic (octadecanoic acid) [178]

The addition of stearic acid to composite materials caused the modification of the microstructure of the composite. Such modification of composite materials has a positive influence on their mechanical, thermal, and electrical properties [181]. Surface modification of magnesium alloys with stearic acid happens by means of immersion in the SA solution and composite coating formation. The protective coating on the surface of magnesium alloy has been formed by two steps. First, the hydrothermal treatment was performed, forming the $Mg(OH)_2$ layer, after which the magnesium alloy was immersed in SA to form an organic coating. Magnesium hydroxide has a porous microstructure, therefore when the Mg alloy was soaked in the solution of SA, the acid molecules diffused through the $Mg(OH)_2$ structure, and the magnesium stearate was formed, reaction 4.1.

$$Mg(OH)_2 + 2CH_3(CH_2)_{16}COOH = [CH_3(CH_2)_{16}COO]_2Mg + H_2O \quad (4.1)$$

This coating exhibited a strong adhesion to the substrate, and it significantly enhanced the corrosion resistance of Mg alloy in the Hank's solution [182]. It has been shown that the composite coating based on stearic acid is superhydrophobic and it improves the corrosion resistance of magnesium substrate [183]. The films of pure stearic acid deposited on the magnesium are mostly very thin, which makes it occasionally difficult to determine its effect on the corrosion resistance of the substrate [183].

4.3. Gelatin coatings.

In recent years, interest in gelatin as a natural polymer has increased which has led to it being widely studied as a coating material for biomedical applications [184]. In addition, gelatin has been used in many industries as a component of multifunctional systems, such as food, pharmaceuticals, cosmetics, photographic films, stabilizing agents, thickeners, film manufacturers and emulsion components [178]. Gelatin is a proteinaceous material [185]. More specifically, it is a high molecular weight polypeptide that is composed of amino acids, mainly glycine (27%), hydroxyproline and proline (25%) [184]. An examination of the structure of the molecule and its strong connection with hydrogen bonds reveals that gelatin films appear fragile. This causes high moisture absorption by gelatin and limits its use in many industries. Fragility is a major disadvantage of using gelatin films, particularly in biomedical applications. In addition, it has poor water resistance and low ductility [184, 185]. Beyond that, the use of gelatin encounters limitations that result from religious conditions and are related to the main method of its production - from pig skin and bovine hides and bones [178].

On the other hand, gelatin has several advantages that make it attractive for biomedical applications, as a component of a bone implant material. These are: biocompatibility and full biodegradability, the fact that gelatin foils are highly transparent and that they do not have a specific smell. Due to the molecular structure of the protein, it is possible to manipulate the gelatin structure to achieve specific material properties [177, 184, 185]. Most often, gelatin films are used in combination with other natural and biocompatible polymers to increase the mechanical properties of these films [177], improve the functional and bioactive properties of the material and they can also be used to improve the structure of the polymer network [144]. For example, proteins such as gelatin are used to improve the stabilization of polysaccharides in water and make them suitable for therapeutic applications [186].

Some researchers have revealed that gelatin can modify the surface properties of metals and slow down their corrosion rate, especially in aggressive solutions. To improve the corrosion resistance of magnesium alloy, the composite coating consisting of MAO film sealed by cross-linked gelatin with distributed PLGA nanoparticles was deposited on WE42 alloy. This coating formed an effective barrier against corrosion, and it effectively improved the corrosion resistance of WE42 alloy in the Hank's solution [187].

4.4. Other Biodegradable Polymers

Previously, natural biopolymers and their applications were described. Synthetic polymers that have similar properties to natural biodegradable polymers can also be used in the human body. Synthetic degradable polymers include aliphatic polyesters such as polylactic acid (PLA), polyglycolic acid (PGA) and polycaprolactone (PCL), which are the most common in biomedical applications [177]. Polyamides and polyesters are types of polymers that have biodegradable and biocompatible properties, are non-toxic and have a variety of combinations of structures.

4.4.1. Polylactic Acid (PLA)

Polylactic acid (PLA) is an attractive polymeric material for biomedical applications and the food packaging industry. PLA and polyglycolic acid (PGA) and their co-polymers found widespread application for tissue engineering [186] and hybridization with collagen [188]. There is a range of advantages that makes PLA interesting for those applications: biocompatibility, high biodegradability, degradation to lactic acid in a biological environment [189] and remarkable mechanical properties [190], inert properties [177] and pH responsibility [170]. One of the main drawbacks of PLA is low crystallinity, which affects the barrier properties of the PLA [189]. To improve the crystallinity of this polymer, surface modification methods are used [189] or, alternatively, the incorporation of different inorganic components [190]. On the other hand, PLA undergoes a rapid degradation in vivo. The implants based on PLA provide different incorrect responses, mainly after 2-4 months to 5 years after implantation. These negative responses are tissue acidification, local inflammation and osteolysis [191]. Compared with other synthetic polymers, PLA has low heat resistance – when the polylactic acid is heated up to 50°C, the polymer loses state shape which causes the limitation in utilization due to reasons such as not being able to be sterilized by heating [191]. Polylactic acid is a polymer with high degradation in biological solutions at around 10-12 days, which is yet another drawback for the application as bone implant material. The degradation products of polylactic acid are lactic acid, which is a metabolite component and can be naturally eliminated from human's body [192]. The degradation process is determined by a range of factors such molecular weight of the polymer, the enantiomeric composition, the characteristics of the implant (size and shape), applications methods and sterilization [177].

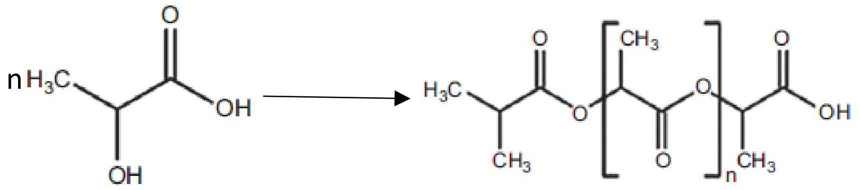

(4.2.)

There are two main enantiomeric forms of polylactic acid - poly-L-lactide (PLLA) and poly-D-lactide (PDLA). These two configurations have opposite structures, due to ring position, achieved by the polymerization process [177]. In terms of molecular configuration, PDLA exhibits poorer mechanical properties, greater susceptibility to weakness, and faster degradation due to its amorphous state [177].

PLA can be employed in the preparation of protective coatings for active metals and their alloys to reduce their corrosion rates. The method of depositing PLA onto the substrate plays a crucial role. Generally, dip-coating results in much higher porosity compared to the spin-coating method. When AZ91 magnesium alloy was coated with PLA using the spin-coating method, it demonstrated a more than two-order-of-magnitude higher polarization resistance than the bare alloy [193]. The polarization resistance gradually decreased with an increase in exposure time to simulated body fluid (SBF).

4.4.2. Polyglycolic Acid (PGA)

Polyglycolic acid (PGA) is the simplest representative of linear aliphatic polyesters, which is produced by polycondensation of glycolic acid [177]. The reaction of polycondensation of glycolic acid is demonstrated on equation 4.3.

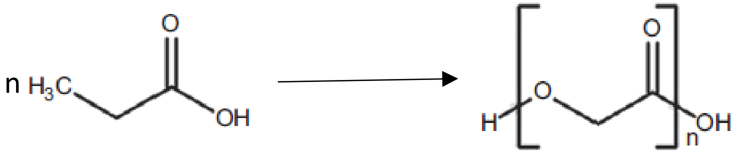

(4.3.)

PGA shows a high melting point (220-225 ºC), high crystalline property (45-55%) with a glass transition temperature of 30-35 ºC and has hydrophobic properties [194]. The crystallinity value is the main factor of its low solubility in organic solvents. During the degradation process, glycolic acid forms. This is a natural participant in metabolism in the human body. PGA was the first polymeric material appropriated for biodegradable structures, but due to low mechanical properties it has limited applications in the biomedical sector [177]. To enhance the mechanical properties of PGA, co-polymeric combinations of PGA and PLA are utilized [191]. Such combinations render the system mechanically stronger [177, 188, 192] when compared to using a single polymeric acid. Conversely, PGA exhibits a high level of biocompatibility, and there have been no reported cases of inflammation associated with materials rich in polyglycolic acid [195]. The most promising applications for this acid include nerve regeneration, wound healing [195], and bone scaffolds [177].

The premier commercially available biodegradable synthetic suture approved by the Food and Drug Academy in the USA was DEXON [194]. That makes it possible to produce implants from polyglycolic acid utilizing a self-reinforcing technique, which is used in treatments of fractures and osteotomies [194]. It has been previously reported that the combination of PGA and PLA shows promising results in biomedical, but other research shows systemic or local reactions in between PLA-PGA scaffolds [196]. PGA, similarly to PLA, is studied as a corrosion inhibitor and correlates with decreasing corrosion rate of implant materials.

4.4.3. Polycaprolactone (PCL)

Polycaprolactone is a biodegradable aliphatic synthetic polyester with a low melting temperature of about 60°C and a glass transition temperature of around -60°C [177, 197, 198]. Polycaprolactone is produced by the polymerization opening of an aliphatic ring of ε-caprolactone in the presence of a catalytic substance (stannous octanoate) combined with increasing temperature [197, 198]. The scheme of the polymerization process is demonstrated in Figure 4.3 [177].

Compared to previous polymers (PLA, PGA), PCL has a much lower degradation rate which makes polycaprolactone more attractive for biomedical applications, especially for long-term implantable drug delivery systems and orthopedic implants [197, 199].

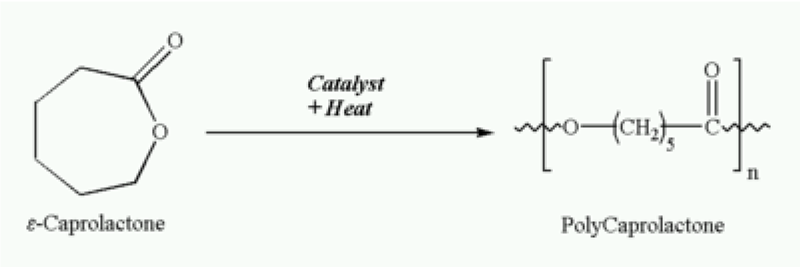

Figure 4.3. Polymerization of ε-caprolactone and polycaprolactone formation [177].

Polycaprolactone is a polymer with a range of advantages needed for biomedical applications such as the fact that the polymer is non-toxic, biocompatible, non-immunogenic, non-cancerogenic and it is a high-level flexibility plastic [177, 198, 199]. Due to the benefits of polycaprolactone it has found widespread use in many industrial branches like food packaging [200] and 3-D printing (for industrial needs) [201]. Moreover, PCL found its range utilization in the biomedical sector: to protect metallic base from corrosion rate, as a polymeric scaffold in 3-D printing to investigate mechanical properties of hydroxyapatite [201], as a coating on Mg alloys to enhance corrosion resistance [202], as a doping material in Mg alloys in drugs industry [203] and also as a scaffold coating before chitosan deposition on a metallic surface [199].

Unfortunately, as with any material, polycaprolactone has its drawbacks which creates limitations in practical use. Polycaprolactone's main drawbacks for biomedical sector applications are its low mechanical strength [200] and its inherent hydrophobic nature which causes complicated interactions with biological fluids [204]. Nevertheless, PCL is a very promising material for combination with other polymeric materials. Moreover, PCL can be utilized with inorganic materials, improving the properties of those materials [177]. It has been studied that a PCL coating deposited on an Mg alloy's surface influences the corrosion resistance of the material and provides suitable cell adhesion and bone formation compared to bare alloy [205]. This means that PCL, like PGA and PLA, act as corrosion inhibitors for implant materials.

Chapter V

Objectives of the dissertation

5. Objectives of the dissertation

Based on the literature review, the following scientific goals for this work were established:

- An examination of the corrosion mechanism and corrosion rates of Mg20Zn and Mg19Zn1Ca alloys in a simulated physiological solution (Hank's solution).
- The production and deposition of chitosan-based composite coatings on magnesium alloys with the aim of significantly reducing the corrosion rates of Mg20Zn and Mg19Zn1Ca alloys in Hank's solution.
- The modification of the chitosan coating to impart antibacterial properties.

The literature review did not provide a clear direction for determining the optimal structure of chitosan coatings to significantly reduce the release of hydrogen and the corrosion rate of binary and ternary magnesium alloys. However, analysis of the literature reports allowed the formulation of the following thesis for this work:

Hybrid inorganic/organic coatings should significantly slow the corrosion rate of magnesium alloys in simulated physiological solutions. The chemical interaction between inorganic compounds and chitosan particles may have a beneficial effect on slowing down the corrosion rate of magnesium alloys.

Chapter VI

Materials and experimental methods

6.1. Materials and surface preparation

Magnesium alloys Mg20Zn and Mg19Zn1Ca have been used as substrates for the deposition of chitosan-based coatings. These alloys were delivered by Goodfellow. The chemical composition of magnesium alloys is: 20 wt.% Zn and 80 wt.% Mg for Mg20Zn and 1wt.% Ca, 19 wt. % Zn and 80 wt.% Mg for Mg19Zn1Ca, respectively. Specimens of 8 mm thickness were cut from rods (diameter 10 mm, length 10 cm). They were ground with emery paper (1200 grit), cleaned by sonication for 60 seconds in ethanol, rinsed with ethanol, and then dried with argon. The specimens used for corrosion tests were embedded in an epoxy resin. The electrical contact to the lateral face of the rods was made using an insulating cable. The surface area in contact with the electrolyte was 0.785 cm^2. In Fig.6.1, the top view of the Mg20Zn specimen mounted in the epoxy resin is shown.

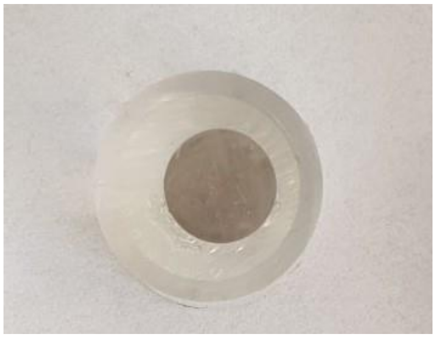

Figure. 6.1. Top view of mounted Mg20Zn alloy sample in epoxy resin.

The specimens that were used for the investigation of the microstructure were ground with emery paper up to 4000 grits, then smooth (polished) by using the SiO_2 colloidal suspension. Then, the specimens were cleaned by sonication for 5 minutes in ethanol, rinsed with ethanol, and dried with argon. Such preparation of the surface of Mg alloys allows, to reveal the microstructure, and the surface observation could be performed by using the scanning electrochemical microscope (SEM).

6.2. Coating's preparation and deposition on the substrate

In this study, it has been investigated two main types of coatings – inorganic (phosphate coating) and organic (chitosan based coating).

1) The first coating studied (noted "**Ca-P coating**") was chemically formed by immersing the substrate at the open circuit potential (OCP) in a solution containing 70 ml H_2O, 30 ml C_2H_5OH, 2 g $Ca(NO_3)_2 \cdot 2H_2O$ and 0.7 g NaH_2PO_4 for 12 hours. The solution was stirred at 250 rpm.

2) The second coating (noted "**chitosan**") was a chitosan coating deposited in a solution containing 2 g of chitosan (Acros Organics, molecular mass 100000-300000) dissolved in 100 ml of 1 vol.% acetic acid solution. To completely dissolve chitosan, the solution was stirred for 24 hours at room temperature. When chitosan solution has been prepared – different inorganic particles were added to improve the functional properties of the coatings.

3) The third coating (noted **"chitosan/TiO_2**) the chitosan solution containing the nanoparticles of titanium dioxide TiO_2 has been prepared in the following procedure. The first two solutions were prepared, solution (S1) 2g of chitosan powder was dissolved in the 100ml of 1vol.% of acetic acid. This solution was stirred at 250 rpm for 24 hours. The second solution (S2) of 0.5 g of TiO_2 nanoparticle (average size 20 nm) was dissolved in 50 ml of 1% vol. of acetic acid. Then, 50 ml of solution (S1) was mixed with 50 ml of solution (S2). This mixed solution (chitosan/TiO_2) was used for the deposition of coatings on the substrates (Mg20Zn or Mg19Zn1Ca alloys).

4) The coating (noted by **"chitosan_WG coating**") was a chitosan-based coating deposited in a solution containing 50 mL of solution (S1), 0.5 g Na_2SiO_3 and 1 mL of water glass (Chempur, SiO_2/Na_2O molar modulus 2.4–2.6). Solution (S1) contains 2 g of chitosan (Acros Organics, molecular mass 100 kDa–300 kDa) dissolved in 100 mL of 1 vol.% acetic acid solution. To completely dissolve chitosan, S1 was stirred for 1 h at a temperature of 40°C.

All chitosan-based coatings were deposited on the substrate (Mg20Zn, Mg19Zn1Ca) by means of the spin coater POLOS SPIN 150i. The procedure used for the deposition of chitosan-based coatings consists of four steps (step 1 for 5 seconds at 250 rpm, step 2 for 30 seconds at 1000 seconds, step 3 for 60 seconds at 1500 rpm, and step 4 for 60 seconds at 250 rpm). This procedure was repeated 6 times, resulting in a coating comprising six polymer sublayers.

6.3. Techniques used for characterization of substrate and coatings

To study the corrosion behavior of coated and uncoated specimens' different experimental techniques must be used. In this thesis, the microstructure of the substrate and coatings has been investigated by using microscopic, diffraction, and spectroscopic techniques. The choice of test technique depends on the type of material to be tested and the scale at which the measurement will be made (macro, micro, or nanoscale). In Fig. 6.2 different techniques are presented that can be used for the characterization of materials within various scales.

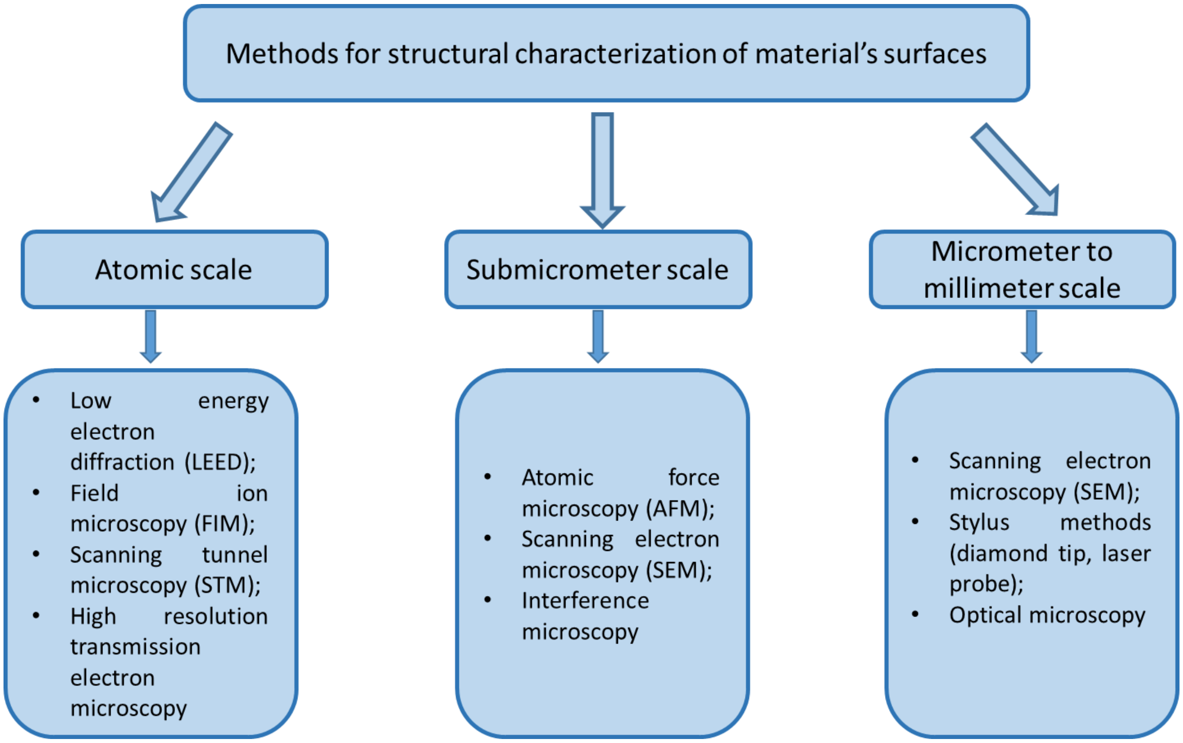

Figure 6.2. Methods for structural characterization of Mg alloys surfaces has been applied in this work.

In this thesis, the following experimental techniques were used for the characterization of substrate and coatings: scanning electron microscopy, X-ray diffraction spectroscopy, optical profilometry, Fourier-transform infrared spectroscopy (FTIR), and X-ray electron spectroscopy (XPS). Microstructural observations and chemical composition analysis were performed by Field-Emission Scanning Electron Microscope (FE-SEM) with Energy Dispersive X-ray Spectroscopy (EDS) integrated detector, which is a widely used technique in research on surface morphology and structural research of materials. EDS allows obtaining the quantitative microanalysis of the sample. In the case of EDS analysis, the content of elements is determined by the proportional relationship of the number of emitted characteristic pulses of X-ray radiation to the concentration of elements in the tested place. The depth of signal excitation is related to the depth of penetration of the electron beam into the material under test and depends on the type of material and the energy of the primary electron beam. The quantitative interpretation of EDS analysis should be interpreted carefully, especially for light elements such as carbon, and oxygen. The main disadvantage of the SEM technique is that the measurement must be carried out in a vacuum. Pumping out the air from the chamber may influence the behavior of the tested material. Some materials may also be sensitive to beam bombardment resulting in forming artefacts during the measurement. Top-view surface imaging of uncoated and coated specimens was carried out with SEM (JEOL, JSM-5500LV). An acceleration voltage of 20 kV was used. The microstructure of the magnesium alloys was investigated by means of X-ray diffraction. Intermetallic phases present in the Mg20Zn alloy as well as in the Mg19Zn1Ca alloy were identified by XRD with Philips PW-3710 X'PERT diffractometer using Cu-Ka radiation.

Optical profilometry is a contactless technique that is usually used to assess surface roughness, and surface changes that are the result of, for example, corrosion degradation, and coatings deposition [115]. The thickness of deposited coatings can be measured by means of this technique. In this thesis, optical profilometry was used for the determination of the roughness of the chitosan-based coatings.

The surface of the coated specimens before and after the corrosion tests have been investigated by means of X-ray Photoelectron Spectroscopy and Fourier-transform infrared spectroscopy (FTIR). X-ray photoelectron spectroscopy (XPS) is a spectroscopic technique based on the photoelectric effect. This technique allows us to identify the elements that exist at the surface of material or coating, as well as their chemical state. Chemical states are inferred from the measurement of the kinetic energy and the number of ejected electrons from the surface. The electron binding energy of the emitted electrons can be determined by using the photoelectric effect equation (6.1).

$$E_B = E_{photon} - E_{kin} + \phi \qquad (6.1)$$

where E_B is the binding energy of the electron measured relative to the chemical potential, E_{photon} is the energy of the X-ray photons being used for the experiment, E_{kin} is the kinetic energy of the electron ejected from the surface of the material and measured by the instrument, and ϕ is a work function. XPS can be used in line profiling of the elemental composition across the surface. Moreover, depth profiling can be obtained when the ion-beam etching (Ar^+ ions) of the surface is performed. XPS detects all chemical elements except hydrogen and helium. In this thesis, XPS analysis was performed after the deposition of chitosan-based coatings and after immersion of these coatings in the Hank's solution for 110 hours and 4 days. The equipment is a SIA 100

Cameca Riber apparatus and a nonmonochromated Al Ka line (energy of 1486.7 eV, power of 50Wand X-ray beam diameter of 200 nm). A Mac 2 semi-imaging spectrometer was used with a resolution of 1.3 eV (width of Ag 3d5/2 level). C(1s) peak from pollution (285 eV) was considered for the energy calibration. During XPS measurements, the residual pressure of the analysis chamber was maintained below 10-7 Pa. Spectra were treated with the Casa software package, and ionization cross-sections from Landau were used in order to quantify the semi-empirical relative sensitivity factors.

Fourier Transform Infrared Spectroscopy (FTIR) is an analytical methodology used to study the structure of individual molecules and the composition of molecular mixtures. FTIR spectroscopy uses modulated energy in the mid-infrared to study samples. Infrared light is absorbed at specific frequencies directly related to the vibrational energies of the bonds between atoms in a molecule. When the vibrational bond energy and the mid-infrared light energy are equal, the bond can absorb this energy. Different bonds in a molecule vibrate with different energies and therefore absorb different wavelengths of infrared radiation. The position (frequency) and intensity of these individual absorption bands make up the overall spectrum. FTIR analysis is used in industrial (pharmaceutical, chemical, and polymer industries) and academic laboratories to study the molecular structure of materials. In this thesis, FTIR analysis was used to study the molecular structure of chitosan-based coatings by using a Thermo-Scientific Nicolet 6700 spectrophotometer equipped with an attenuated total reflectance accessory (ATR) accessory. FTIR spectra were obtained over a scan range of 4000 cm^{-1} to 500 cm^{-1}.

6.4. Electrochemical techniques and corrosion tests

Corrosion tests were carried out on uncoated and coated Mg19Zn1Ca substrates in the Hank’s solution. The chemical composition of the Hank’s solution is: 8 g/l NaCl, 0.4 g/l KCl, 0.140 g/l $CaCl_2$, 0.350 g/l $NaHCO_3$, 0.217 g/l NaH_2PO_4, 0.06 g/l Na_2HPO_4, 0.406 g/l $MgCl_2•6H_2O$, 0.029 g/l $MgSO_4$, 1 g/l D-glucose. Corrosion measurements were performed using a standard three-electrode cell. The reference electrode is an Ag / AgCl (3M KCl) reference electrode, and the counter electrode is a Pt grid (4 x 5 cm2). All the experiments were performed with a Metrohm Autolab PGSTAT128 Potentiostat/Galvanostat and Nova 2.1 software.

6.4.1. Electrochemical techniques

To determine the corrosion resistance the linear sweep voltammetry (LSV) has been performed. In this technique, a linearly varying potential is applied to the working electrode and then a current is measured. From LSV curves the following parameters can be determined: corrosion potential, corrosion current, limiting current, passive current, breakdown potential, and pitting potential. Moreover, the position of the anodic oxidation peak, passive and transpassive regions. The corrosion potential and the corrosion current can be obtained from the extrapolation of the Tafel plot. Knowing the corrosion current, the corrosion rate of metal can be calculated by using the equation (6.2).

$$v_{corr} = \frac{i_{corr}}{nFA} \tag{6.2}$$

where n is the number of electrons exchanged, F is Faraday's constant, A is the surface area of the corroding electrode, i_{corr} is the corrosion current. Before the LSV experiment, the open circuit potential (OCP) was measured. The open circuit potential (OCP) is the potential set up spontaneously by an electrode in the absence of an external current. OCP is the potential established between the working electrode and the environment, with respect to a reference electrode. The reference electrode is placed in the electrolyte close to the working electrode. Measurement of the OCP is also a nondestructive method that allows you to estimate the tendency of a metal to corrode. Therefore, checking up on the OCP helps keep an eye on corrosion processes. More positive open circuit potential seems beneficial because the system would much rather take electrons in than lose electrons, so it is more likely that reduction reactions occur.

To check where the corrosion starts at the surface of bare magnesium alloys the chronoamperometry test has been performed. After this test, the surface observation of the specimens was performed by using scanning electron microscopy (SEM). Chronoamperometry is an electrochemical technique in which the electrical potential is imposed on the working electrode and the resulting current from the electrode is monitored as a function of time. There are two types of chronoamperometry that are commonly used: controlled-potential chronoamperometry and controlled-current chronoamperometry. The relationship between current response and time can be measured after applying a single or double potential step to the working electrode. Before chronoamperometry controlled-potential chronoamperometry, cyclic voltammetry (CV) or linear sweep voltammetry (LSV) are run to determine the potential of oxidation or reduction. Generally, chronoamperometry is suitable for studying electrode processes.

One of the parameters, that characterize the corrosion resistance of a material is its polarization resistance. The polarization resistance (R_p) corresponds to the corrosion resistance of the specimen and is obtained by the linear polarization resistance method. The polarization resistance is defined as the resistance of the specimen to oxidation during the application of an external potential. The current density linearly depends on the potential in a narrow potential region of E_{corr} ± 20 mV, as expressed by equation (6.3).

$$R_p = \left(\frac{\Delta E}{\Delta i}\right)_{E_{corr}} \tag{6.3}$$

Electrochemical impedance spectroscopy (EIS) is a well-known technique for the determination of the corrosion resistance of uncoated and coated metallic materials. In this, the current is measured as a response of an electrode to a sinusoidal potential perturbation of small amplitude (typically 5-10 mV) at different frequencies. The EIS measurements can be performed at imposed on the specimen either onto an applied anodic, cathodic or OCP potentials. Another possibility is to modulate the current and to measure the potential. Among the different transient methods, EIS is most widely used in corrosion studies. It serves for the measurement of uniform corrosion rates, for the elucidation of reaction mechanisms, for the characterization of surface films and for testing of coatings [93].

In this thesis, the corrosion measurements were performed by using three-electrode cells. The following electrodes were used: reference electrode Ag / AgCl (3M KCl), the counter electrode was a Pt grid (4 x 5 cm^2) and the specimen was used as a working electrode. All the measurements were performed with a Metrohm Autolab PGSTAT128 Potentiostat/Galvanostat and Nova 2.1 software. Linear sweep voltammetry (LSV) curves were plotted from -50 mV vs. OCP to the anodic direction, at a potential scan rate of 1 mV s^{-1}. Prior to LSV experiments, the open circuit potential (OCP) was measured for 30 minutes (to reach the steady state). The chronoamperometry test has been performed for bare Mg20Zn and Mg19Zn1Ca alloys at the potential value −1.25 V vs. Ag/AgCl (3M KCl). These tests were performed for 120 seconds in the Hank's solution, and then the surface observation of the Mg alloys was performed. Linear polarization measurements (LPR) were performed after 30 minutes of immersion of uncoated and coated specimens in the Hank's solution. Then, the specimens were polarized at ±25 mV vs. OCP with a potential scan rate of 0.125 mV/s. Electrochemical Impedance Spectroscopy (EIS) measurements were performed potentiostatically in Hank's solution at the open circuit potential (OCP). A sinusoidal AC wave of ±30 mV amplitude was applied from 10 kHz to 0.008 Hz. Fitting of the experimental spectra was carried out using the ZView software (Scribner Associates).

6.4.2. Determination of corrosion rate of uncoated and coated magnesium alloys from the hydrogen evolution test.

During the corrosion process of Mg and its alloys, the hydrogen gas is released in different aqueous environments [206]. Figure 6.3 shows the hydrogen evolution experimental setup for the collection of hydrogen released during the corrosion tests. The amount of hydrogen gas released during the corrosion test was measured using a burette placed above the specimen, according to the method described in [207].

The corrosion rate of uncoated and coated alloys was calculated based on measurements of hydrogen volume evolved during the corrosion test. The specimens were immersed in the Hank's solution for 4 or 7 days at 37 °C, pH=7.2.

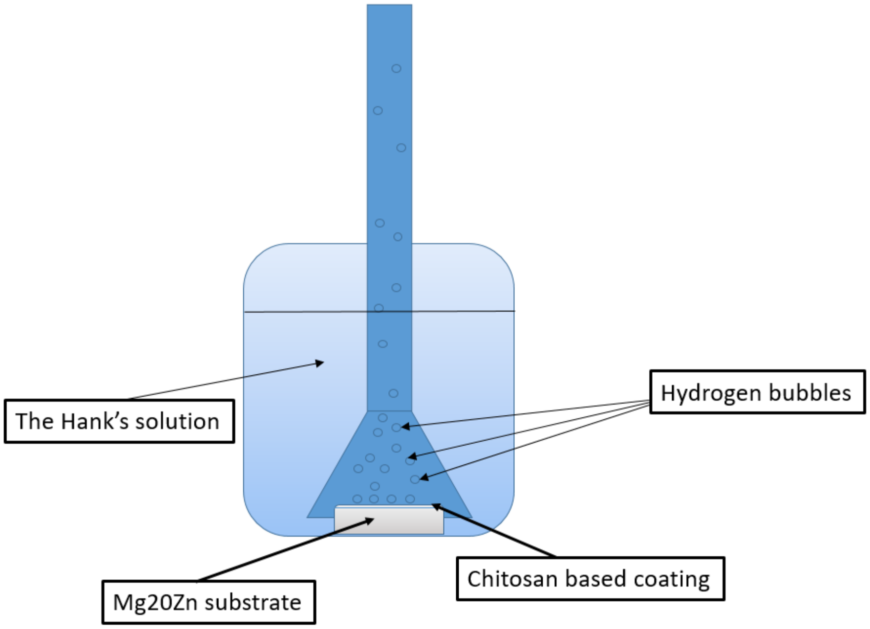

Figure 6.3. The diagram of the experimental set-up used for the hydrogen evolution test.

The overall corrosion reaction of magnesium in aqueous solutions can be expressed by reaction (6.4):

$$Mg + 2H_2O = Mg^{2+} + 2OH^- + H_2 \qquad (6.4)$$

The corrosion rate of magnesium and its alloys can be calculated from equation (6.5).

$$v = 87.6\left(\frac{m\,[mg]}{d\left[\frac{g}{cm^3}\right]\cdot s\,[cm^2]\cdot t\,[h]}\right)[mm/y] \qquad (6.5)$$

Where d is the density of the metal, s – is the surface of metal exposed to the corrosive environment, t –time of exposed specimen in the Hank's solution, m- mass of magnesium dissolved during the corrosion test. According to the stoichiometry of the reaction (6.4), the evolution of 1 mole of hydrogen gas corresponds to the dissolution of one mole of magnesium. Therefore, the corrosion rate of magnesium alloy can be calculated on the base of the reaction (6.4), knowing the volume of the hydrogen evolved during the corrosion process.

6.5. Antibacterial tests

The antibacterial properties of solution coatings have been investigated through the disc diffusion method and the serial dilution method. The solution of the following coatings have been investigated: chitosan, chitosan/WG, chitosan/TiO_2, chitosan/Ag (NPs) and chitosan/ZnO (NPs). The preparation of chitosan, chitosan/TiO_2, and chitosan/WG coatings was described in paragraph 6.2. The chitosan coatings containing the silver and zinc oxide nanoparticles were prepared according to the following procedures:

1) Chitosan/Ag coating was prepared by mixing the 20 ml of 2% wt—chitosan solution with 11 ml of colloidal suspension containing the silver nanoparticles (NPs). One ml of colloidal suspension contains 0.0026 g of silver. The concentration of silver nanoparticles in the chitosan solution was 922µg/ml.
2) Chitosan/ZnO coating was obtained by mixing 20 ml 2% wt—chitosan solution with 17 ml of ZnO colloidal suspension. One ml of ZnO suspension contains 0.0414 g of ZnO. Therefore, the concentration of ZnO nanoparticles in the chitosan solution was 19 mg ZnO/ml.

The ZnO (NPs) and Ag (NPs) used for the preparation of chitosan-based coating have been synthesized in an electrochemical way according to the procedures described in the references [208, 209]. The crystalline silver nanoparticles were formed by potentiostatic polarisation of silver electrode in the saturated solution of $NaNO_3$ in ethanol solution deaerated by argon. The polarization has been performed at 0.4 V vs. Ag/AgCl electrode for 4 hours. However, the ZnO nanoparticles were formed during the polarization of the zinc electrode at 0.4 V vs. Ag/AgCl electrode for 4 hours in 0.1M LiCl – C_2H_5OH +5% H_2O solution.

The antibacterial properties of the solution coatings have been investigated against two of the most popular bacteria Staphylococcus Aureus (S. A) and Escherichia Coli (E. C). The two methods were performed to study the resistance of chitosan-based coatings against the bacteria – disk diffusion and dilution method. A description of how the antibacterial tests were performed and the results are presented in chapter IX.

Microstructure of Mg20Zn, Mg19Zn1Ca alloys and chitosan-based coatings

7.1. Microstructure of magnesium alloys (Mg20Zn, Mg19Zn1Ca)

The microstructure of binary Mg20Zn and ternary Mg19Zn1Ca alloys has been investigated using the scanning electron microscopy (SEM) and X-ray diffraction (XRD) techniques. In Fig. 7.1. the microstructure of Mg20Zn and Mg19Zn1Ca alloys have been revealed following mechanical grinding with emery paper (2400 grit) and polishing via SiO_2 suspension. Mg20Zn alloy consists of two phases (Figure 7 (a, b)), namely α-Mg hexagonal phase (matrix) and $Mg_{51}Zn_{20}$ intermetallic phase. The intermetallic phase is located at the grain boundaries.

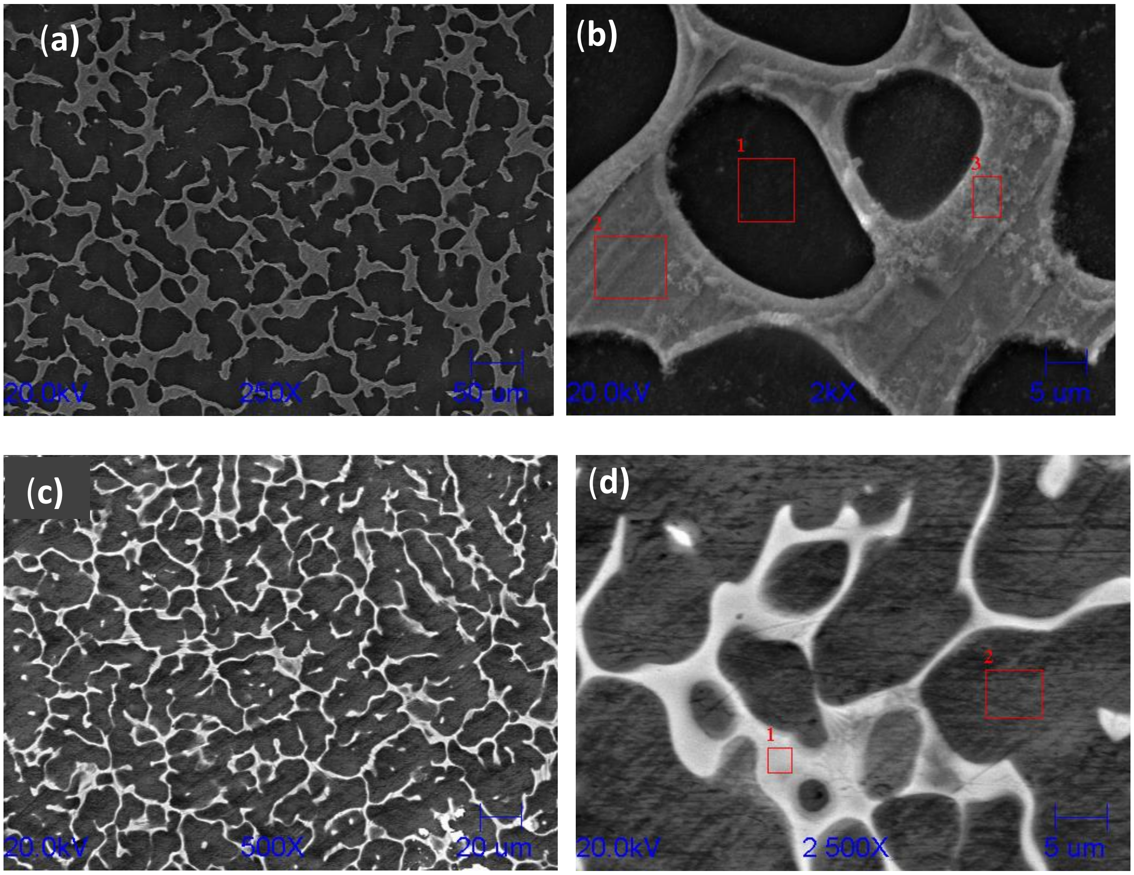

Figure 7.1. Microstructure of Mg20Zn alloy (a, b) [210], and microstructure of Mg19Zn1Ca alloy (c, d) [211].

EDS analysis was performed in sites containing the pure matrix (site 1 in Figure 7 (b)) and the intermetallic phase (sites 2 and 3 in Figure 7 (b)). The matrix is composed mainly of magnesium and a small amount of zinc. The intermetallic phase contains mainly magnesium, and a much higher amount of zinc compared to its content in the matrix. The surface of the Mg20Zn alloy was slightly oxidized, and few at. % of oxygen was detected. Figure 7.2 shows EDS spectra that were taken during the analysis of the chemical composition of the Mg 20 Zn alloy in places 1 and 2 marked in Figure 7.1 (b).

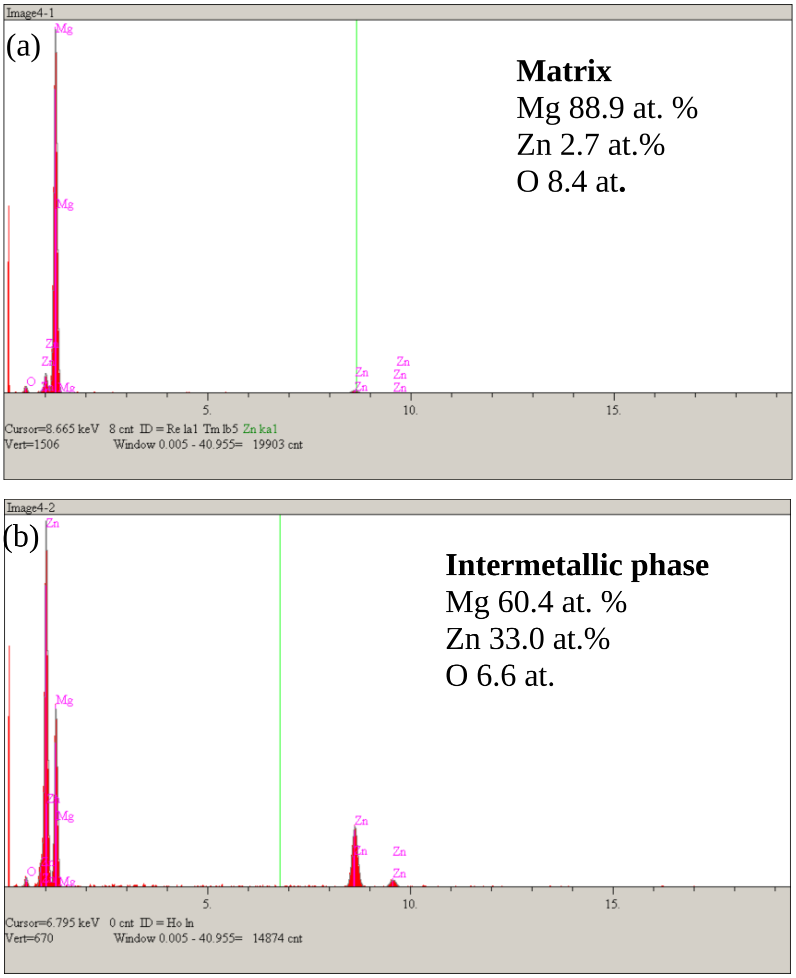

Figure 7.2. EDS spectra measured for matrix (a) and intermetallic phase (b).

Fig. 7 (c, d) shows the microstructure of the Mg19Zn1Ca alloy. The intermetallic phases are located along the grain boundaries. EDS analysis has revealed that the matrix (site 2, Figure 7 (d)) is composed of magnesium (98.0 ± 0.7 at. %) with a small amount of zinc (2.0 ± 0.2 at. %). The intermetallic phase (site 1, Figure 7 (d)) is composed of magnesium (61.0 ± 3.0 at. %), zinc (35.0 ± 4.0 at. %) and calcium (3.8 ± 1.0 at. %). The presence of intermetallic phases was confirmed by X-ray diffraction measurements (XRD) in Figure 7.3. From the XRD peaks, the crystalline nature of the substrate is observed. In the case of Mg20Zn alloy, the XRD measurements have confirmed the presence of two phases: α-Mg hexagonal (matrix) and intermetallic $Mg_{51}Zn_{20}$, Fig. 7.3 (a). For the Mg19Zn1Ca alloy, however, three phases were detected: α-Mg hexagonal (matrix) and the Mg_2Ca and $Ca_2Mg_6Zn_3$ intermetallic phases, Fig. 7.3 (b) (b). The highest peak formed at 2-Theta (deg) angle of 36.5 is related with α-Mg hexagonal close packed crystal structure [212, 213].

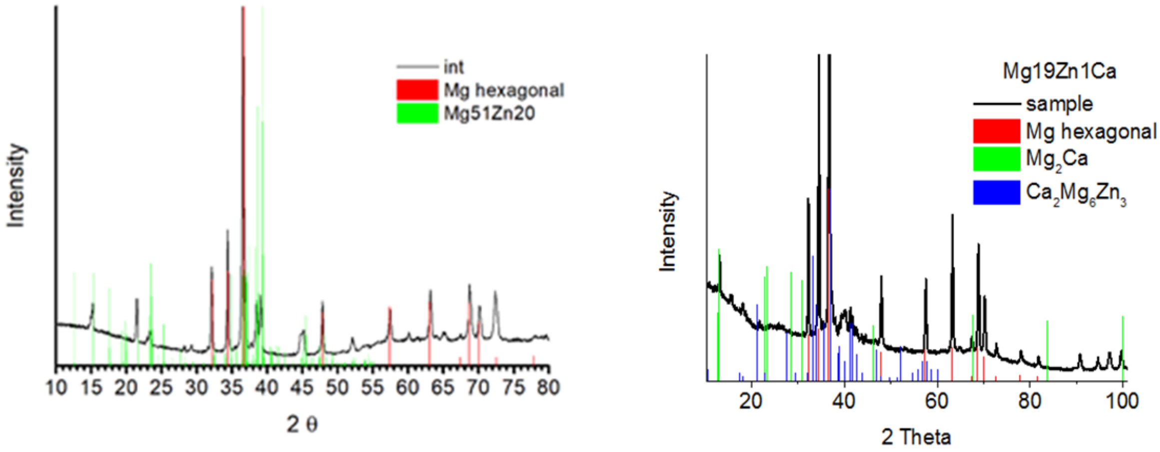

Figure 7.3. XRD diffraction pattern of Mg20Zn (a) [210] and Mg19Zn1Ca (b) [211]

7.2. Structure of Ca-P and chitosan-based coatings.

The corrosion resistance of magnesium alloys was improved by applying an inorganic calcium-phosphate coating and chitosan-based coatings to their surface. Figure 7.4 presents the top view of the calcium-phosphate and chitosan coatings containing water glass. The Ca-P coating shows a rough surface with a crystalline structure (Figure 7.4 (a, b)). At high magnification, a plate-like structure is visible, Figure 7.4 (b). Plates are mainly composed of calcium (64.6 at.% in site 1, Figure 7.4 (b) and phosphorous (25.2 at.%, site 1) with a small amount of oxygen (6.7 at.%, site 1).

The surface of the Ca-P/chitosan_WG coating appears smooth and compact, although some rare microcracks can be observed (Figure 7.4 (c, d)). EDS analyses at low magnification (site 2 in Figure 7.4(c)) yield 35.3 at.% carbon, 45 at.% oxygen, 5.6 at.% silicon, and 2.3 at.% sodium (these elements come from the outer chitosan_WG sublayer), 6.1 at.% calcium and 5.4 at.% phosphorous. By contrast, the surface of the chitosan_WG coating deposited on the pure Mg20Zn alloy appears smooth, but numerous microcracks are observed, Figure 7.4 (e, f). EDS analysis performed on the surface of this coating (site 3 in Figure 7.4(e)) yields 55 at.% carbon, 37 at.% oxygen and 8 at.% silicon.

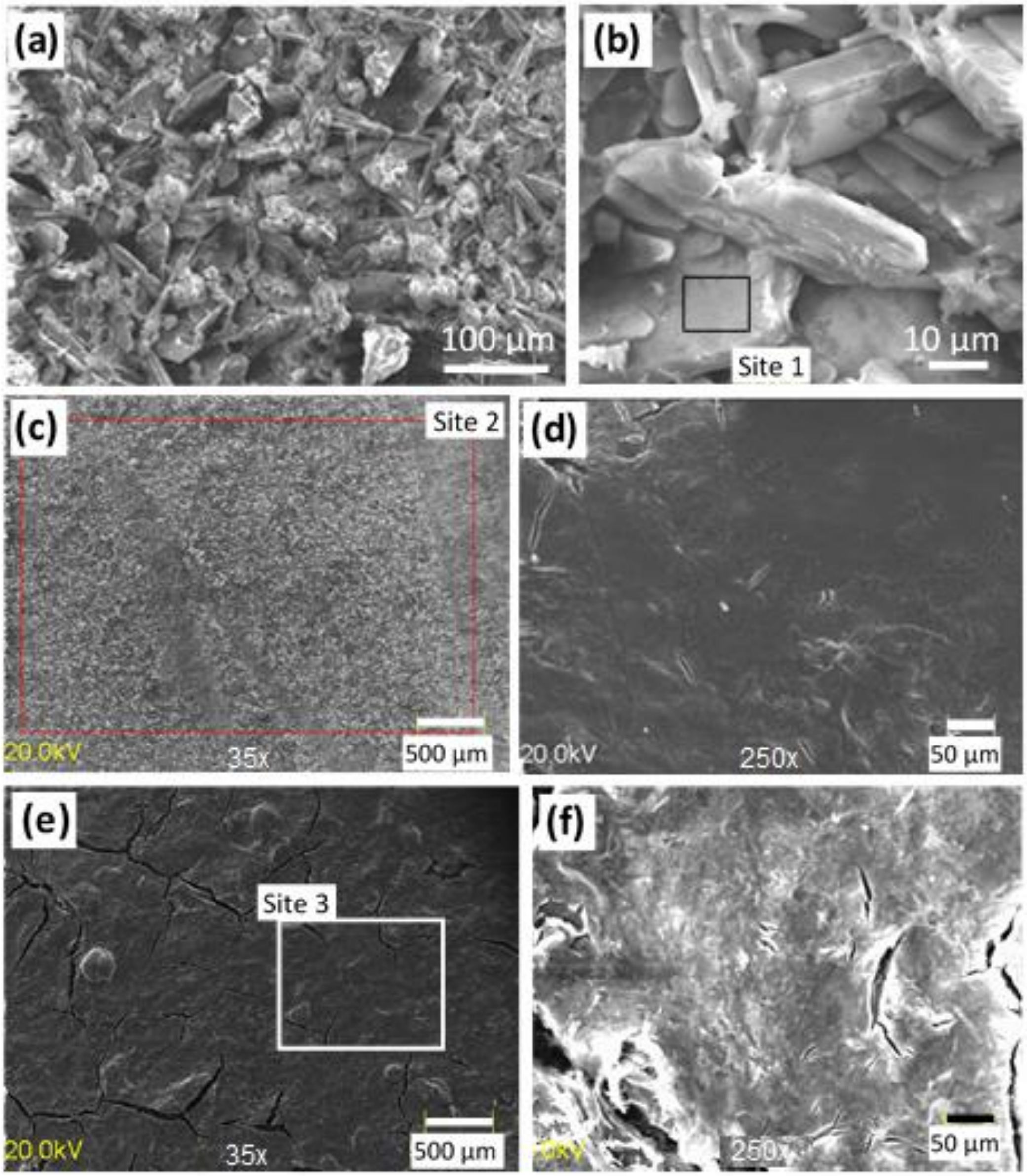

Figure 7.4. SEM images of (a, b) Ca-P (c, d) Ca-P/chitosan_WG and (e, f) chitosan_WG coatings deposited on the Mg20Zn alloy [210].

The morphology of the chitosan/TiO_2 coating has been investigated by using a Scanning Electron Microscope (SEM). Figure 7.5 (a) shows the cross-section through the substrate coated with the chitosan/TiO_2 coating. The coating is uniformly deposited on the substrate without the defects at a thickness of about 10 µm. The top view of the chitosan/TiO_2 coating deposited on the substrate is shown in Figure 7.5 (b, c). The TiO_2 nanoparticles (white area) are uniformly distributed in the chitosan matrix. Distribution of the elements like carbon, nitrogen, oxygen, titanium, and magnesium on the surface coating is presented in Figure 7.5 (d – h). It can be noticed that in places where the TiO_2 nanoparticles are located, mainly titanium and nitrogen are present, Figure 7.5 (e, g). The oxygen is uniformly distributed in the coating, Figure 7.5 (f). The carbon and magnesium are located around the TiO_2 nanoparticles, Figure 7.5 (d, h). The presence of higher amounts of nitrogen in places where the titanium nanoparticles are found suggests the interaction of the N-H group form chitosan molecule with titanium dioxide. Titanium has not completely filled with electrons the atomic orbital d, therefore it can be an acceptor of a lone pair of electrons from an atom of another element. The nitrogen atom has a lone pair of electrons and can give it to another atom. It has been revealed that the formation of $TiO_2\_N_x$ nanoparticles can be obtained at room temperature by direct amination of TiO_2 nanoparticles [214].

Figure 7.6 shows the corss section of chitosan_WG (a) and chitosan/TiO_2 (b) coatings deposited on magnesium alloys. The thickness of the chitosan_WG coating is approximately 40 μm, and the thickness of the chitosan/TiO_2 was measured in the range between 10 μm and 14 μm. It should be emphasized that the thickness of the chitosan-based coating does not depend on the substrate. The same coating thickness was measured for both substrates (MgZn and MgZnCa). The thickness of the chitosan WG coating was measured using Glow discharge optical emission spectroscopy (GDOES). GDOES is an analytical technique that can quickly measure both the surface/depth profile and the elemental composition of solid materials and layers with high sensitivity. Figure 7.7 shows the surface/depth profile of the chitosan_WG coating deposited on the Mg20Zn alloy. The lowest values of carbon, hydrogen, nitrogen and silicon content were measured at a depth of approximately 40 μm. A sharp increase in magnesium and zinc content was observed at the same depth, however. Elements such as magnesium and zinc are found only in the substrate. Therefore, GDOES measurements confirmed that the chitosan_WG coating thickness is 40 μm. In Figure 7.8., the cross section of Ca-P/chitosan_WG coating is shown. EDS spectra were performed in the selected regions marked in Figure 7.8. Figure 7.9 shows the EDS spectra and chemical composition of selected areas. The presence of chromium is related to the deposition of a thin chromium layer to enhance the electrical conductivity of the investigated chitosan coating. The Ca-P coating contains calcium, phosphorus and oxygen, Figure 7.9 (a). The main elements present in the chitosan_WG coating are carbon, nitrogen, oxygen and silicon, Figure 7.9 (b).

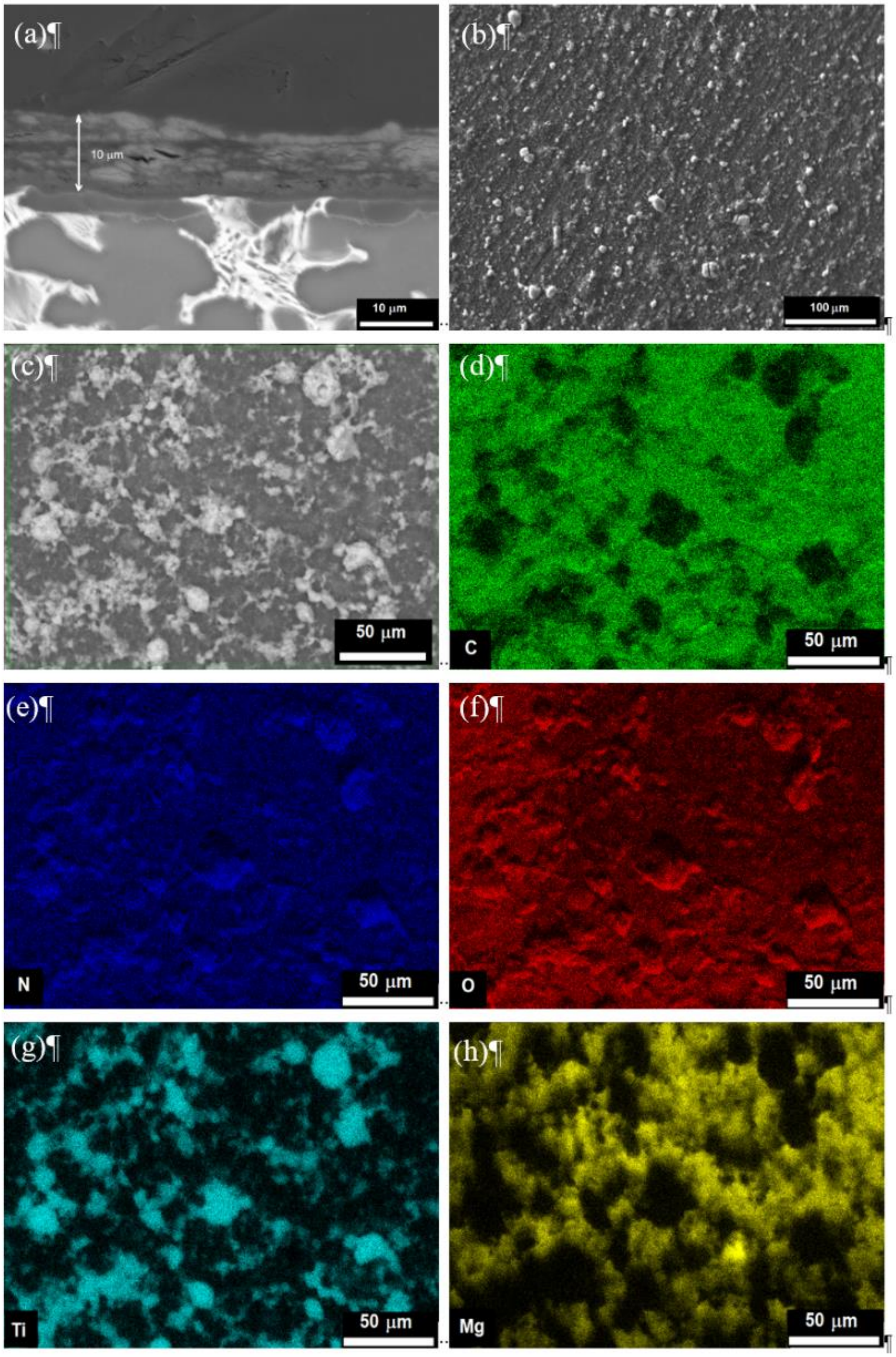

Figure. 7.5. SEM images of the TiO_2 coating deposited on the Mg19Zn1Ca substarte (a) top view, (b) cross section, (c-f) mapping of the elements present in the coating [211].

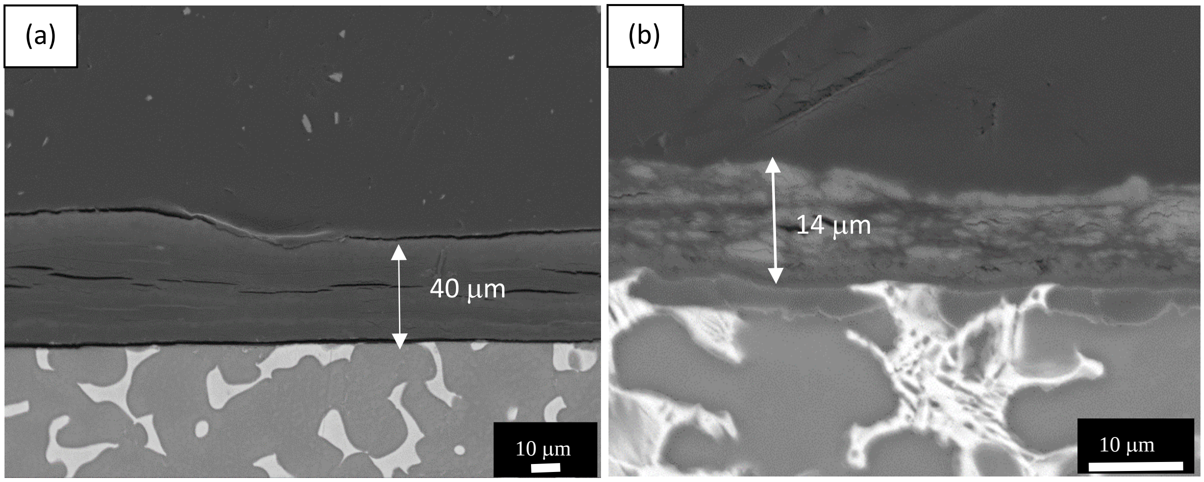

Figure 7.6. The cross section of chitosan_WG (a) and chitosan/TiO_2 (b) coatings deposited on magnesium alloys.

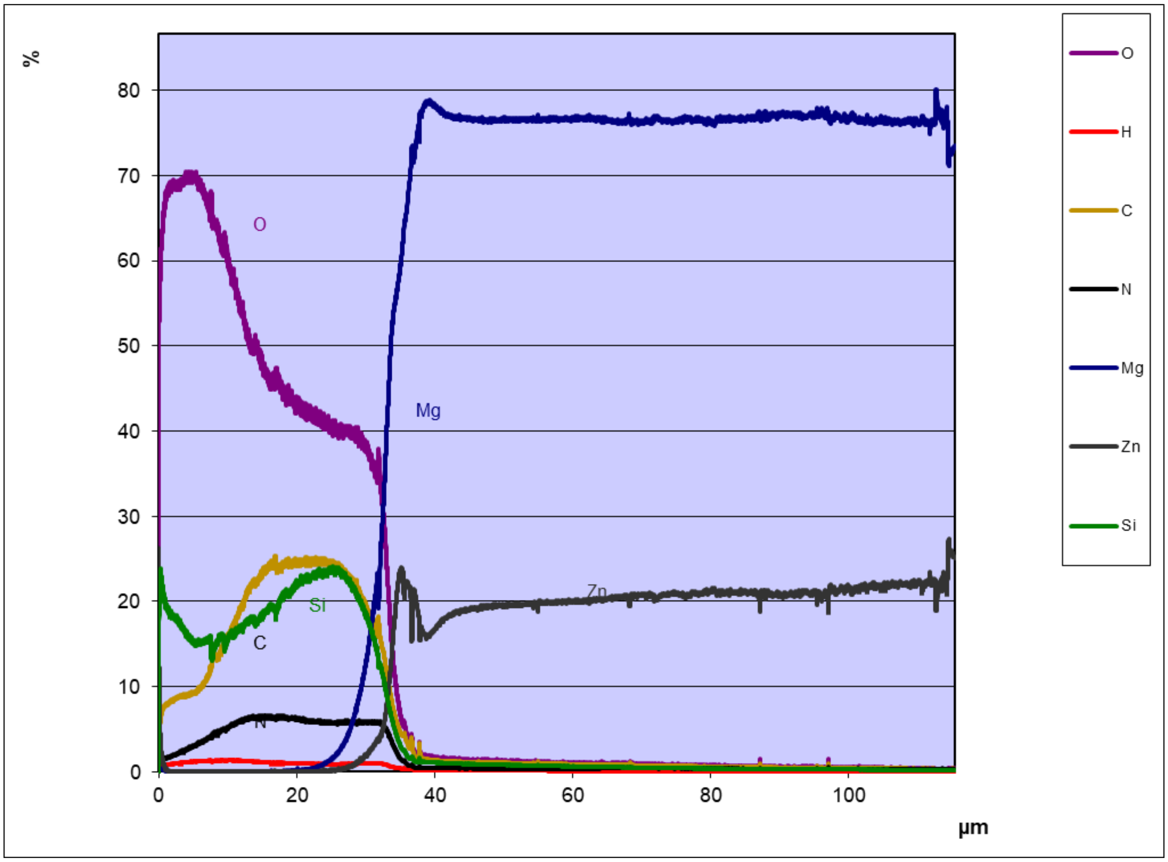

Figure 7.7. GDOES surface/depth profile of chitosan_WG coating deposited on MgZn alloy.

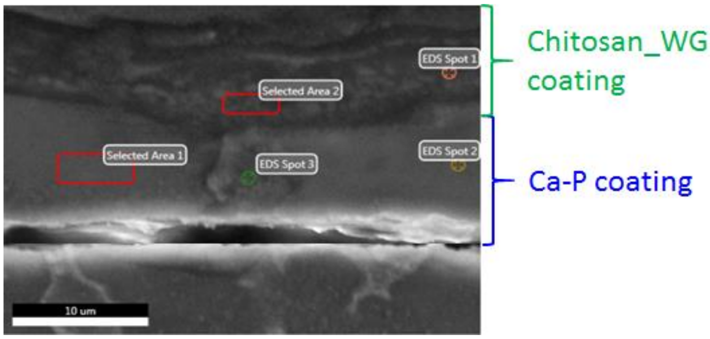

Figure 7.8. Cross section of the Ca-P/chitosan_WG coating.

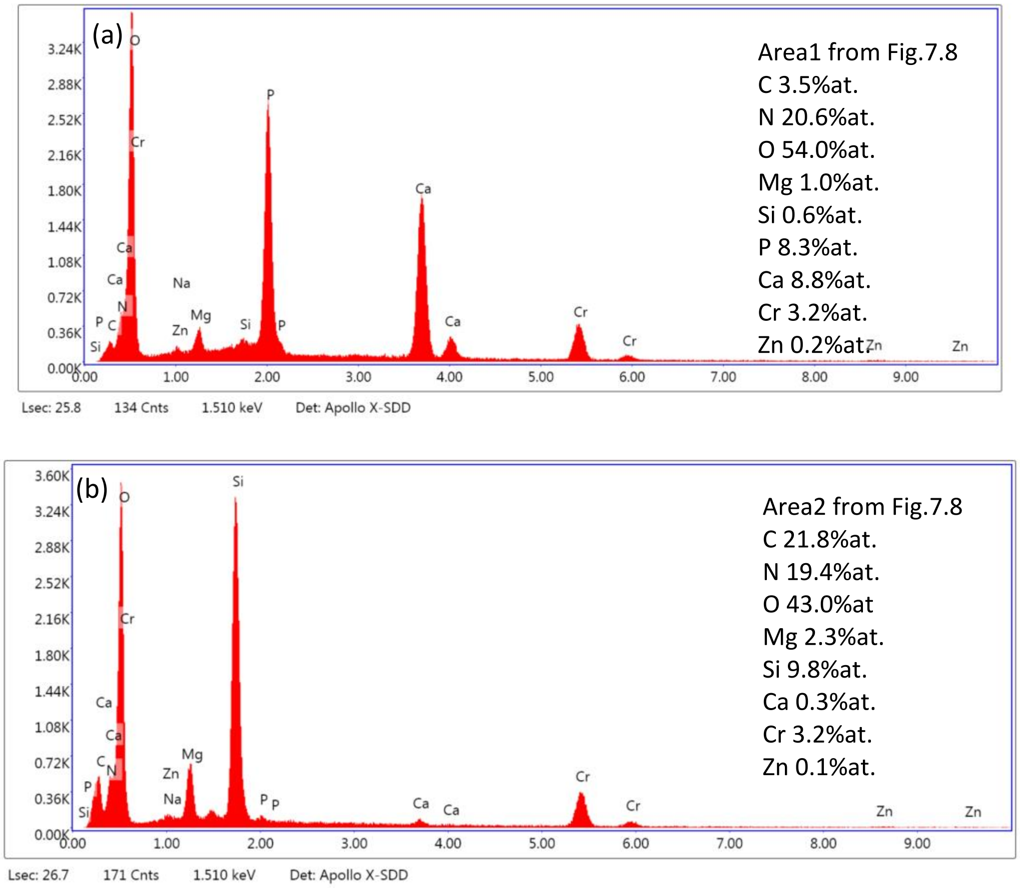

Figure 7.9. EDS spectra measured for selected areas in Figure 7.8: area 1(a), area 2 (b).

The roughness of chitosan-based coatings has been measured by means of optical profilometry. Figure 7.10 shows the images of chitosan_WG and chitosan/TiO_2 coatings deposited on a Mg20Zn substrate. The roughness (R_a) of the chitosan/TiO_2 coating measured by optical profilometry was in the range from 900 nm and 1.1 μm while the roughness (R_a) of chitosan_WG was between 5.7 and 7.7 μm.

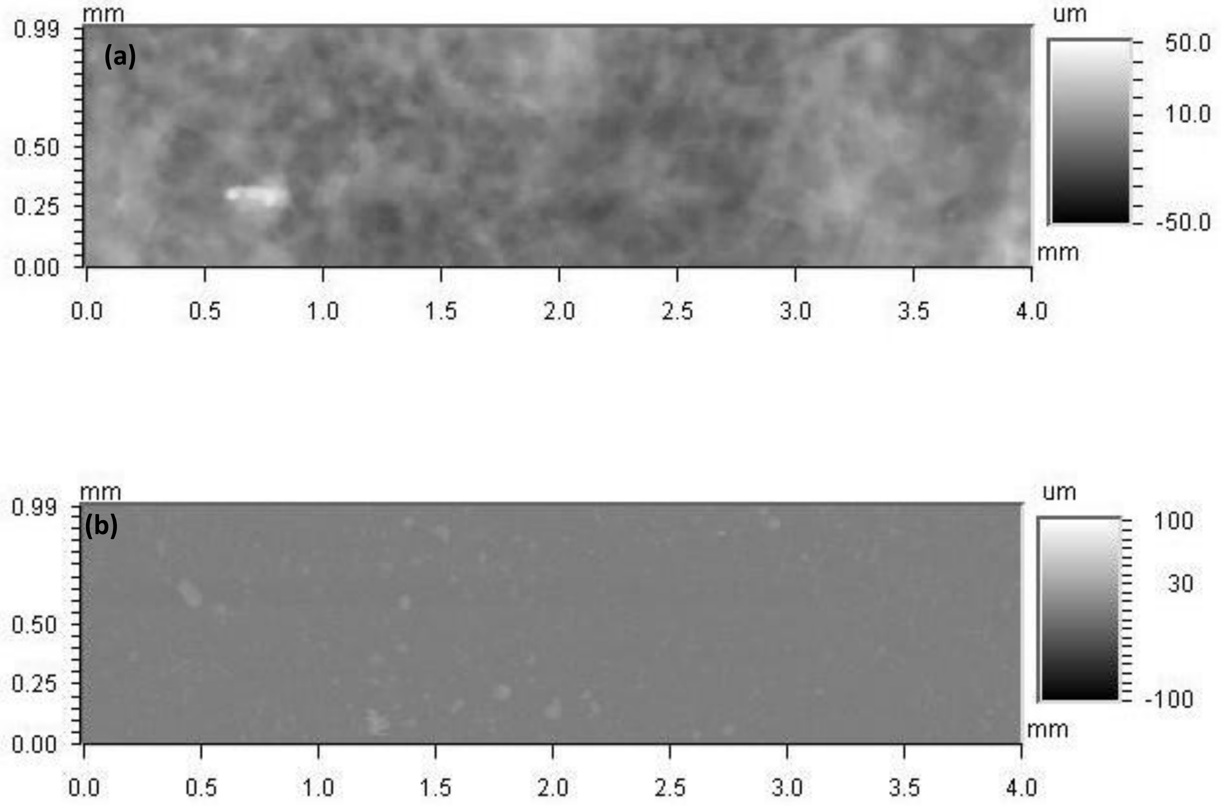

Figure 7.10. Images of chitosan_WG (a) and chitosan/TiO_2 (b) coatings deposited on Mg20Zn substrate. Images obtained via optical profilometry.

7.3. Spectroscopic investigation of chitosan-based coatings.

Fourier Transform Infrared Spectroscopy (FTIR) and X-ray photoelectron spectroscopy (XPS) were used to study the structure and chemical composition of chitosan-based coatings. These techniques give complementary information. The XPS technique shows not only what elements are present in a coating, but also shows the electronic state of the atoms within a material. FTIR measurements allow for the identification of the chemical bonds in chitosan-based coatings.

7.3.1. FTIR investigation of chitosan-based coatings.

In Figure 7.11, the FTIR spectra obtained for chitosan-based coatings are presented. It can be noticed that for chitosan, the main band appearing in the spectrum (black curve, Figure 7.11 (a)) is due to stretching vibration of hydroxyl (OH) and N-H groups in the range from 3358 cm^{-1} to 3285 cm^{-1} and C-H bond in -CH_2 (v = 2930 cm−1), and -CH_3 (v = 2872 cm^{-1}) groups, respectively [171, 217]. The band at 1590 cm^{-1} , however, is assigned to –NH group with bending vibration [168]. In addition, the bands revealed at 1386 cm^{-1} and 1023 cm^{-1} are related with the stretching vibration of the C-O-C bound. The spectrum of chitosan with TiO_2 nanoparticles (gray curve, Figure 7.11 (a)) exhibits bands related to Ti-O bonding at approximately 635 cm^{-1} and 1386 cm^{-1} [216, 217]. The addition of TiO_2 nanoparticles causes an increase of intensity of the signal in the range of 3500 – 2750 cm^{-1} corresponding to the O-H, N-H and C-H groups. In addition, a strong enhancement and broadening of the bands for N-H and C-N are visible. Compared with the chitosan spectrum, the broader and stronger peaks are moved to lower wavenumbers for the chitosan/TiO_2 coating (for example, from 3358 cm^{-1} to 3183cm^{-1}, from 2872 cm^{-1} to 2860, from 1596 cm^{-1} to 1545 cm^{-1}, for chitosan and chitosan/TiO_2 coatings, respectively), indicating the interaction between the groups of O-H, N-H, C-N and TiO_2 nanoparticles. These results showed that –OH and/or –NH_2 groups from the chitosan chains may interact with TiO_2 nanoparticles to form covalent or hydrogen bonds [218]. This interaction of chitosan molecules with the TiO_2 nanoparticles was observed in reference [219]. The characteristic bands observed from 700 to 500 cm^{-1} are attributed to the Ti–O–C bending mode and Ti–O–Ti stretching vibration. The interaction of TiO_2 nanoparticles with functional groups present in the chitosan chain ensures their uniform distribution in the polymer matrix (chitosan matrix).

Figure 7.11 (b) shows the FTIR spectrum of the chitosan_WG coating (blue curve). The broad band at 1025 cm^{-1} is related to Si-O stretching vibrations in dimers $[Si_2O_7]^{6-}$ and $[SiO_3]^{2-}$. A hump at 15860 cm^{-1} appears in the band between 1700 cm^{-1} and 1500 cm^{-1}, originating from the bending and stretching modes of OH groups. The shoulder at 880 cm^{-1} is associated with the asymmetric vibration isolated $[SiO_4]^{4-}$ groups [220-222]. The FTIR spectrum of the Ca-P/chitosan_WG is similar to that of the chitosan_WG coating, but all peaks have lower intensities (black curve, Figure 7.11 (b)). The FTIR spectrum obtained for the CaP coating (green curve in Figure 7.11 (b)) shows the adsorption bands from 528 cm^{-1} to 1150 cm^{-1} assigned to phosphate groups [223].

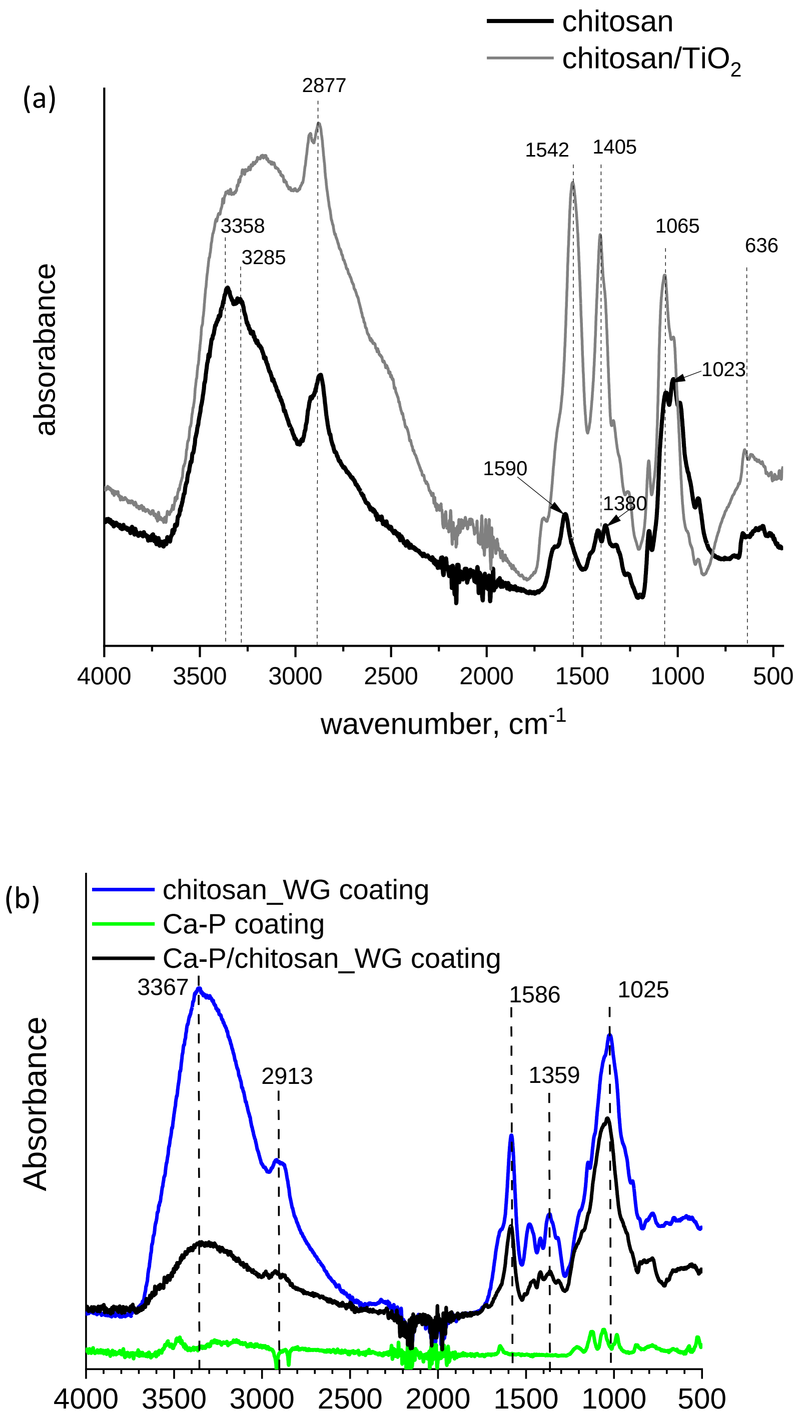

Figure 7.11. FTIR spectra obtained for chitosan-based coatings [210, 211]

7.3.2. XPS investigation of chitosan-based coatings.

The oxidation state of the elements present in chitosan has been investigated by using X-ray photoelectron spectroscopy (XPS). In Figure 7.12, XPS spectra of chitosan coating are presented.

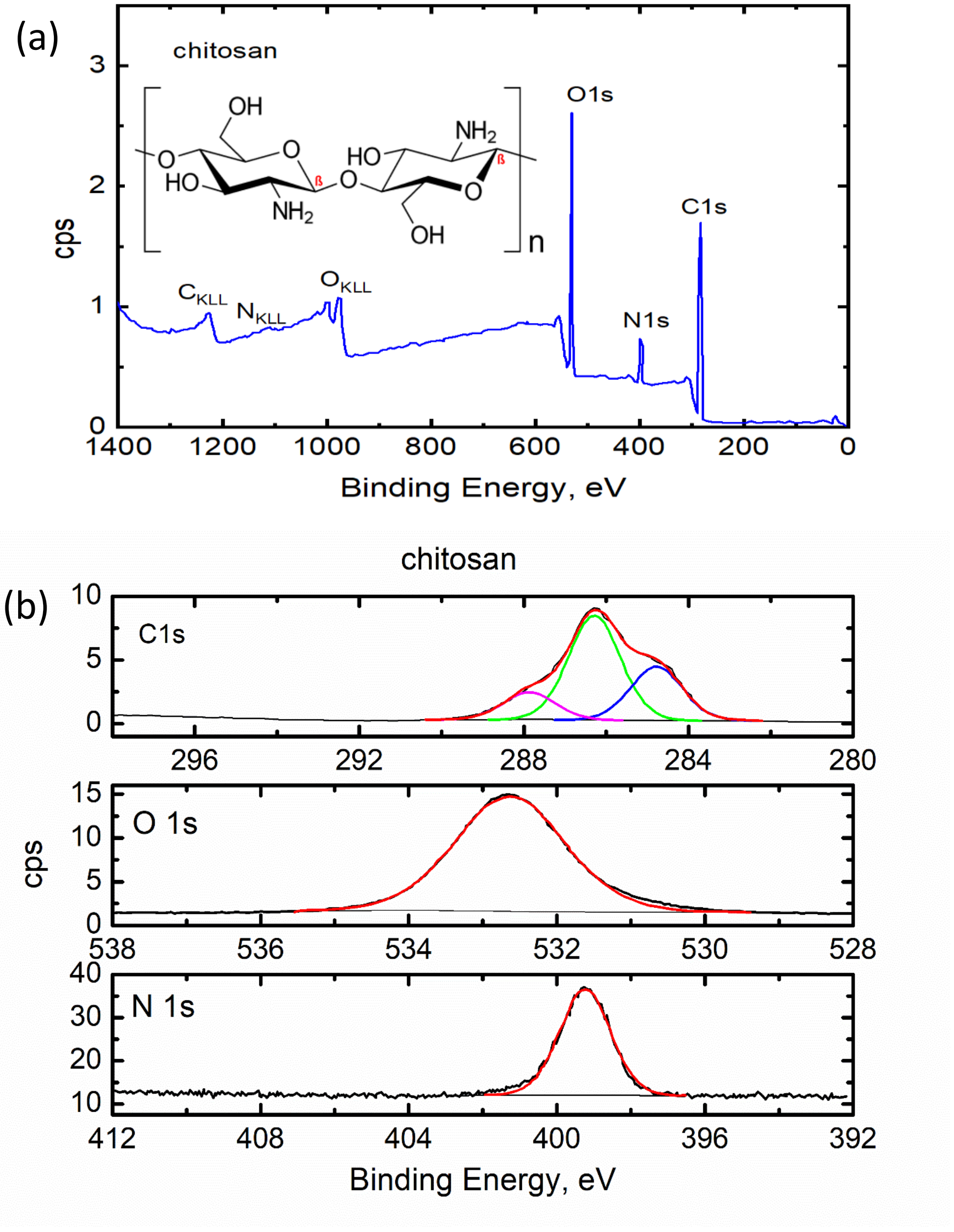

Figure 7.12. XPS spectra obtained for chitosan coating (a) and XPS spectra in individual band C1s, O1s and N1s (b).

The chitosan coating consists of 62.7 at.% carbon, 29.6 at.% oxygen and 7.7 at.% nitrogen. The XPS spectra recorded for the chitosan coating in the individual bands C1s, O1s and N1s are presented in Figure 7.12 (b). The C1s spectrum was decomposed into three peaks. The peaks present in the C1s, O1s and N1s photoelectron spectra are related to the chemical bounds present in the chitosan molecule [224]. The peaks at 284.77 eV, 286.27 eV, and 287.86 eV are attributed to C-C/C-H, C-N and C=O chemical bounds, respectively. In the O1s spectrum, only one peak at 532.6 eV is attributed to the hydroxyl group. The peak at 399.24 eV recorded in the N1s spectrum is assigned to the C-NH2 bound.

XPS analysis has been performed on the Ca-P/chitosan_WG coating. Figure 7.13 shows a survey XPS spectrum of the Ca-P/chitosan_WG coating. Quantitative analysis of XPS data shows that the chitosan_WG coating contains 18.2 at.% carbon, 1.7 at.% nitrogen, 53.3 at.% oxygen, 4.6 at.% sodium, and 22.0 at.% silicon. Figure 7.14 (a–f) shows the C1s, O1s, Na1s, Si2p, Ca2p, and N1s XPS levels of the Ca-P/chitosan_WG coating. The C1s spectrum was deconvoluted into three contributions. The peaks at 284.78 eV, 286.15 eV, 288.0 eV are attributed to C-C/C-H, C-N, and C=O/C-OH chemical bonds, respectively. The peak at the binding energy 399.24 eV, recorded in the N1s spectrum, is assigned to C-N bond present in the chitosan molecule [224]. The peaks at the binding energy 530.31 eV and 532.6 eV are assigned to O^{2-} and SiO_2/CaO, respectively [225]. One peak at the binding energy 1072.01 eV present in the Na1s spectrum is attributed to Na_2SiO_3 [226]. The peak at the binding energy 103.3 eV present in the Si2p spectrum is assigned to SiO_2 [225, 227]. Figure 7.14 (f) shows the typical bands 2p3/2 and 2p1/2 of the Ca2p orbital located at 347.2 and 351.03 eV, respectively. The peak at 347.2 eV corresponds to the Ca-O bond of $CaSiO_3$ [228].

XPS analysis performed for the chitosan/TiO_2 coating has revealed that this coating consists of 56.3 at. % carbon, 34.8 at. % oxygen, 7.2 at. % nitrogen, 1.7 at. % Ti. Figure 7.15 presents the XPS spectra recorded for the chitosan/TiO_2 coating in the individual bands C1s, O1s, N1s, Ti2p. The peaks present in the C1s, O1s and N1s photoelectron spectra are related to the chemical bounds present in the chitosan molecule [224]. The multiple peaks fitted from the C1s spectrum (Figure 7.15 (a)), the binding energy of 284.8 eV, 286.3 eV, and 287.8 eV correspond to C-C/C-H, C-N and C=O chemical bounds, respectively. In the O1s spectrum (Figure 7.15 (b)) two peaks at the binding energy of 529.2 eV and 531.3 eV can be assigned to oxide ions in TiO_2 and titanium oxynitride TiOxNy, respectively [229]. The single peak fitted from the Ti2p XPS spectrum located at the binding energy 457.6 eV is associated with the presence of Ti (III) in the titanium oxynitride Ti-O-N, Figure 7.15 (c) [230-232]. The peak located at 398.0 eV recorded in the N1s spectrum (Figure 7.15 (d)) is assigned to Ti-N bound [230, 231]. The peaks present in the Ti2p and N1s bands confirm the interaction of TiO_2 nanoparticles with the functional groups present in the chitosan molecule.

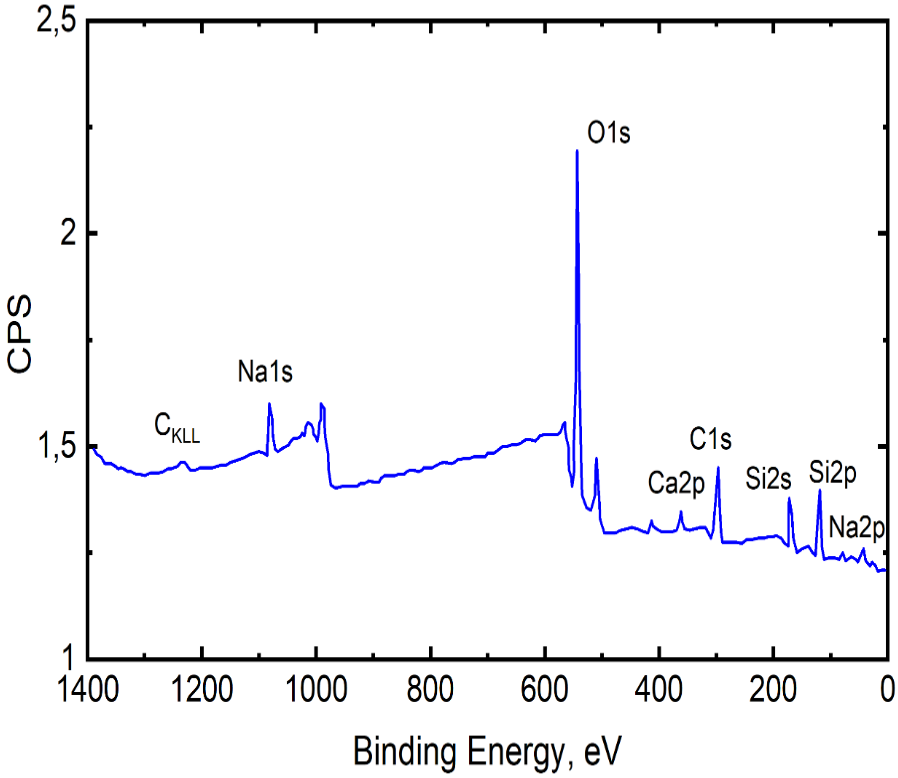

Figure 7.13. Survey XPS spectrum of the CaP_chitosan_WG coating.

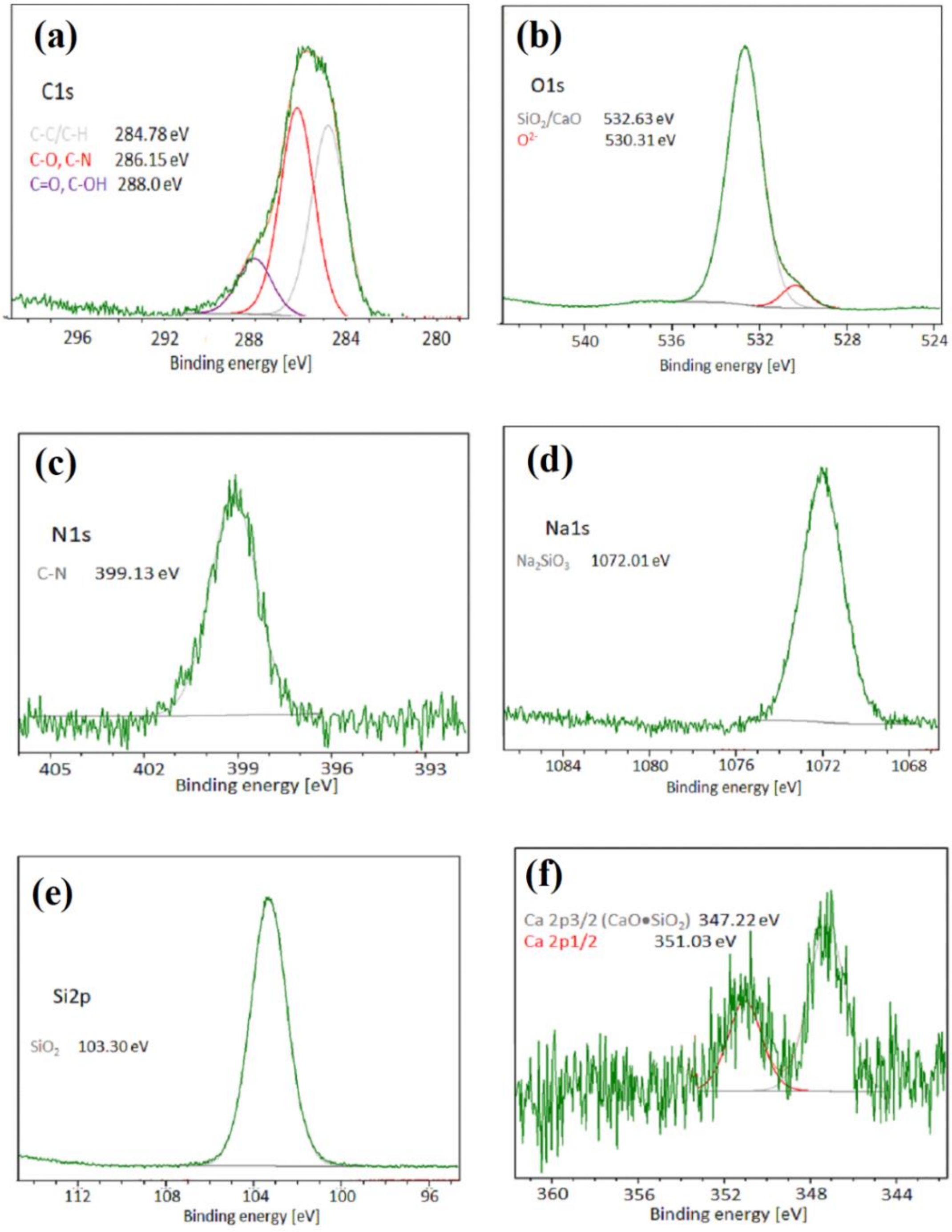

Figure 7.14. XPS spectra of the Ca-P/chitosan_WG coating recorded in (a) C1s, (b) O1s, (c) N1s, (d) Na1s, (e) Si2p, and (f) Ca2p levels [210].

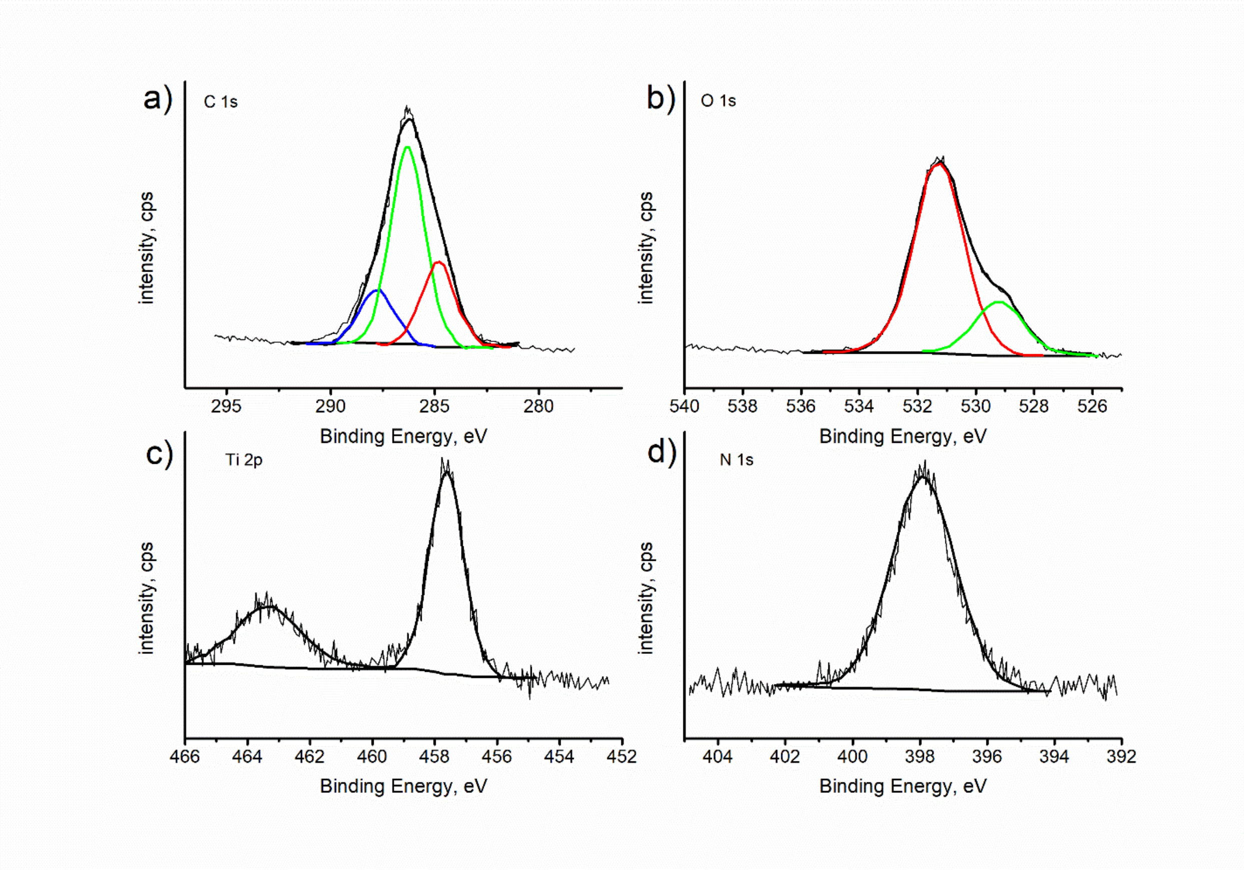

Figure 7.15. XPS spectra of chitosan/TiO_2 coating recorded in C1s, O1s, Ti2p and N1s levels [211].

7.4. Summary of chapter VII

In the binary Mg20Zn and ternary Mg19Zn1Ca alloys, the intermetallic phases are located along the grain boundaries. Addition of 1%wt. of calcium to MgZn causes refinement of the microstructure. The presented results have revealed that the structure and the thickness of chitosan-based coatings do not depend on the substrate (Mg20Zn, Mg19Zn1Ca). The chitosan-based coatings were uniformly deposited on the substrates. The chitosan/TiO_2 coating was the thinnest and showed the least roughness. FTIR and XPS measurements support the existence of TiO_2 nanoparticles-chitosan matrix interactions. Such interaction of TiO_2 nanoparticles with functional groups present in the chitosan chain ensures their uniform distribution in the polymer matrix. During the deposition of Ca-P/ chitosan_WG coating $CaSiO_3$ ($CaO \bullet SiO_2$) is formed.

Chapter VIII

Corrosion resistance of coated and uncoated Mg20Zn and Mg19Zn1Ca

in the Hank's solution

8.1. Corrosion behavior of coated and uncoated magnesium alloys under potential control

As mentioned in Chapter VI, the corrosion tests for coated and uncoated magnesium alloys were performed in Hank's solution. The chemical composition of this solution is like that of human body fluid. All corrosion tests were performed at 37°C. Chapter VIII presents the results of corrosion tests which allow for an estimation of the corrosion resistance of magnesium alloys before and after the application of protective chitosan-based coatings. In addition, the corrosion rate of the tested materials was also calculated, and a characterization of corrosion products was carried out.

8.1.1. Potentiodynamic polarization measurement for Mg and uncoated alloys

Figure 8.1. demonstrates the comparison of the potentiodynamic polarization curves (LSV) performed for pure Mg, Mg20Zn and Mg19Zn1Ca alloys in Hanks' solution. The potentiodynamic polarization curves were plotted in the potential range from -1.8 V to -1.2V vs. Ag/AgCl (3M KCl) reference electrode. The corrosion potential was: -1428 mV for Mg, -1431 mV for Mg19Zn1Ca, and -1424 mV for Mg20Zn alloy, respectively.

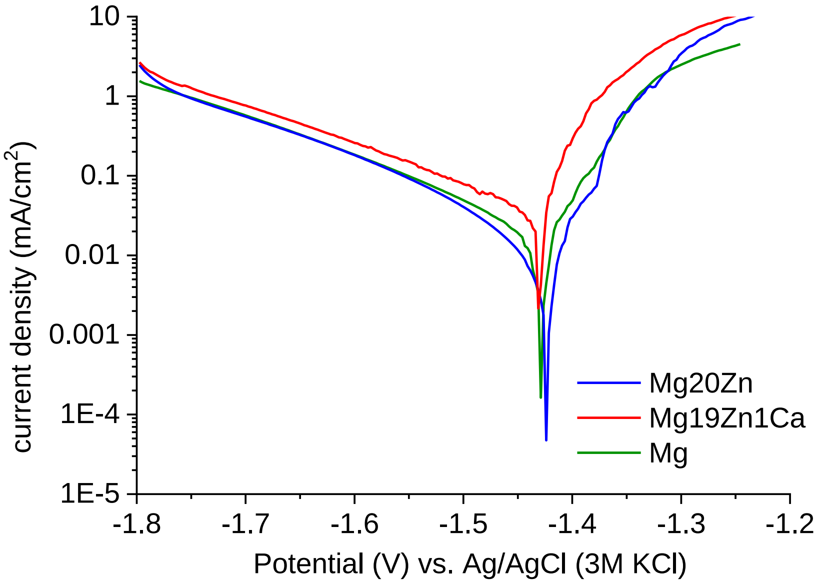

Figure 8.1. Comparison of LSV measurement for pure Mg (green curve), Mg20Zn (blue curve), and Mg19Zn1Ca (red curve). LSV curves performed in Hanks' solution. The potential scan rate was 1mV/s.

A slightly higher current density in the cathodic branch was measured for the Mg19Zn1Ca alloy, red curve Figure 8.1. This result suggests that cathodic reactions (oxygen reduction, water reduction) are promoted at the surface of the Mg19Zn1Ca alloy. A slightly higher value of the current density in the anodic branch was also measured for the Mg19Zn1Ca alloy, red curve Figure 8.1. The corrosion current obtained from the analysis of potentiodynamic polarization curves was 6 $\mu A/cm^2$, 16 $\mu A/cm^2$, 30 $\mu A/cm^2$ for Mg20Zn, pure Mg and Mg19Zn1Ca, respectively. Both alloys exhibit active electrochemical behavior like pure magnesium in Hank's solution.

To improve the corrosion resistance of magnesium alloys, chitosan-based coatings were deposited by using the spin-coating method. The experimental procedure for the deposition of chitosan coatings is described in Chapter VI. Inorganic coatings such as Ca-P were also applied to some magnesium alloys. To increase corrosion resistance, double inorganic/organic coatings were also applied to magnesium alloys, e.g. Ca-P and a chitosan-based coating.

8.1.2. Corrosion behavior of uncoated and coated Mg20Zn, Mg19Zn1Ca alloys

The uncoated and coated specimens of Mg20Zn alloy were immersed in Hanks’ solution for 30 minutes, and then the polarization curves were plotted from -100 mV vs. OCP to the anodic direction. In Fig. 8.2, the polarization curves of the coated and uncoated substrate (Mg20Zn) are depicted. The corrosion potential of the bare, uncoated Mg20Zn alloy is located at approximately −1.433 V, while the corrosion potential is shifted to the more anodic direction for the coated specimens. The value of corrosion potential for the Mg20Zn alloy is -1.403 V for pure chitosan coating, -1.392 V for Ca-P coating, -1.381 V for chitosan_WG, and -1.256 V for sandwich coating Ca-P/chitosan_WG, respectively. The current density in the anodic branch of the Mg20Zn substrate (black curve) increases sharply with increasing applied potential, exhibiting active behavior. The three mono-layer coatings (Ca-P (orange curve) and chitosan_WG coatings (blue curve)) and chitosan coating (red curve) have similar behaviors. For the specimens covered with these coatings, the current density in the anodic branch increases significantly, but the values are lower than those obtained on the bare Mg20Zn substrate. This shows that the presence of these three coatings has a beneficial influence on the kinetics of anodic reactions. Note that the chitosan_WG coating performs slightly better than the Ca-P and chitosan coatings (lower anodic current densities). The increase of current density in the anodic branch is more marked on the chitosan_WG coating (blue curve) than on the Ca-P/chitosan_WG coating (green curve), Fig. 8.2. This may be related to the presence of cracks in the coatings which provide new pathways for electrolyte penetration (see chapter 7, Fig.7.4).

The presence of the multilayer coating (Ca-P/chitosan_WG coating) induces a sharp decrease of the current density in the anodic branch (green curve, Figure 8.2), leading to a huge shift of the corrosion potential to the anodic direction (of about 0.2 V with respect to the value obtained on the substrate). It should be emphasized that the anodic current density measured at an applied potential of −1.2 V is 12.25 mA/cm2 on the Mg20Zn alloy, between 1 and 2.5 mA/cm2 on the two monolayer coatings, and only 0.05 mA/cm2 on the Ca-P/chitosan_WG coating. These results indicate that the specimen covered by the multilayer coating (Ca-P/chitosan_WG) has the highest corrosion resistance in Hanks' solution and that the simultaneous presence of the two sublayers increase this resistance.

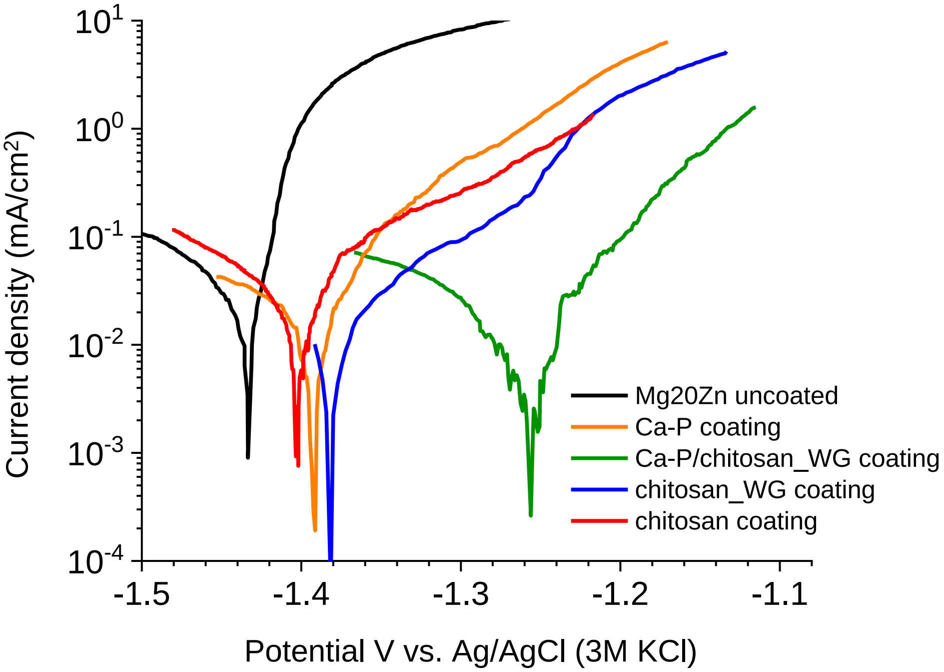

Fig.8.2. LSV curves plotted in Hanks' solution for Mg20Zn substrate (black curve), and substrate covered by the following coatings: chitosan (red curve), Ca-P (orange curve), chitosan_WG (blue curve) and Ca-P/chitosan_WG coating (green curve). The curves were plotted with the potential scan rate of 1mV/s.

The magnesium alloy Mg19Zn1Ca was covered by the following coatings: chitosan with the addition of hydroxyapatite (chit_HA), chitosan with the addition of titanium dioxide (chit_TiO_2), chitosan with the addition of water glass and Na_2SiO_3 (chit_WG), and a multilayer coating Ca-P/chit_WG. Fig. 8.3 shows the polarization curves of the Mg19Zn1Ca alloy (uncoated substrate) and the substrate covered by the chitosan-based coatings. A sharp increase of the current density is observed with increasing applied potential in the anodic domain (active behavior) for all uncoated and coated specimens. The most active corrosion behavior is exhibited by the magnesium alloy covered by the chitosan coating containing the hydroxyapatite powder, grey curve, Fig.8.3. The corrosion potential of the specimen marked as “chit_HA” is shifted by 100 mV to the cathodic direction compared to the corrosion potential of the uncoated substrate. The corrosion potential for specimens covered by other coatings is shifted to a more anodic direction compared to the uncoated substrate. The lowest current densities in the cathodic and anodic branches is exhibited by the Mg19Zn1Ca alloy coated by the double coating Ca-P/chit_WG, green curve Fig.8.3. This curve is very similar to the polarization curve obtained for Ca-P/chit_WG deposited on the Mg20Zn alloy, Fig.8.2. Such a result indicates that the substrate does not play a crucial role in the deposition of the chitosan-based coatings and their corrosion resistance. The current density in the anodic branch is much lower for the magnesium alloy coated with chit_WG (blue curve) and chit_TiO_2 (red curve) compared to the uncoated substrate, Fig.8.3. For example, the anodic current density registered at a potential of −1.3 V (the potential located in the anodic domain) is 5.2 mA/cm^2 for the Mg19Zn1Ca alloy and only 0.28 mA/cm^2 on the magnesium alloy covered with the chitosan/TiO_2 coating. The corrosion potential of the magnesium alloy coated with the chitosan/TiO2 coating is shifted toward higher values (of about 0.07 V) compared to that recorded for the pure substrate. Therefore, the presence of the chitosan/TiO_2 coating has a beneficial influence on the kinetics of anodic reactions. These results show that the specimen covered by chitosan/TiO_2 coating has a high corrosion resistance in Hanks’ solution.

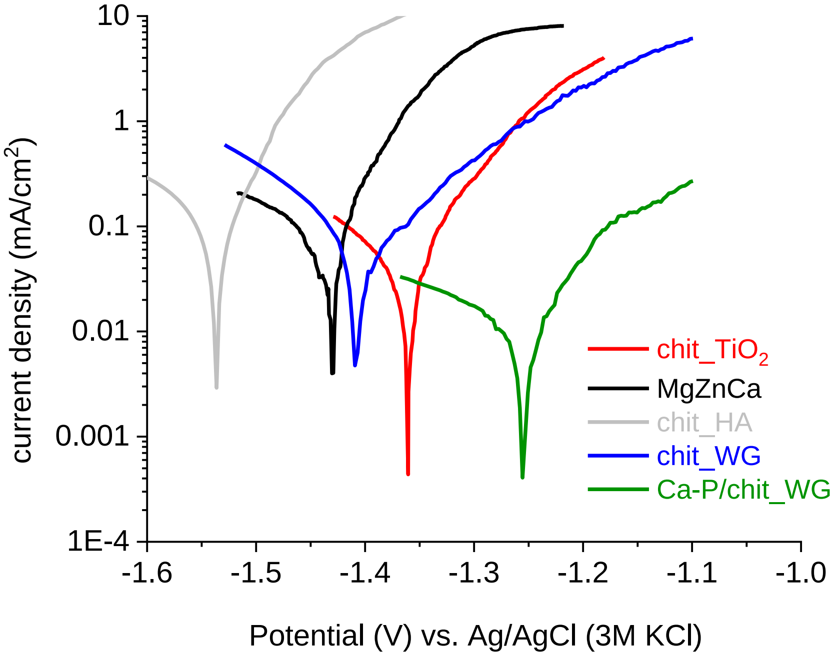

Figure 8.3. LSV curves performed for uncoated (black curve) and coated Mg19ZnCa alloy in Hanks' solution.

To check the electrochemical activity in the anodic domain of magnesium alloys, the chronoamperometry test was performed at the potential -1.25 V vs. Ag/AgCl (3M KCl). Figure 8.4 shows the evolution of the current density versus time at the potential -1.25 V for pure Mg20Zn and Mg19Zn1Ca alloys. The current density at the beginning of the chronoamperometry test is very high for both alloys, but sharply decreases, and then achieves a stable value of about 12 mA/cm^2 after 500 seconds, Fig.8.4. The decrease of the current density is related to the anodic dissolution of magnesium alloys and formation of the corrosion products, which are deposited on the surface of magnesium alloys. To reveal the changes at the surface of the magnesium alloys caused by anodic dissolution, the chronoamperometry test was performed for 120 seconds at the potential -1.25 V. Fig.8.5 shows the morphology of the surface of the magnesium alloys after the chronoamperometry test. The bare Mg20Zn and Mg19Zn1Ca alloys undergo oxidation, and an uneven distribution of corrosion products is visible, Fig. 8.5. In general, the corrosion products are formed in the matrix, whereas the intermetallic phases do not undergo corrosion.

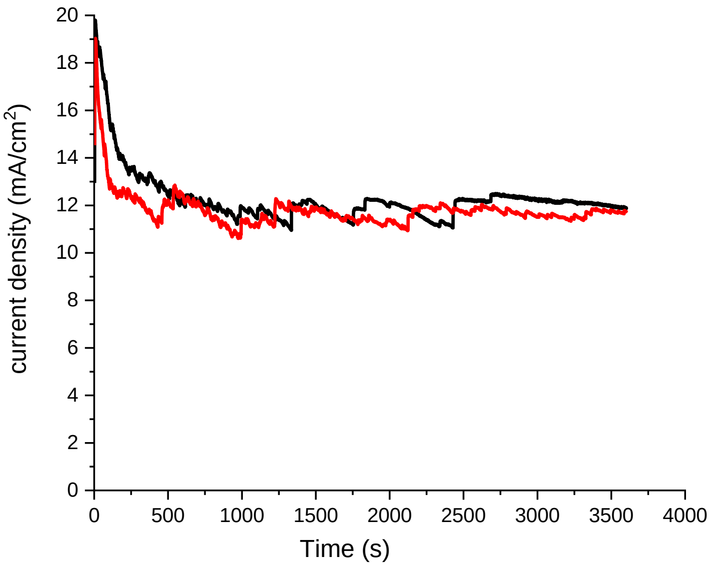

Fig.8.4. Evolution of the current density at -1.25 V vs. Ag/AgCl (3M KCl) for bare alloys Mg20Zn (black curve) and Mg19Zn1Ca (red curve).

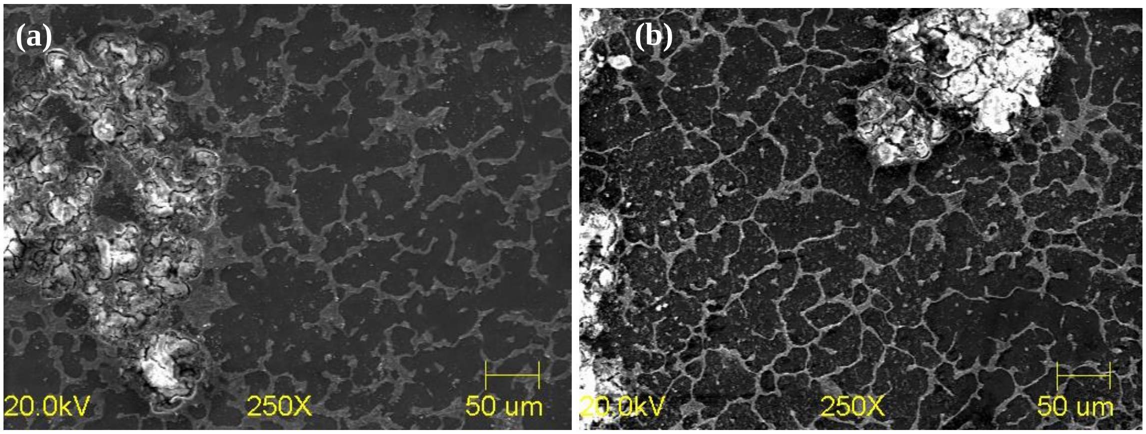

Fig. 8.5. Morphology of the surface of Mg20Zn (a), Mg19Zn1Ca (b) alloys after chronoamperometry test at E= -1.25V for 120 seconds in Hanks' solution.

The chemical composition of corrosion products verified using EDS analysis confirmed the presence of magnesium (37.0 at.%), zinc (3.7 at.%), chlorine (3.7 at.%) and oxygen. Therefore, the corrosion products are a mixture of magnesium oxide, zinc oxide and small amount of adsorbed chloride ions from the solution. Chloride was not found either at the surface of the unoxidized matrix or at the intermetallic phase. The chloride ions were preferentially adsorbed on the corrosion products.

A similar chronoamperometry test was performed for the magnesium alloys coated by chitosan_WG coating. In Fig. 8.6, surface views of the coated magnesium alloys and EDS spectra are presented.

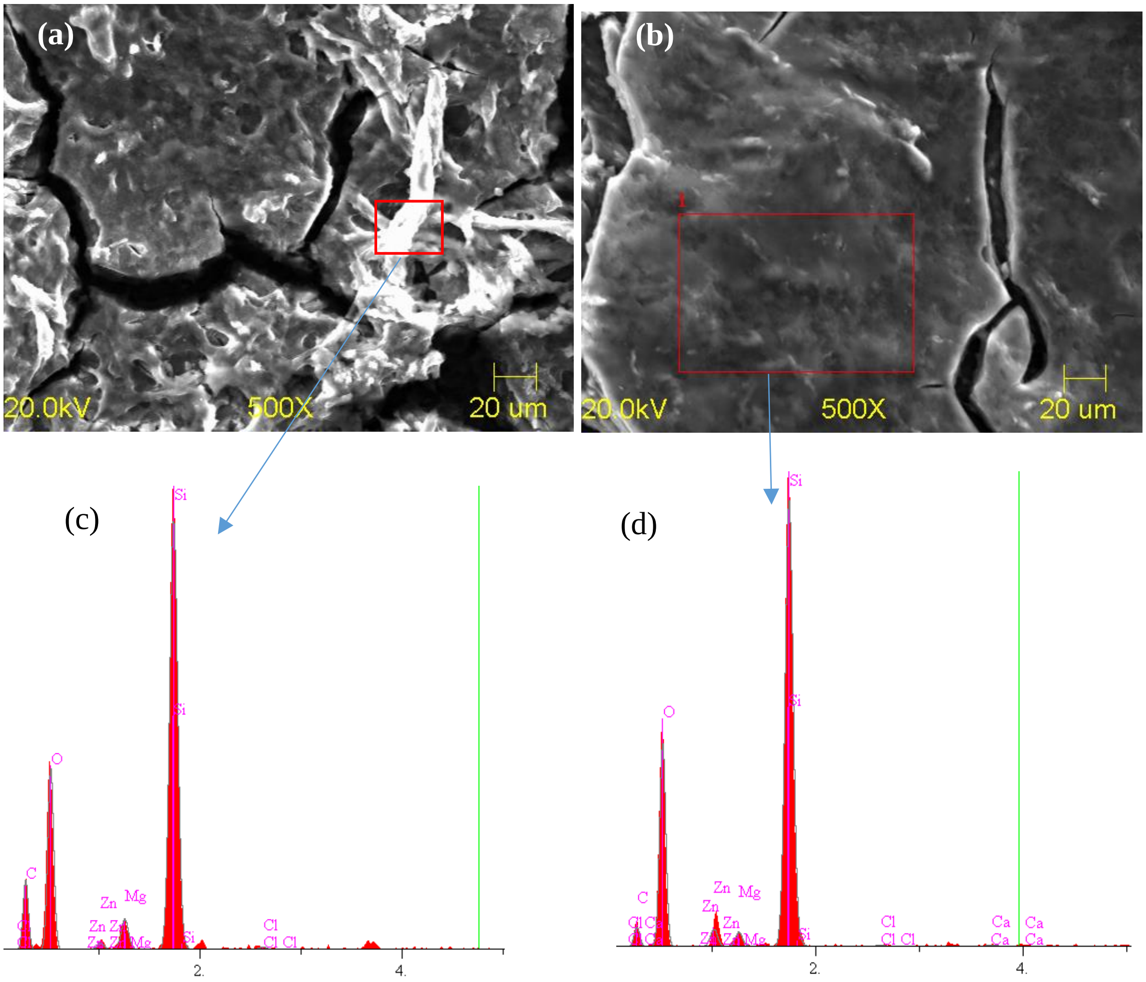

Fig.8.6. Morphology of the Mg20Zn (a) and Mg19Zn1Ca (b) alloys coated with chitosan_WG coating after chronoamperometry at -1.25 V for 120 seconds in Hanks' solution. EDS spectra for coated Mg20Zn (c) and coated Mg19Zn1Ca (d).

On the surface of the chitosan_WG coating, after the chronoamperometry test microcracks are visible, Fig. 8.6 (a, b). Chemical analysis of the coating revealed the presence only of silicon, oxygen, and carbon, but no chloride was detected on its surface, EDS analysis Fig.8.6 (c, d). Moreover, no magnesium or zinc were found on the surface of the chitosan_WG coating, which suggests that the coating protects the substrate well against corrosion in Hank's solution. Even the presence of surface micro-cracks does not accelerate the corrosion of the magnesium alloys substrate.

8.1.3. Electrochemical impedance spectroscopy (EIS)

Electrochemical impedance spectroscopy (EIS) is considered to be a non-destructive method for investigating the corrosion mechanisms of alloys [76]. Fig. 8.7 (a, b) shows the EIS spectra for the uncoated Mg19Zn1Ca alloy immersed in Hanks' solution at the OCP value for 2 and 7 hours. These spectra were fitted using the electrical equivalent circuit shown in Fig. 8.7 (c). It is composed of the solution resistance (R_s) at high frequencies and a combination of components (CPE // R_{ct} // L- R_L) at medium and low frequencies. CPE is a constant phase element (corresponding to the formation of oxides at the interface solution/alloy) R_{ct} is the charge transfer resistance, L is inductance, and R_L is inductance resistance. The constant phase element (CPE) is used to simulate the capacitive response of a non-ideal capacitor, due to the heterogeneous nature of the electrode surface. The impedance of the constant phase element (CPE) is given in equation (8.1).

$$Z_{CPE} = \frac{1}{Y(j\omega)^n} \qquad (8.1)$$

where Y is the value of admittance expressed in (S cm^{-2} s^{n}), ω is the angular frequency (rad s^{-1}), j is the imaginary number (j2 = (-1)), and n is a dimensionless fractional exponent. When n = 1, 0 or -1, the CPE represents an ideal capacitor, a resistance, and an inductor, respectively. The inductive loop in the low-frequency range is mainly associated with the adsorption of corrosion products and/or pitting corrosion initiation [233-236]. The numerical values of the components of the equivalent circuit are listed in Table 8.1.

A slight increase in the charge transfer resistance (R_{ct}) and the inductance resistance (R_L) is observed with increasing immersion time (by a factor of ~1.2). The incubation time T_L of pitting corrosion was calculated from the numerical values of the components of the inductive loop [237], equation (8.2).

$$T_L = \frac{L}{R_L} \qquad (8.2)$$

TL was also found to slightly increase with increasing immersion time (from 2.6 seconds after a 2-hour immersion up to 4.6 seconds after a 7-hour immersion). Therefore, the adsorption of corrosion products on the specimen surface partly inhibits the corrosion rate and slightly retards the initiation of pitting corrosion. Corrosion products are mainly composed of $Mg(OH)_2$, $Mg_3(PO_4)_2$ and $CaCO_3$ [210, 238].

These results were confirmed by determining the numerical values of the polarization resistance (Rp) from the linear polarization resistance (LPR) method [76]. LPR measurements were performed in Hanks' solution. The potential scan rate was set at 0.125 mV/s and the potential range was [-25, +25] mV vs OCP (OCP was previously measured for 30 min). R_p was found to be equal to 214 ± 60 $\Omega.cm^2$ and 952 ± 250 $\Omega.cm^2$ for the uncoated and coated magnesium alloys, respectively. Therefore, the value of R_p is decreased by a factor of 4.4 in the presence of the chitosan/TiO_2 coating. These results confirm those derived from the polarization curves, indicating that the Mg19Zn1Ca alloy covered with the chitosan/TiO_2 coating exhibits significantly better corrosion resistance in Hanks' solution compared to the uncoated specimen.

Table 8.1. Fitting results obtained from the EIS spectra of MgZnCa alloy with immersion time in Hanks' solution.

	Rs ($\Omega\cdot cm^2$)	Rct ($\Omega\cdot cm^2$)	Y ($S\cdot cm^{-2}\cdot s_n$)	n	R_L ($\Omega\cdot cm_2$)	L ($H\cdot cm^2$)
2 hours	66.0 ± 0.4	191.9 ± 1.8	2.4·10-4 ± 4·10-6	0.84 ± 0.009	436.5 ± 21	1117.0 ± 87
7 hours	68.0 ± 0.67	239.6 ± 2.5	2.9·10-4 ± 1.3·10-5	0.84 ± 0.003	489.5 ± 27.0	2229.0 ± 127.0

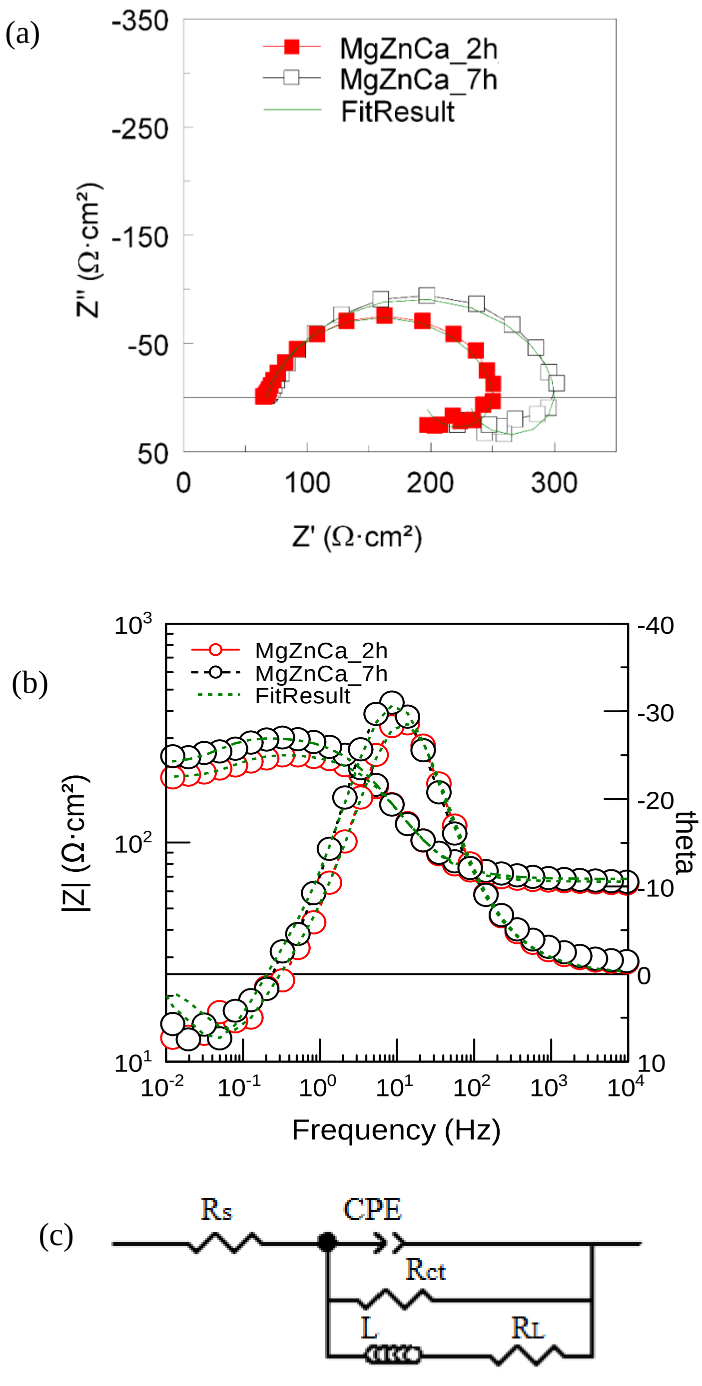

Fig.8.7. EIS spectra measured after immersion of MgZnCa alloy for 2 and 7 hours in Hanks' solution, (a) Nyquist plots, (b) Bode plot, (c) electrical equivalent circuit used for fitting the experimental spectra.

Fig. 8.8 (a, b) shows EIS spectra (Nyquist and Bode plot) obtained for the Mg19Zn1Ca alloy coated with the chitosan/TiO_2 coating (after immersion for 2 and 7 hours). In the presence of the coating, EIS spectra are different from those obtained on the uncovered alloy. They were fitted considering the equivalent circuit shown in Fig. 8.8 (c). Rs is the solution resistance and Rct the charge transfer resistance. The exponent of CPE1 is close to unity (value of 0.9 in Table 8.2) indicating that it can be considered as a capacitor (capacitive loop observed at medium frequencies). By contrast, the exponent of CPE2 is close to 0.5, indicating that it corresponds to a diffusion process (low frequency range). Corrosion processes were then controlled by the diffusion of species through the chitosan/TiO_2 coating [239]. In contrast to the previous case (uncoated substrate), the value of R_{ct} increases significantly (by a factor of 1.6) with increasing immersion time. Such an increase in R_{ct} is related with the deposition of corrosion products on the surface of the coated specimen. During coating degradation, the alloy is dissolved, and corrosion products are deposited on the electrode surface. The Gerischer impedance was used for describing the diffusion of species involved in the chemical-electrochemical reaction mechanisms from the bulk of the solution to the electrode/solution interface. The Gerischer element is given by equation (8.3).

$$G = Y(k + j\omega) \cdot 0.5 \tag{8.3}$$

where k is the rate constant parameter, ω is the angular frequency (rad s^{-1}), j is the imaginary number (j2 = (-1)). Magnesium cations diffuse through the chitosan/TiO_2 coating, then react with phosphate ions present in Hank's solution. In Hanks' solution, calcium ions react with the carbonate's ions and then the calcium carbonate is deposited on the electrode surface. Magnesium phosphates and carbonates are deposited on the surface of the coated alloy and hinder further dissolution of the substrate.

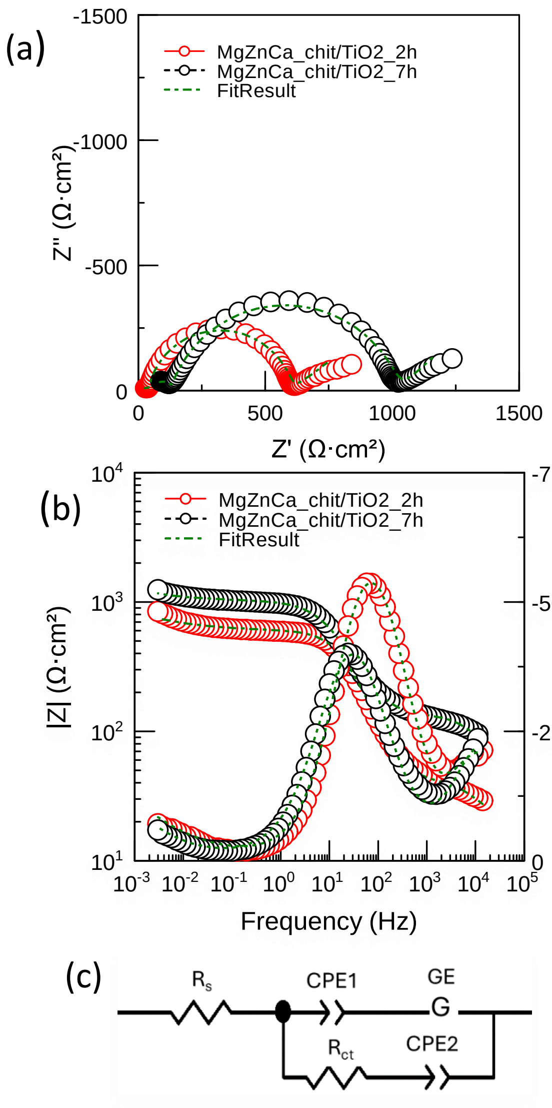

Fig.8.8. EIS spectra performed for the Mg19Zn1Ca_chit/TiO_2 coated alloy after immersion for 2 and 7 hours in Hanks' solution. (a) Nyquist plots, (b) Bode plot, (c) electrical equivalent circuit [211].

Table 8.2. Fitting results obtained from the EIS spectra of the Mg19Zn1Ca alloy coated with chitosan/TiO_2 coating with immersion time in Hanks' solution.

	Rs (Ω·cm^2)	Rct (Ω·cm^2)	Y1 (S·cm^{-2}·s^n)	n1	Y2 (S·cm^{-2}·s^n)	n2	GE-T (S·cm^{-2}·s$^{0.5}$)	GE-P
2 hours	13.2 ± 2.0	585.9 ± 4.9	2.6·10-5± 2.2·10-7	0.9 ± 0.005	0.029 ± 4.4·10-4	0.42 ± 0.017	2.1·10-4± 1.2·10-5	2938± 946
7 hours	33 ± 0.8	991.2 ± 7.3	3.4·10-5± 3.8·10-7	0.82 ± 0.006	5.8·10-5± 2.2·10-	0.49 ± 0.02	0.037± 0.002	27652± 449

8.2. Corrosion rate of coated and uncoated magnesium alloys

8.2.1. Corrosion rate of uncoated and coated Mg20Zn alloy

The corrosion process of magnesium and its alloys proceeds with the hydrogen evolution. Therefore, knowing the volume of hydrogen gas released during the corrosion, the corrosion rate of magnesium can be calculated. The hydrogen evolution method described in reference [224] was used to evaluate the corrosion rate of uncoated and coated Mg20Zn specimens immersed for 7 days in Hanks' solution at 37°C. As it is shown in Chapter VI (Fig.6.3), the hydrogen evolved during the corrosion process was collected in the burette placed above the specimen's surface. Fig. 8.9. shows the evolution of released hydrogen volume versus time collected for coated and uncoated alloy specimens. As can be seen in Fig. 8.9 (a), the volume of released hydrogen increases linearly with time almost immediately after immersion of the uncoated Mg20Zn alloy (green curve). By contrast, hydrogen evolution starts to be observed from an immersion time of roughly 50 h for the two monolayer coatings (Ca-P and chitosan_WG coatings), indicating the onset of corrosion due to the loss of the protective properties of the coatings (orange and blue curves, Fig.8.9 (a)). In the range between 50 and 110 h of immersion, both coatings exhibit similar behavior. From 110 h of immersion, the quantity of hydrogen released is significantly greater for the Ca-P coating than for the chitosan_WG coating, suggesting that the inorganic Ca-P coating degrades faster. These results confirm those derived from polarization curves, Fig.8.2. Both monolayer coatings exhibit similar corrosion behavior, but the chitosan_WG coating has slightly better corrosion resistance than the inorganic Ca-P coating. In the case of the specimen coated with the multilayer coating (Ca-P/chitosan_WG, wine-colored curve, Fig. 8.9 (a)), hydrogen evolution was detected from 90 h of immersion in Hanks' solution. In addition, the quantity of hydrogen released was found to be systematically smaller than in the three other cases (Mg20Zn alloy and the two monolayer coatings). This confirms that the multilayer coating has the highest corrosion resistance.

According to the stoichiometry of reaction (8.4), the evolution of 1 mol of hydrogen gas corresponds to the dissolution of 1 mol of magnesium.

$$Mg + 2H_2O = Mg(OH)_2^- + H_2 \qquad (8.4)$$

Therefore, knowing the volume of hydrogen evolved during the corrosion process, the corrosion rate of magnesium can be calculated based on reaction (8.4). The corrosion rate calculated for uncoated and coated magnesium alloys after exposition in Hanks' solution for 7 days was calculated using equation (6.5), Chapter VI.

Figure 8.9 (b) shows the evolution of the corrosion rates vs. time. The corrosion rate of the substrate increases exponentially vs. time (according to equation (8.5)), to reach a steady state at 3.2 mm/year.

$$v_{corr,substrate} = 3.2 - e^{(-0.02 \cdot time)} \tag{8.5}$$

In the presence of the monolayer coatings (Ca-P and chitosan_WG coatings), the corrosion rate increases faster than in the case of the substrate. For long immersion times (greater than 120 h for the Ca-P coating and 170 h for the chitosan_WG coating), the corrosion rate is greater than values measured on the pure substrate, Fig. 8.9 (b). Severe degradation of the monolayer coatings may be related to the formation of galvanic coupling between the alloy and the coating. This phenomenon is discussed in Section 8.3.

It is remarkable to note that the corrosion rate measured on the multilayer coating increases slowly with increasing time, indicating that this coating has excellent protective properties against corrosion. In contrast to the monolayer coatings, the multilayer coating helps to protect the alloy against corrosion in Hanks' solution. After 173 h of immersion in Hanks' solution at 37 °C, the corrosion rate of uncoated and coated Mg20Zn alloy is as follows: 4.7 mm/year for the Ca-P coating, 3.3 mm/year for the chitosan_WG coating, 3.2 mm/year for the bare Mg20Zn alloy, and only 1.2 mm/year for the multilayer coating (Ca-P/chitosan_WG coating).

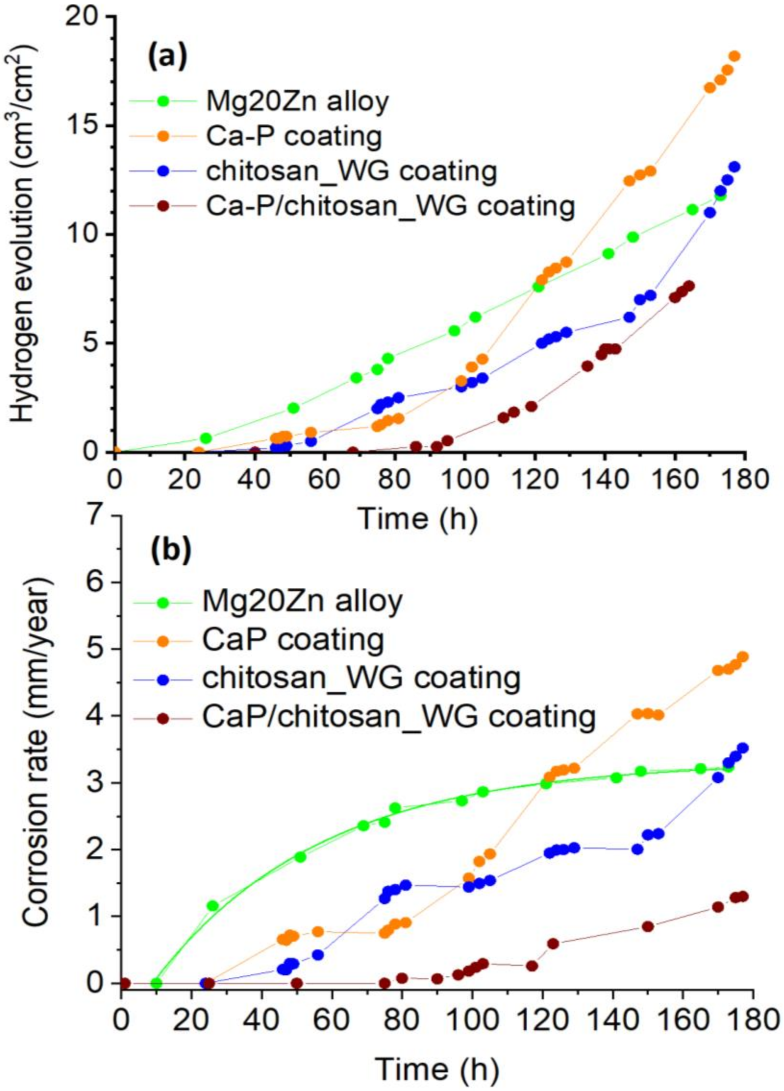

Figure 8.9. (a) Hydrogen evolution vs. time for the Mg20Zn alloy and the different coatings immersed at the OCP in Hanks' solution at 37 °C. (b) Evolution of the calculated corrosion rate vs. time [210].

8.2.2. Corrosion rate of uncoated and coated Mg19Zn1Ca alloy

The corrosion rate of the uncoated and coated Mg19Zn1Ca alloy was calculated by collecting the hydrogen evolved during the corrosion process. This was performed by applying the method described in reference [207, 240]. Samples were immersed at the OCP for 160 hours in Hanks' solution at 37 °C. Fig. 8.10 (a) shows the evolution vs. time of the ratio τ between the volume of released hydrogen and specimen surface area for the two specimens. For the uncoated sample (bare

Mg19Zn1Ca alloy), hydrogen is produced after short-term immersion. This indicates that corrosion of the uncoated substrate starts immediately after its immersion in Hanks' solution.

The ratio τ was found to increase sharply with time, according to a power function, black curve in Fig. 8.10 (a). In contrast, for the substrate coated with the chitosan/TiO_2 coating, the volume of released hydrogen was measured after 45 hours of immersion. This shows that the coating protects the substrate against corrosion after short-term immersion. From 45 hours of immersion, the ratio τ increases slowly and linearly vs. time (red curve in Fig. 8.10 (a)). It can be seen that the value of τ after 160 hours of immersion is 4 times greater in the absence of coating. This result shows clearly that the presence of the chitosan/TiO_2 coating has a beneficial influence on the corrosion resistance of the magnesium alloy.

Knowing the volume of hydrogen released during the corrosion test, the mass of dissolved magnesium was calculated and then the corrosion rate was calculated from equation (6.5), Chapter VI. Fig. 8.10 (b) shows the evolution of the corrosion rate vs. time for the coated and uncoated Mg19Zn1Ca alloy. In the case of the uncoated specimen, the corrosion rate sharply increases with immersion time. Whereas, for long immersion times (greater than 45 hours), the corrosion rate of the covered sample increases slowly vs. time, Fig.8.10 (b). After 157 hours of immersion of the two specimens in Hanks' solution, the corrosion rate was 12.6 and 3.5 mm/y for uncoated and coated substrates, respectively. This result indicates that the chitosan/TiO_2 coating significantly decreases the corrosion rate of the Mg19Zn1Ca alloy.

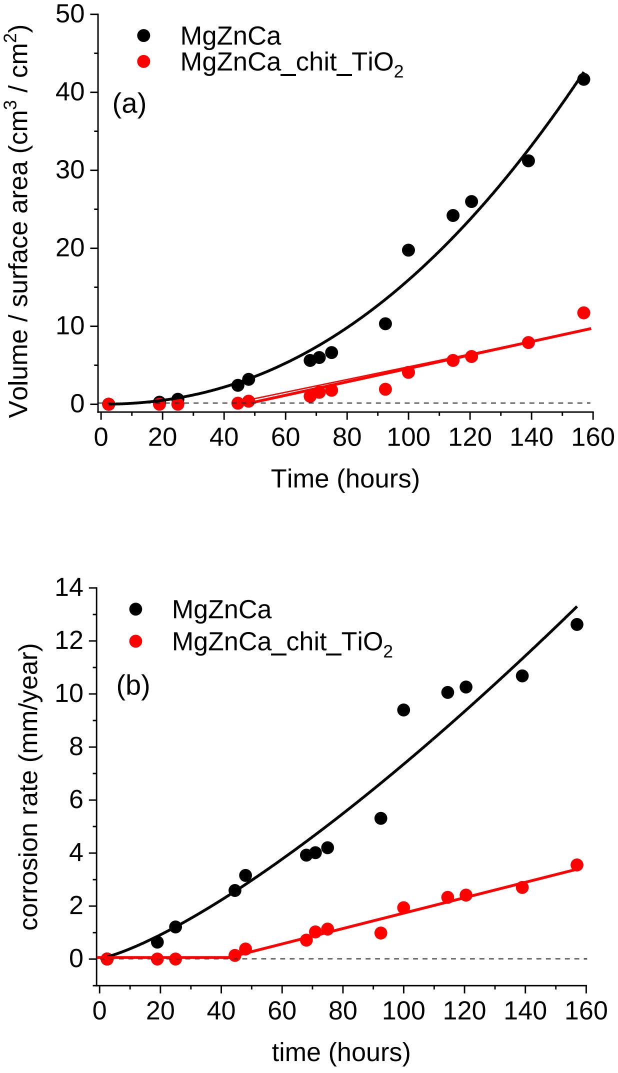

Fig.8.10. Evolution vs time of (a) the ratio between the volume of released hydrogen and sample surface area and (b) the corrosion rate for the uncoated and coated specimens immersed at the OCP in Hanks' solution at 37 °C (a) [211].

8.3. Characteristics of corrosion products

8.3.1. Corrosion products of uncoated and coated Mg20Zn alloy

The corrosion products formed at the surface of bare Mg20Zn and Mg20Zn coated with the chitosan_WG coating were investigated after 110 hours of immersion in Hanks' solution. Figure 8.11 (a, b) shows the surface of the Mg20Zn substrate after immersion for 110 h in Hanks' solution. The bare Mg20Zn alloy undergoes oxidation, and uneven distribution of corrosion products is visible, Fig. 8.11. (a). In general, the corrosion products are formed in the matrix, whereas the intermetallic phase $Mg_{51}Zn_{20}$ does not undergo corrosion. The chemical composition of corrosion products was determined by means of EDS analysis at numerous sites. EDS analysis revealed the presence of few at.% of carbon, about 60 at.% of oxygen, 11.0 ± 0.9 at.% of phosphorous, 8.5 ± 0.7 at.% of magnesium, 8.0 ± 1.3 at.% of calcium, and 1.3 ± 0.1 at.% of sodium. Magnesium comes from the substrate whereas all the other elements come from Hanks' solution. It should be emphasized that zinc, which is mainly present in the intermetallic phase, was not detected in the corrosion products. This suggests that the intermetallic phase does not undergo corrosion.

A top view of the corrosion products formed on the coated specimen (Ca/P_chitosan_WG) is shown in Fig. 8.11 (c, d). EDS analysis revealed that the corrosion products formed on the coated specimen (Ca/P_chitosan_WG) contain a few at.% of carbon, about 60 at.% of oxygen, 8.0 ± 2.0 at.% of phosphorous, 11.5 ± 0.6 at.% of magnesium, and 6.0 ± 2.0 at.% of calcium, 1.1 ± 0.2 at.% of sodium. There is a difference in the chemical composition of the intermetallic phase $Mg_{51}Zn_{20}$ after corrosion for uncoated and coated specimens. On the surface of the intermetallic phase, neither phosphorus nor calcium was found for the coated specimen.

Figure 8.12 shows the FTIR spectra of the uncoated and coated Mg20Zn substrate after immersion in Hanks' solution for 110 h. The main absorption bands at 560 cm^{-1} and 1040 cm^{-1} are attributed to PO_4^{3-}, which confirms the formation of a calcium phosphate layer for both coated and uncoated (Ca-P/chitosan_WG coating) specimens. In the spectrum obtained on the coated specimen (blue curve, Figure 8.12), the broad band in the range 3700–2500 cm^{-1} is due to the overlapping of several bands, i.e., the stretching vibration of O-H, absorbed H_2O and N–H stretching of the amine group, while the vibration bands of the C–H are at ~2920 cm^{-1} and ~2875 cm^{-1}. The peak at ~1645 cm^{-1} is assigned to the N–H bending mode of the amine group and bending mode of H_2O. The band at ~1040 cm^{-1} represents the C–O vibrations in the chitosan molecule [241-243].

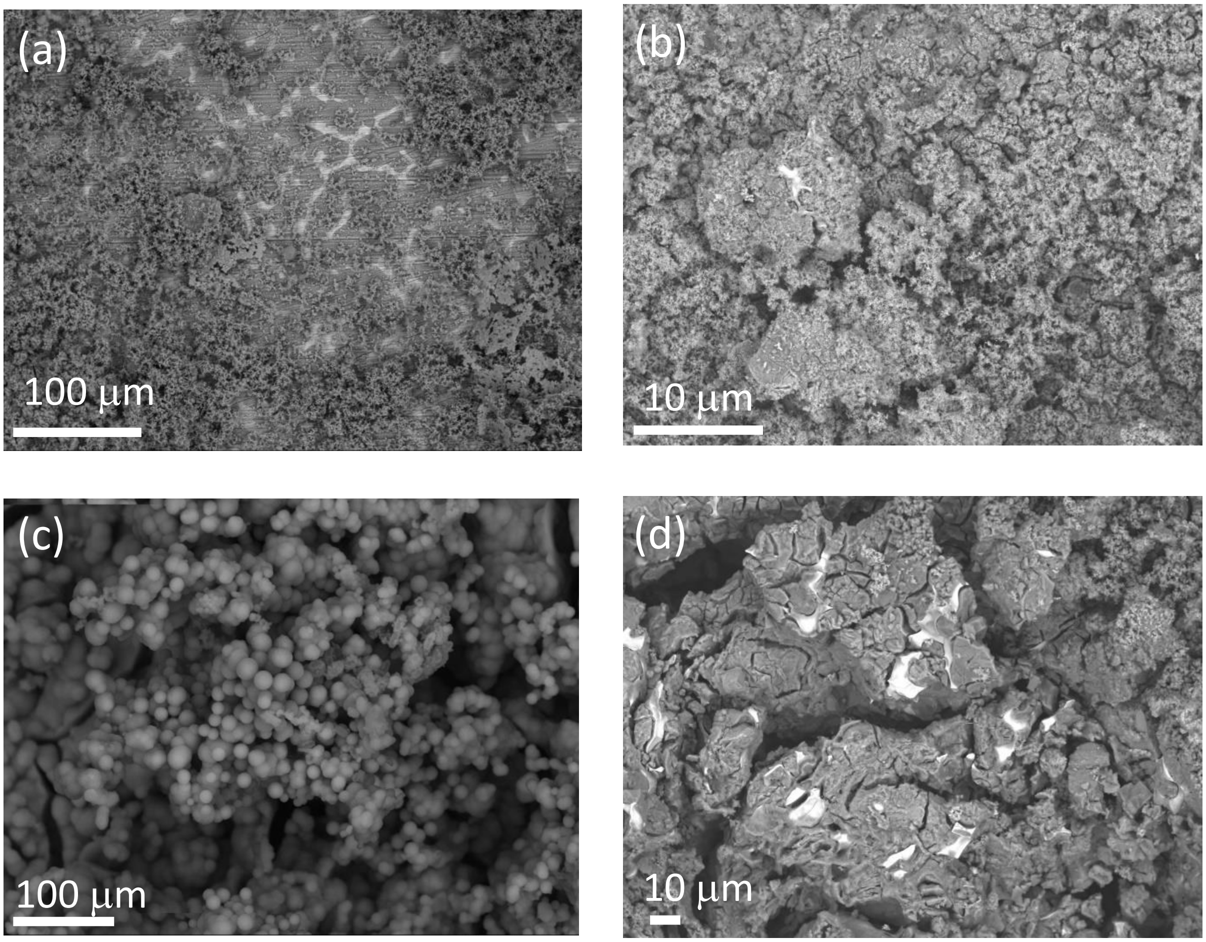

Fig.8.11. SEM image of Mg20Zn alloy (a, b) and Mg20Zn_CaP_chitosan_WG coating (c, d) after exposition for 110 hours in Hanks' solution [210].

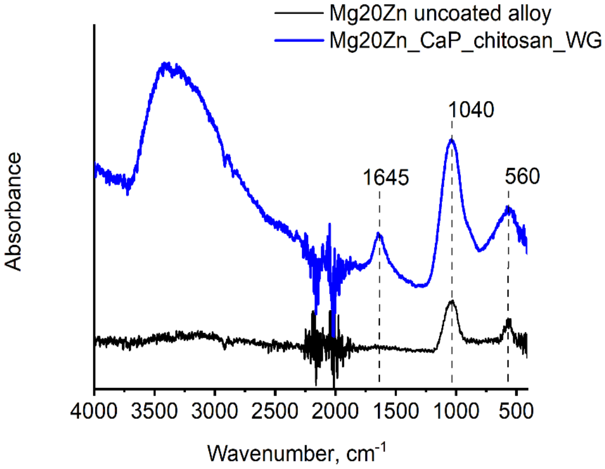

Fig.8.12. FTIR spectra of the Mg20Zn alloy (black curve) and the Ca-P/chitosan_WG coating (blue curve) after immersion in Hanks' solution for 110 h [210].

8.3.2. Corrosion products formed on a coated Mg19Zn1Ca alloy

Figure 8.13 shows the surface morphology of the Mg19Zn1Ca alloy which was coated with the chitosan/TiO_2 coating and then immersed in Hanks' solution for 24 hours and 4 days, respectively. After 24 hours immersion in Hanks' solution, some small micro cracks are visible on the surface of the chitosan/TiO_2 coated Mg19Zn1Ca alloy, Fig. 8.13 (a). However, after a longer immersion time, numerous and wide micro-cracks appear on the surface of the Mg19Zn1Ca alloy covered with the chitosan/TiO_2 coating, Fig. 8.13. (b). Wide micro-cracks are caused by the presence of internal stresses in the layer of corrosion products that grows over time.

EDS analysis performed after exposition of the specimen in Hanks' solution for 24 hours revealed the presence of the following elements: carbon (7.2 at.%), nitrogen (13 at.%), oxygen (55 at.%), magnesium (12.5 at.%), phosphorous (5.0 at.%), chloride (1.5 at.%), calcium (1.3 at.%), titanium (2.5 at.%), and traces of zinc (below 1 at.%). The presence of nitrogen, carbon and titanium confirms that the chitosan/TiO_2 coating was not destroyed. It is still present on the substrate surface. As shown in Figure 8.10, after 24 hours of immersion in Hank's solution, there is no hydrogen evolution on the coated Mg19Zn1Ca alloy, and the corrosion rate is equal to 0 mm/year.

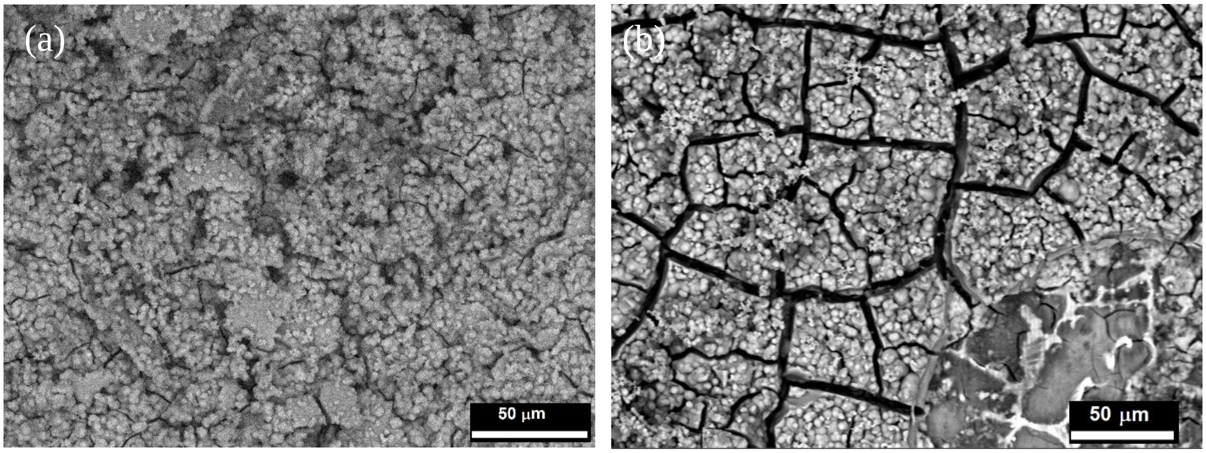

Fig. 8.13. SEM image of the coated Mg19Zn1Ca alloy after immersion for 24 hours (a) and 4 days (b) in Hanks' solution [211].

SEM/EDS analyses performed on the coated Mg19Zn1Ca specimen exposed for 4 days in the corrosive environment reveal the presence of a few at% of carbon, oxygen (about 65 at.%), magnesium (4.3 at.%), phosphorus (10.0 at.%), and calcium (12.0 at.%). The absence of nitrogen and titanium indicates that the coating was destroyed. The large amount of phosphorus and calcium compared to those found on the sample immersed for 24 hours indicates that a layer of corrosion products was formed on the specimen surface. Moreover, the presence of cracks in the corrosion products is caused by the presence of high levels of internal stress, and additionally in some places the coating was partly removed Fig. 8.13 (b).

The chemical composition of corrosion products formed after 4-day immersion of the coated sample was studied by means of XPS. After the corrosion test, the following elements were detected: 20.7 at.% of carbon, 53.8 at.% of oxygen, 8.0 at.% of magnesium, 9.3 at.% of calcium and 7.0 at.% of phosphorus. Fig.8.14 shows the XPS spectra recorded in the individual bands C1s, O1s, Mg2p, Ca2p, P2p. The peak related to the C1s level was fitted considering four components as shown in Fig. 8.14 (a). The components located at 284.5 eV, 286.0 eV, 287.5 eV and 289.7 eV are related to C-C/C-H, C-N, C=O, and carbonates, respectively [244-246]. For the O1s spectrum (Fig.8.14 (b)), two main components were observed at 529.8 eV and 531.5 eV which are assigned to oxides and the O-P bond, respectively [247]. The peak associated with the Mg 2p level at the binding energy of 50.25 eV is related to MgO [248]. The P 2p spectrum was fitted with one peak located at the binding energy of 133.0 eV (phosphate species). The Ca 2p spectrum shows one doublet (Ca2p1/2 et 350.8 eV and Ca2p3/2 at 347.3 eV), Fig.8.14 (d). The peak located at the binding energy of 347.3 eV is attributed to calcium carbonate ($CaCO_3$) [247]. Additionally, the peak at the binding energy 289.7 eV located in the C1s spectrum confirms the presence of carbonates in the layer of corrosion products. XPS analysis revealed that the main corrosion products deposited on the surface of the coated Mg19Zn1Ca magnesium alloy are calcium carbonates and magnesium phosphates.

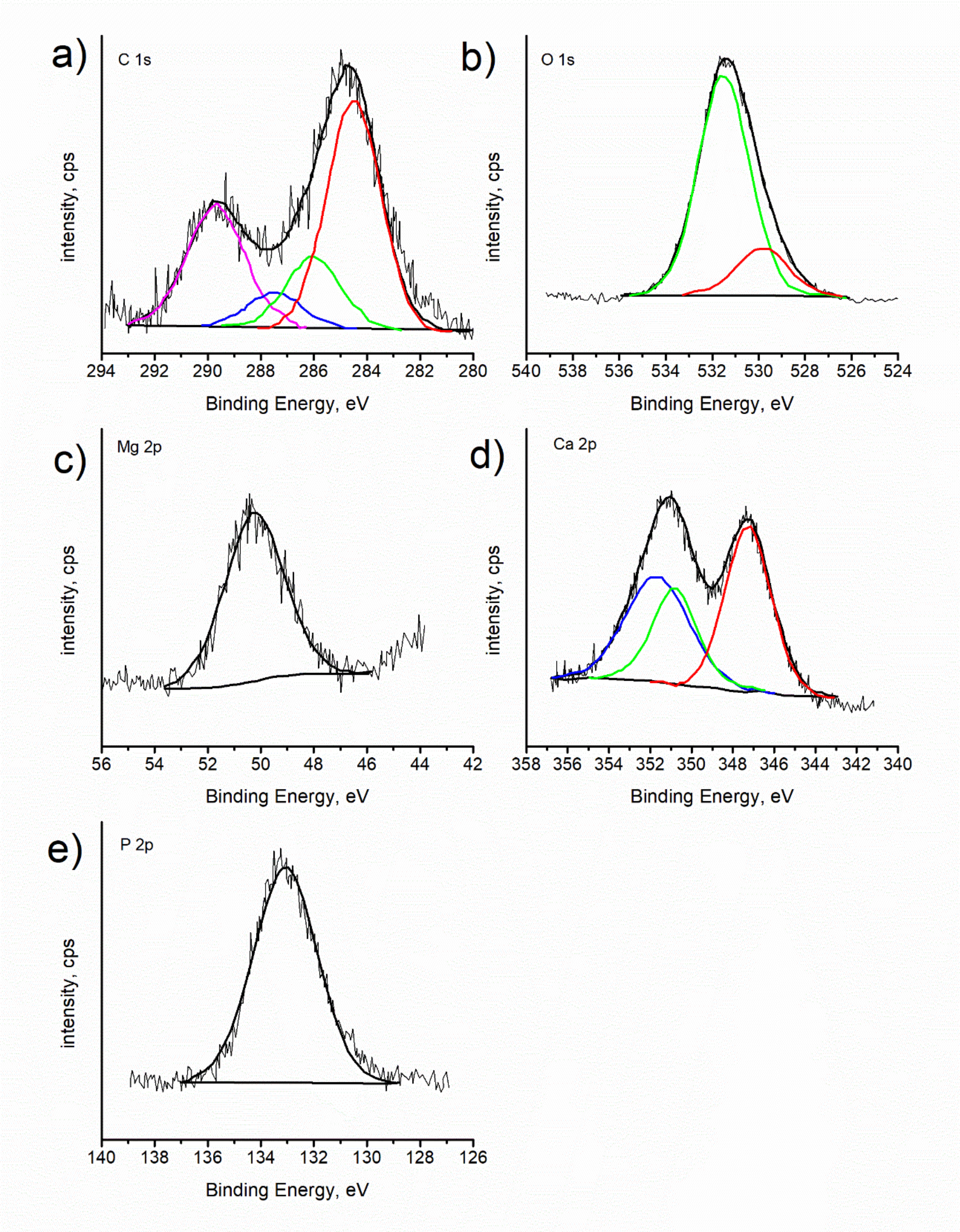

Fig.8.14. XPS spectra recorded for chitosan/TiO_2 coatings deposited on the surface of the Mg19Zn1Ca alloy. XPS deconvoluted profiles for C1s (a), O1s (b), Mg2p (c), Ca2p (d) and P2p (e) [211].

8.4. Corrosion mechanism of coated and uncoated magnesium alloys in Hanks' solution

Corrosion tests revealed that magnesium alloys (binary Mg20Zn and ternary Mg19Zn1Ca) exhibit active electrochemical behavior in Hanks' solution. The corrosion process of magnesium alloys proceeds according to reactions (8.6) – (8.8):

$$Mg \rightarrow Mg^{2+} + 2e \tag{8.6}$$

$$2H_2O + 2e \rightarrow H_2 + 2OH^- \tag{8.7}$$

$$Mg^{2+} + 2OH^- = Mg(OH)_2 \tag{8.8}$$

Magnesium undergoes oxidation (anodic reaction, reaction 8.6) and Mg^{2+} ions go to the solution. At the same time, the cathodic reaction and reduction of water (reaction 8.7) proceeds. Hydroxide ions react with the magnesium cations and the main corrosion product magnesium hydroxide is formed, reaction (8.8). In the case of ternary alloys, the intermetallic phase containing calcium undergoes dissolution and calcium cations are released to the solution, reaction (8.9).

$$Ca \rightarrow Ca^{2+} + 2e \tag{8.9}$$

The corrosion mechanism of magnesium in the solution containing chloride ions is presented in Figure 8.15.

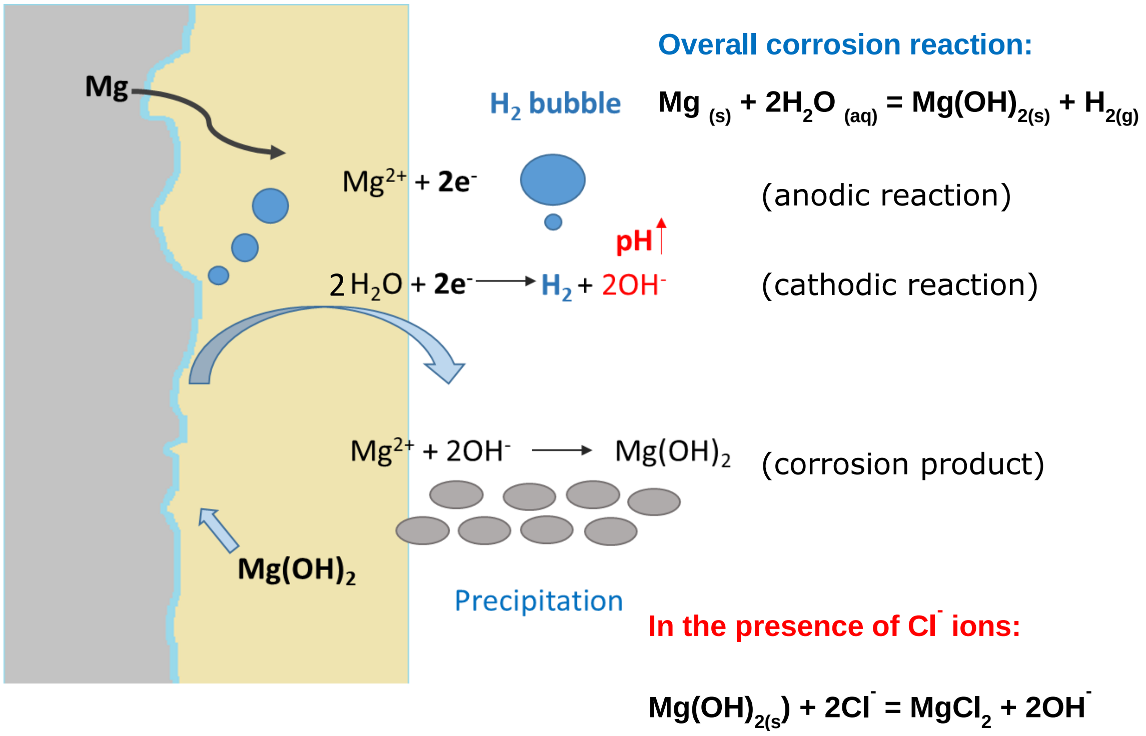

Fig. 8.15. The corrosion mechanism of Mg alloys in the electrolyte containing chloride anions.

In order to slow down the corrosion rate of the magnesium alloy (Mg20Zn), a Ca-P coating was deposited from the solution containing $Ca(NO_3)_2$ and NaH_2PO_4. The PO_4^{3-} ions present in the solution react with calcium ions according to reaction (8.5).

$$Ca^{2+} + PO_4^{3-} \rightarrow Ca_3(PO_4)_2 \tag{8.10}$$

Deposition of insoluble calcium phosphate on the surface of magnesium alloy blocks the penetration of aggressive chloride ions to the metal surface. Therefore, the calcium phosphate layer retards the corrosion rate of the Mg20Zn substrate up to 40 h of immersion in Hanks' solution, orange curve in Figure 8.9. Deposition of the chitosan_WG coating on the bare Mg20Zn alloy decreases the corrosion rate of the substrate for 60 h of immersion in Hanks' solution, blue curve in Figure 8.9. The chitosan_WG solution is an alkaline solution (pH = 11.5) and in contact with the substrate containing magnesium, the following reaction (8.11) proceeds.

$$Mg(OH)_2 + Na_2SiO_3 = MgSiO_3 + 2NaOH \tag{8.11}$$

Magnesium silicate is an insoluble salt which is deposited on the substrate surface and slows down the corrosion rate of the magnesium alloy. As it was shown in Figure 8.9, the presence of two coatings (CaP/chitosan_WG) on the surface of Mg20Zn alloy significantly decreases its corrosion rate in Hanks' solution. The chitosan solution (chitosan_WG) containing water glass and Na_2SiO_3 is alkaline (pH = 11.5). Deposition of such a chitosan_WG solution on the CaP coating causes the formation of insoluble calcium silicate according to reaction (8.12) [210].

$$Ca_3(PO_4)_2 + 3Na_2SiO_3 = 2Na_3PO_4 + 3CaSiO_3 \tag{8.12}$$

The formation of additional compound $CaSiO_3$ insoluble in water causes the formation of a barrier layer and protects the alloy's surface against corrosion. The solubility of $CaSiO_3$ in water is three times lower than the solubility of $Ca_3(PO_4)_2$. Therefore, a synergistic effect due to the presence of the multilayer coating on the corrosion resistance of the Mg20Zn alloy is observed in Hanks' solution. The highest corrosion resistance of the Mg20Zn alloy covered with the CaP/chitosan_WG coating is caused by the formation of two compounds, $CaSiO_3$ and $Ca_3(PO_4)_2$, which are insoluble in water. The beneficial effect of the addition of $CaSiO_3$ on the corrosion resistance of titanium alloy (Ti6Al4V) was presented in the paper [249].

Moreover, it should be emphasized that chitosan is a pH-sensitive polymer. In an acidic solution at pH 5 or lower, the chitosan molecules are protonated. However, in a solution at pH higher than 6, chitosan loses its positive charge and becomes insoluble. In this study, the corrosion test was performed in Hanks' solution at pH = 7.2. During corrosion, OH^- ions are produced and cause the increase of pH, therefore the chitosan exists as deprotonated molecules and cannot attract the negatively charged ions from the solution.

The corrosion of the ternary magnesium alloy in Hanks' solution proceeds according to reactions (8.6-8.9). The overall corrosion reaction of magnesium and its alloys is given by equation (8.4). Moreover, the phosphate ions present in Hanks' solution can react with the magnesium and calcium ions according to reactions (8.13, 8.14).

$$3Mg^{2+} + 2PO_4^{3-} \rightarrow Mg_3(PO_4)_2 \tag{8.13}$$

$$Ca^{2+} + CO_3^{2-} \rightarrow CaCO_3 \tag{8.14}$$

Magnesium phosphate and calcium carbonate undergo deposition at the surface of the magnesium alloy and form a barrier layer. Such a barrier layer (corrosion products) hinders further dissolution of the magnesium alloy. As shown in Figure 8.10 (b) (black curve), the corrosion rate of the uncoated Mg19Zn1Ca alloy varies with exposure time. For immersion times up to 93 hours, the corrosion rate increases linearly with time and the slope of the curve is 0.061. On the other hand, for immersion times longer than 100 hours, the slope of the black curve is 0.052. The decrease in the slope value suggests that corrosion products are deposited on the surface of the magnesium alloy and slow down its corrosion rate.

In the case of the coated specimen, the corrosion rate of the substrate significantly decreased. This was related to the interaction of TiO_2 (NPs) with chitosan molecules. XPS analysis confirmed the presence of Ti-N and Ti-O-N bonds in the coating. In the FTIR spectrum, the characteristic band attributed to the Ti-O-C bending mode was detected. The interaction of the TiO_2 (NPs) caused their uniform distribution in the chitosan matrix. Therefore, a specific chitosan/TiO_2 network was formed, Fig. 8.16.

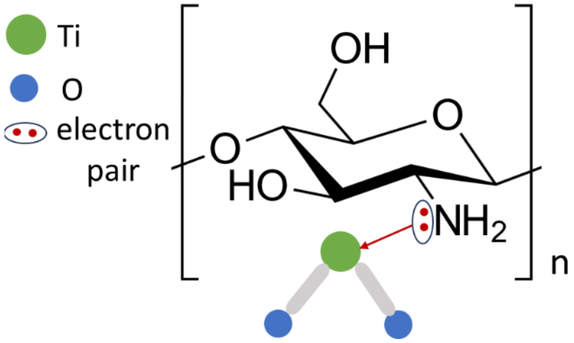

Fig.8.16. The interaction of TiO_2 (NPs) with the chitosan molecule [211].

Such a structure reduced the surface of the magnesium alloy (Mg19Zn1Ca) exposed to Hank's solution and slowed down its corrosion degradation.

Immersion of the Mg19Zn1Ca coated specimen for 4 days in Hanks' solution caused partial damage of the chitosan/TiO_2 coating, and subsequently the corrosion products were deposited at the surface of the bare alloy. XPS analysis showed that there was a significant decrease in carbon (20.7 at.%) after 4 days of exposure in Hanks' solution of the coated alloy compared to the carbon content (56.3 at.%) in the chitosan/TiO_2 coating before the corrosion test. Moreover, the lack of signal in the N1s and Ti2p bands indicates that the chitosan/TiO_2 coating was significantly damaged. The exposed parts of the bare Mg19Zn1Ca alloy undergo corrosion, and deposition of corrosion products occurs. Formation of corrosion products such as calcium carbonates and magnesium phosphates (reactions 8.13, 8.14) were confirmed by XPS analysis on the surface of the coated Mg19Zn1Ca alloy, Figure 8.14.

The corrosion rate of the coated sample varies linearly with time, as shown in Figure 8.10 (b). In contrast to the bare alloy (black curve, Figure 8.10), the slope of the red curve (coated alloy) remains constant over the time range from 40 to 157 hours. The slope calculated for the red curve is 0.027, Figure 8.10 (b). The twice lower value of the slope for the coated alloy compared to the uncoated alloy indicates that the chitosan/TiO_2 coating limits the contact of the substrate with Hank's solution and significantly reduces its corrosion.

8.5. Summary of Chapter VIII

Corrosion tests revealed that the galvanic coupling between the α-Mg matrix and the intermetallic phase $Mg_{51}Zn_{20}$ is a driving force for local corrosion. The corrosion proceeds preferentially in the α-Mg matrix. Coatings like Ca-P, chitosan_WG, and the double layer coating Ca-P/chitosan_WG significantly decrease the corrosion rate of the Mg20Zn alloy in Hanks' solution. The greatest effectiveness in protection against corrosion is achieved by covering the Mg20Zn alloy with a double Ca-P/chitosan_WG coating. The alloy covered with this coating corrodes almost three times slower than the bare Mg20Zn alloy. Moreover, the insoluble corrosion products such as $Ca_3(PO_4)_2$, and $CaSiO_3$ formed at the specimen surface hinder the penetration of chloride ions to the metal surface.

A chitosan/TiO_2 coating was deposited on the Mg19Zn1Ca alloy to protect it against corrosion in Hanks' solution. The bare magnesium alloy (Mg19Zn1Ca) undergoes active corrosion in Hanks' solution. Corrosion products such as magnesium phosphate and calcium carbonate are formed on the surface of Mg alloy, and they retard the initiation of pitting corrosion. The chitosan/TiO_2 coatings enhance the corrosion resistance of the Mg-alloy in Hanks' solution. The interaction of TiO_2 (NPs) with the amine groups present in the chitosan molecule causes their uniform distribution in the chitosan matrix. The formation of such structure means that the chitosan/TiO_2 coating limits the contact of the substrate with Hanks' solution.

Chapter IX

Antibacterial properties of chitosan based-coatings and corrosion resistance

9. Antibacterial properties of chitosan-based coatings

In the literature, it has been shown that antibacterial hydrogels such as chitosan and its derivatives are known as good candidates for several biomedical applications. Chitosan and its derivatives exhibit antibacterial properties [246-249]. Antibacterial hydrogels cross-linked by Ag^+, $Cu^{2+,}$ and Zn^{2+} metal ions exhibit excellent antibacterial properties, especially against *Escherichia coli* and *Staphylococcus aureus*, therefore they can be used for biomedical purposes [250]. Nowadays, numerous investigations are being performed focused on the preparation of more effective derivatives of biocompatible chitosan used for biomedical applications [251]. A derivative of chitosan called methylated 4-N,N dimethyl aminobenzyl N,O-carboxymethyl chitosan (MABCC) was synthesized and its antibacterial activity was tested against four bacterial strains (*Escherichia coli*, *Pseudomonas aeruginosa*, *Staphylococcus aureus* and *Staphylococcus epidermidis*). It was found that MABCC exhibited much greater antibacterial activity than chitosan especially against Gram-positive bacteria [252]. It has been reported [253-254] that Mg alloys coated with chitosan coatings improve not only the corrosion resistance of the alloys, but also their antibacterial properties.

The antibacterial properties of chitosan_WG and chitosan/TiO_2 coatings were investigated. Moreover, additional chitosan-based coatings containing zinc oxide nanoparticles (ZnO(NPs)) and Ag (NPs) were prepared. The ZnO (NPs) and Ag (NPs) were synthesized in an electrochemical way according to the procedures described in the references [208-209]. The antibacterial properties of zinc oxide nanoparticles have been reported in the literature [255-256]. ZnO (NPs) exhibit antimicrobial activity to both Gram-positive bacteria like *Staphylococcus aureus* (S.A.) and Gram-negative bacteria like *Escherichia coli* (E.C). For this reason, ZnO nanoparticles have been incorporated as antibacterial and antifungal agents into surface coatings (paints), textiles, and plastics [257]. It has been shown that nanostructured Ag-ZnO and ZnO/baghdadite coatings deposited on Mg alloy surfaces improved their corrosion resistance and antimicrobial performance toward *Escherichia coli* and *Staphylococcus aureus* compared to bare Mg specimens [258-259]. Silver nanoparticles such as ZnO (NPs) exhibit antibacterial properties; therefore, these nanoparticles are used in the healthcare industries. The addition of up to 3% by weight of silver nanoparticles to chitosan increases its antibacterial properties. When the concentration of Ag (NPs) increases above this threshold, the bactericidal power of chitosan is significantly reduced. Silver nanoparticles react with chitosan particles and produce silver ions, which play a key role in the resistance of the chitosan/Ag(NPs) composite to bacteria [260-261].

9.1. Antibacterial tests

Escherichia coli **(E.C.)** and ***Staphylococcus aureus*** **(S.A.)** are two of the most relevant bacteria that are used to check the antibacterial properties of biomedical materials or drugs. Figure 9.1 shows colonies of *Escherichia coli* and *Staphylococcus aureus* bacteria that were grown under laboratory conditions on agar plates and used to check the antibacterial resistance of chitosan-based coating solutions. For this purpose, two methods were chosen as the most popular methods for testing the antimicrobial properties of substances: the dilution series method and the disk diffusion method.

Figure 9.1. *Staphylococcus aureus* and *Escherichia coli* bacteria colonies.

The **disk diffusion method** is used for routine antimicrobial susceptibility testing. The purpose of the disk diffusion susceptibility test is to determine the sensitivity of bacteria to various antimicrobial compounds like antibiotics, drugs, nanoparticles, or others. The bacteria are grown on Mueller-Hinton agar in the presence of antibacterial-impregnated paper disks. The agar plates are inoculated with a standardized inoculum of the test bacteria. The principles of the disk diffusion method are presented in Figure 9.2. The antibiotic/drug diffuses into the surrounding agar and inhibits the growth of bacteria. Around the antibacterial paper disk (yellow disk), a ring (inhibition zone) is formed, as shown in Figure 9.2. Afterward, the diameters of inhibition zones are measured. The antibacterial potential of tested materials is estimated from the diameter of the inhibition zone [262] or in other words from the ring that has been formed around disks saturated with the antimicrobial material [263].

The rate of diffusion of antimicrobials through the agar is much slower than its extraction out of the disk. Therefore, the concentration of antimicrobials is highest in the close vicinity of the disk [264]. The diffusion rate of antimicrobials in the agar depends on their solubility and molecular weight. Molecules which have a large molecular weight will diffuse more slowly than molecules with a lower molecular weight. These factors cause each antimicrobial to have a unique inhibition zone size indicating its susceptibility to a given antimicrobial compound. The growth inhibition zone depends on the antibiotic (drug) concentration. In some cases, the bacteria can be insensitive to low concentrations of the drug and react only to high concentrations of the drug. In such a case, the inhibition zone will be close to the antibiotic/drug disk. In other cases, if the bacteria are sensitive to low concentrations of the antibiotic, the zone of growth inhibition will be far from the disk.

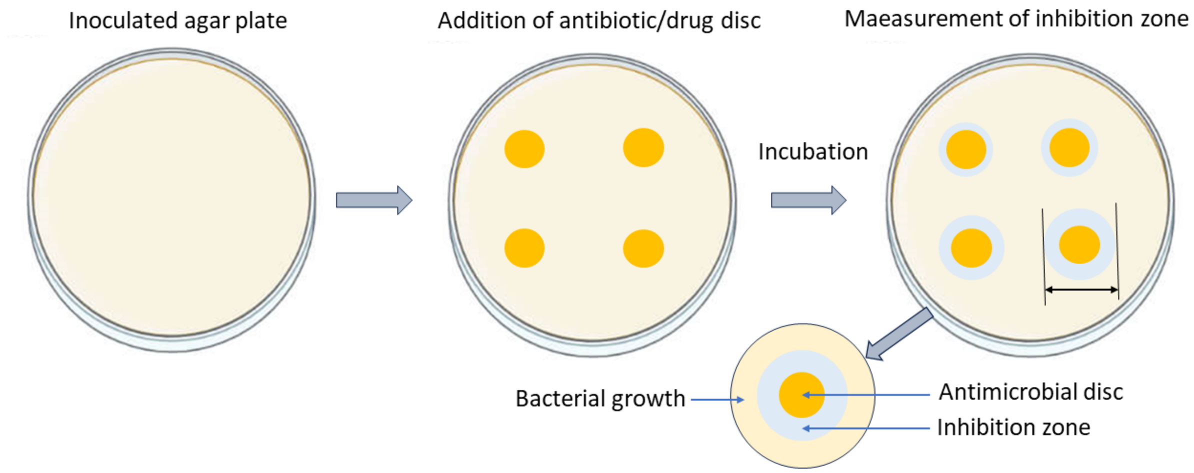

Figure 9.2. Outline of Kirby Bauer Disk Diffusion Method for Antibiotic Susceptibility Testing.

If the bacteria are sensitive to the antimicrobial, their growth is inhibited. Depending on the size of the growth inhibition zone, bacteria are distinguished as:

- sensitive "S" - meaning a high probability of success after using standard doses of the tested antibiotic.
- moderately sensitive "I" – meaning that therapeutic success is not certain. In such a case, a drug can be efficient if it is delivered more frequently or in a higher than standard dose. To increase the chances of the therapeutic success of the drug, the minimum inhibitory

concentration (MIC) should be determined. MIC means the lowest concentration of the antibiotic capable of inhibiting bacterial growth.

- resistant "R" bacteria - meaning that the microorganism is "insensitive" to the action of the tested antibiotic or drug, and therapeutic success is unlikely. These bacteria are resistant even if the dose of the drug used is higher than the standard one.

To investigate the antibacterial properties of chitosan-based coating solutions, Mueller-Hinton agar was chosen as the medium for the disk diffusion method. This medium is widely used to determine the susceptibility of the bacterial isolate to an antibiotic. Mueller Hinton agar has a low content of sulfonamide, trimethoprim, calcium, and magnesium ions, which can interfere with the activity of certain antibiotics. Moreover, this medium is also free of inhibitors that could interfere with bacterial growth. The antibacterial susceptibility of the chitosan-based coatings was tested for two types of bacteria: *Escherichia coli* (E. C.) and *Staphylococcus aureus* (S.A.). 100 mkl *Escherichia coli* and *Staphylococcus aureus* bacteria colonies were prepared at 0.5 McF (0.5 McFarland standard concentration). Sterile filter paper disks were saturated with the tested solutions: chitosan, chitosan/TiO_2, chitosan/ZnO, and chitosan/Ag (NPs). The chitosan-based solutions were placed on the paper disks. Figure 9.3 shows the antibiogram of tested samples for each coating solutions just after sowing of the bacteria. Next, the agar plates were placed in an oven for further incubation of bacteria at a temperature of 36ºC for 24 hours. To obtain reproducible results, 5 agar plates were used for each sample (coating solution).

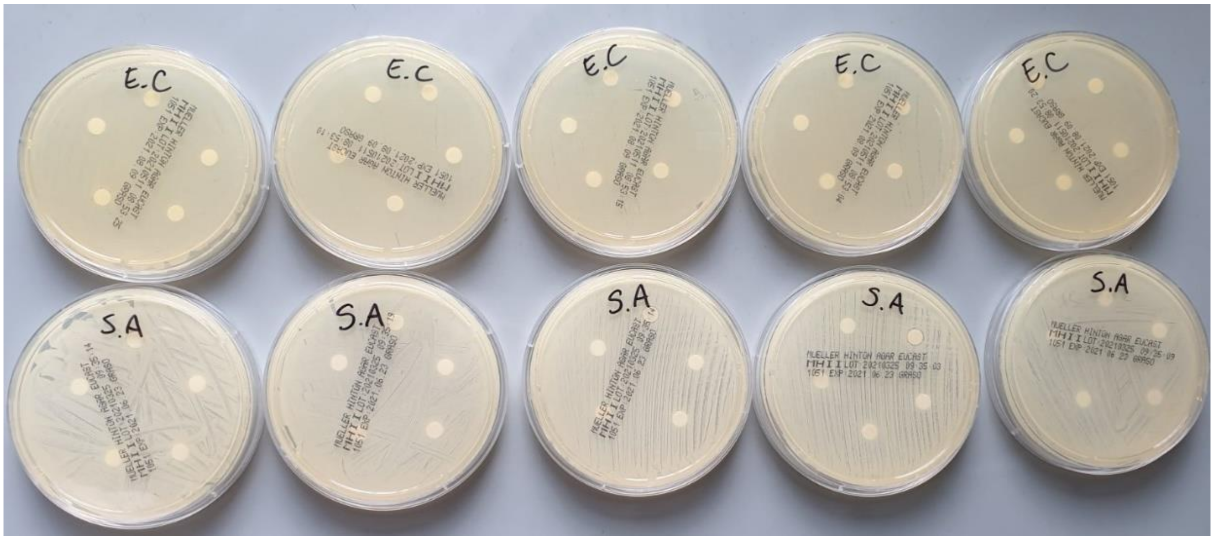

Figure 9.3. Antibiogram of chitosan-based coatings after immersion of tested samples (coating solutions) in *Staphylococcus aureus* and *Escherichia coli* bacteria colonies using the disk diffusion method.

The antibiogram presented in Figure 9.4 shows the zone of inhibition for chitosan-based coatings after exposition for 24 hours at 36°C using the disk diffusion method in *Staphylococcus aureus* and *Escherichia coli* bacteria colonies. In Fig.9.4, “C” means chitosan solution, “Cz” is chitosan with ZnO nanoparticles, “Ct” is chitosan with TiO_2 nanoparticles, and “Ca” is chitosan solution saturated with nanoparticles of Ag. Antibacterial resistance was determined for the samples with chitosan+ZnO (disk “Cz”) and chitosan+Ag (disk “Ca”). The inhibition zone is visible for the chitosan + Ag (NPs) coating solution in the plate with the *Escherichia coli* (E. C.) and *Staphylococcus aureus* (S. A.) bacteria colonies, respectively. The diameter of the inhibition zone (disk “Ca”) is 9mm ± 1mm for *E. coli* bacteria colonies and 8mm ±1mm for *S. aureus* bacteria colonies. The chitosan coating containing the ZnO nanoparticles (disk “Cz”) exhibits a small inhibition zone only in the plates with *Staphylococcus aureus* (S. A.). These results confirm that the chitosan coatings with silver nanoparticles (disk “Ca”) have antibacterial resistance to *Escherichia coli* and *Staphylococcus aureus* bacteria. However, the chitosan coatings containing the ZnO nanoparticles (disk “Cz”) exhibit very weak resistance to *Staphylococcus aureus* (S. A.) bacteria. The inhibition zone is very narrow for disk “Cz” in the plates with *Staphylococcus aureus* (S. A.) bacteria colonies, Figure 9.4.

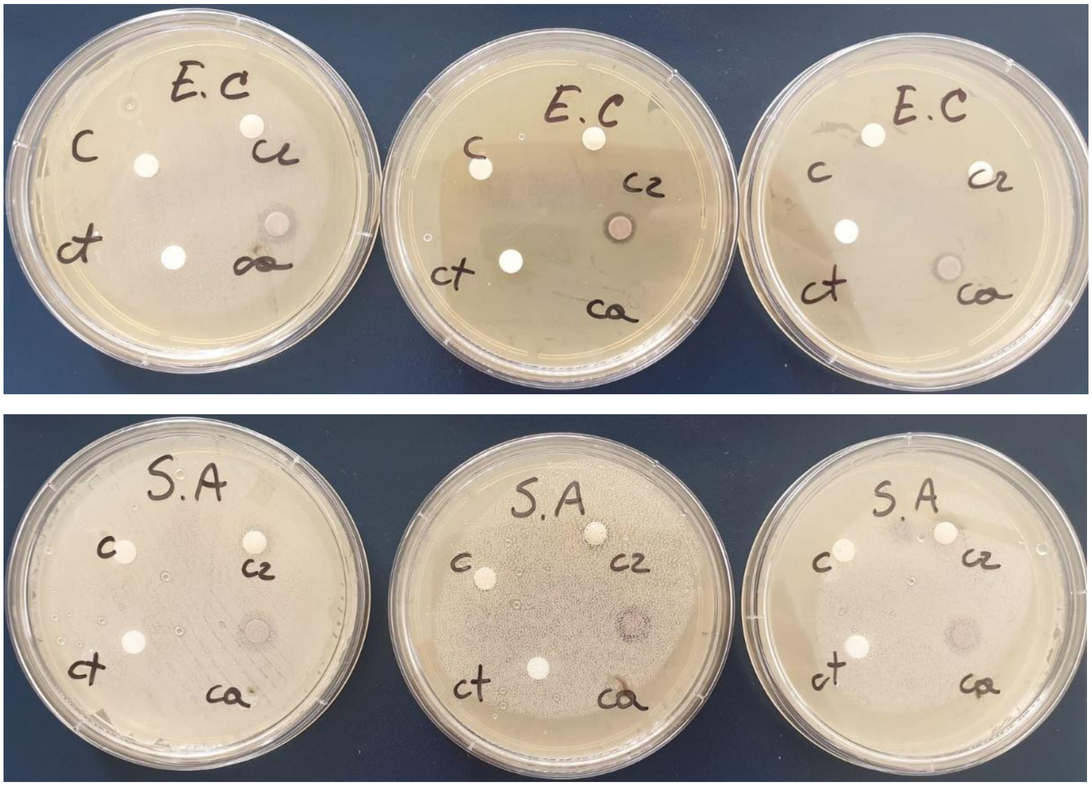

Figure 9.4. Antibiogram of chitosan-based coatings after exposition in oven for 24h at 36°C in *Staphylococcus aureus* and *Escherichia coli* bacteria colonies using the disk diffusion method.

The largest ring around the filter paper disks corresponds to high antibacterial resistance in both bacterial environments. The results presented in Figure 9.4 show that in the ring obtained for the sample with chitosan/ZnO coating solution, the rings around the filter disk are much smaller than in the chitosan/Ag coating. Such a result is correlated with the lower antibacterial resistance of the chitosan/ZnO solution in both bacterial environments. The chitosan/TiO_2 samples do not demonstrate antibacterial protection in either bacterial environment. This could be explained by the low concentration of TiO_2 nanoparticles in the coating solution. Moreover, the chitosan/WG coating solution did not exhibit antibacterial properties in the E.C. or S.A. environments.

Figure 9.5. Equipment used for preparation of dilution series.

The **serial dilution method** allows us to determine the minimum inhibitory concentration (MIC) of the antibiotic/drug capable of inhibiting bacteria growth. MIC is a critical parameter in microbiological analysis, which is based on the calculation of microorganisms present (in this case bacteria) via concentration reduction of a solution containing the drug. Determination of MIC allows the chances of therapeutic success to be increased. To carry out the dilution series test, test tubes with an appropriate medium enabling the growth of bacteria are prepared. Fig. 9.5 shows the equipment used for preparation of the dilution series. The essence of serial dilutions lies in the principle of sequentially reducing the concentration of a solution through fixed dilution factors. In Fig.9.6, the principles of the serial dilution method are presented. This is a methodical process in which a solution is diluted sequentially to produce a series of solutions having progressively lower concentrations. The working solution was the physiological solution (NaCl) with the addition of the tested bacteria (*Escherichia coli* and *Staphylococcus aureus* were each added separately). The working solution for this method was prepared by adding 1 ml of NaCl to the first tube and then immersing in it the stick with the tested bacteria, controlling the concentration of the solution. The second solution was made by the addition of 1 ml of the first solution, mixing and transporting the same amount to the next one. This procedure was repeated until a 10^{-7} dilution was obtained. When the dilution was completed, the prepared agar plates were saturated with the solutions. Figure 9.7 presents the dilution series of bacteria colonies as reference plates. These plates were then placed in the oven and kept for 24 hours at 36ºC. The agar plates with the colonies of bacteria (*Staphylococcus aureus* and *Escherichia coli*) after exposition in the oven are presented in Fig. 9.8.

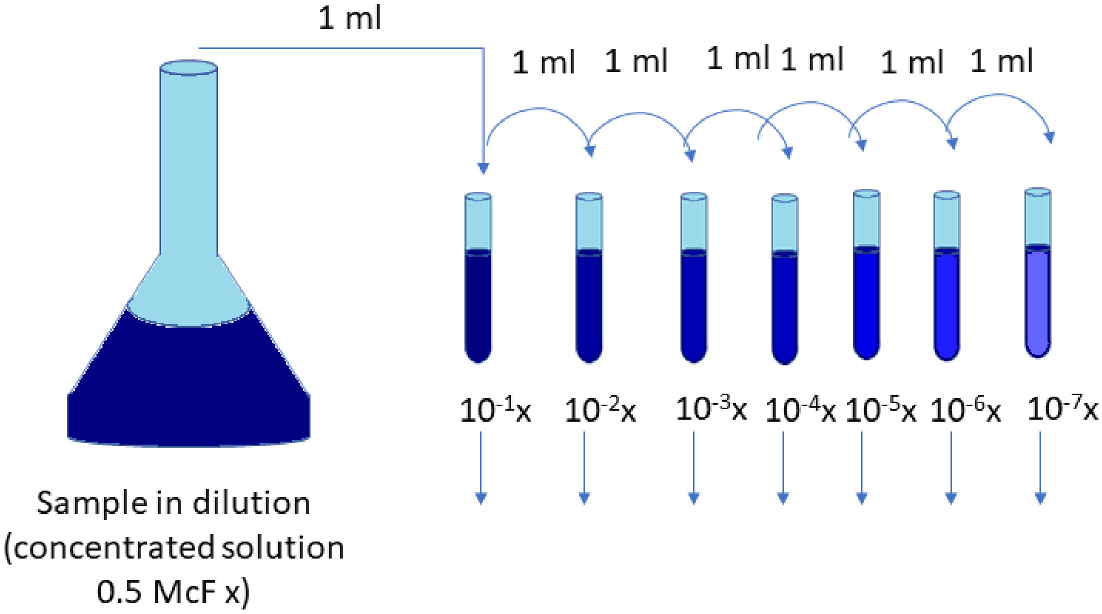

Fig.9.6. Serial dilution process.

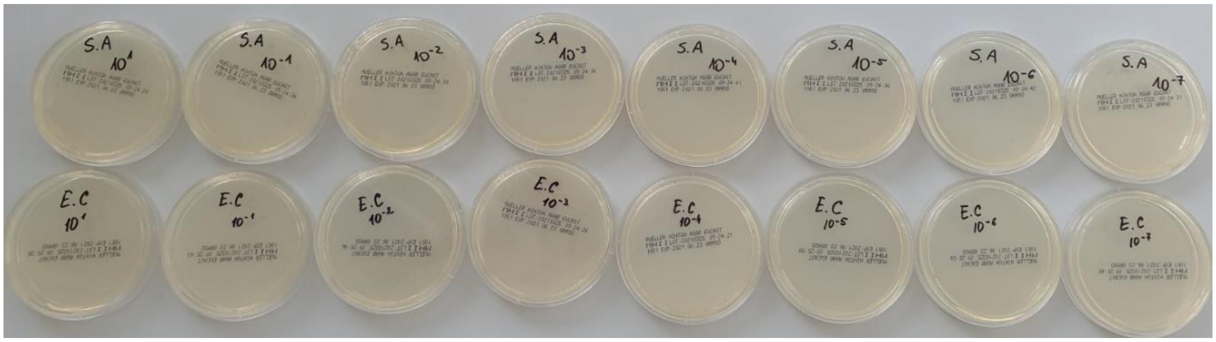

Figure 9.7. Dilution series of bacteria colonies as a reference plates.

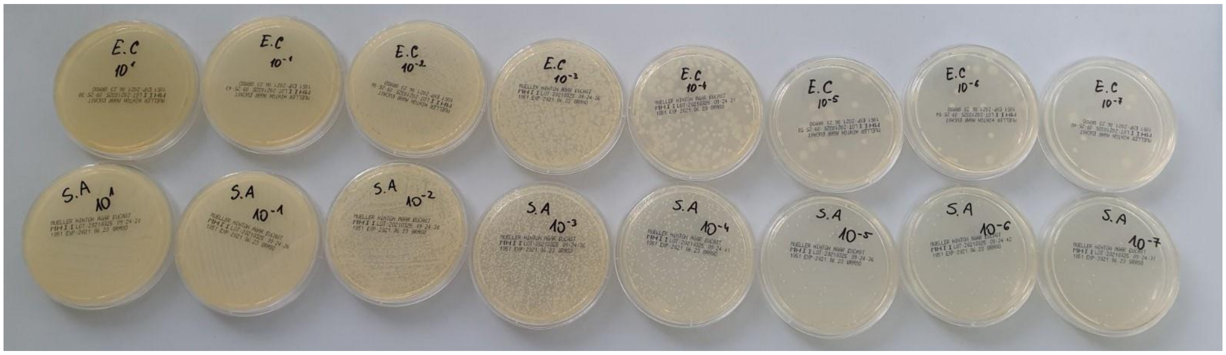

Figure 9.8. Dilution serial of bare agar plates saturated with *Staphylococcus aureus* and *Escherichia coli* bacteria colonies, reference materials after drying in the oven for 24 hours.

To investigate the antibacterial properties of the chitosan coatings, the agar plates were saturated with chitosan-based coating solutions. The following procedure of agar plate preparation was performed: 1) 15 sterile plates were prepared, 2) the agar solution was prepared in a 50 ml flask of distillate water. This solution was heated up to 90ºC to reach complete dissolution of agar in water and to receive a uniform solution, 3) the obtained solution was divided into two flasks with the same volume and after the temperature of the agar solution had decreased to 50ºC, 7.5 ml of chitosan solution was added to the first solution, then the same amount of modified chitosan+Ag solution was added to the second flask. The solutions were mixed and poured out on sterile plates and placed in a fume cupboard for 1 hour for the cooling down and drying process. These operations made it possible to provide serial dilutions for the tested material and study the antibiogram of *Staphylococcus aureus* and *Escherichia coli* bacteria. The inoculation and cultivation of bacteria colonies were performed in the same way as for the reference plates. Fig.9.9 shows a visualization and the calculated result of antibacterial protection of the selected bacteria on the tested solutions. Table 9.1 summarizes the results obtained during the dilution series on the tested samples as well as on bare agar plates as a reference.

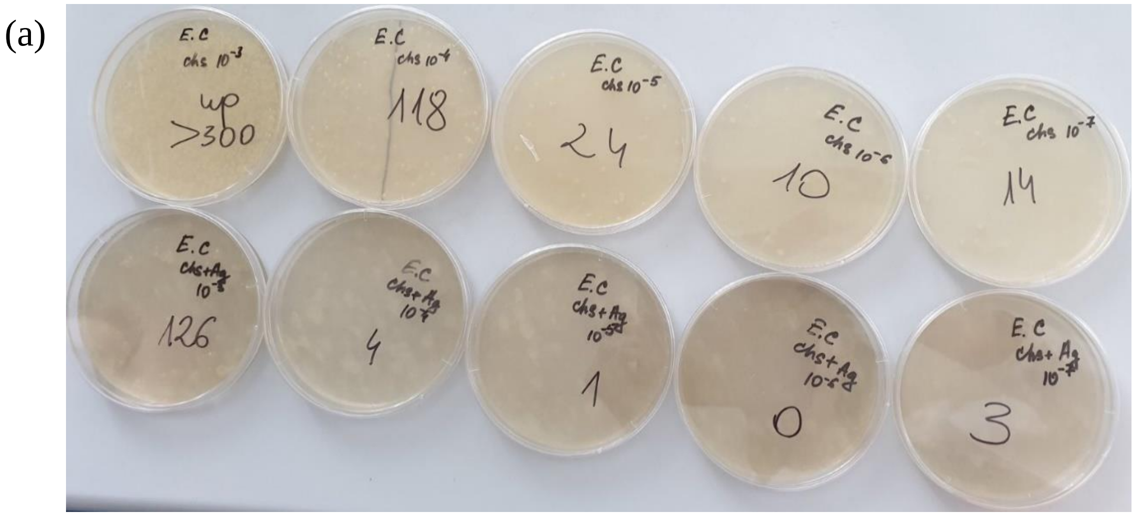

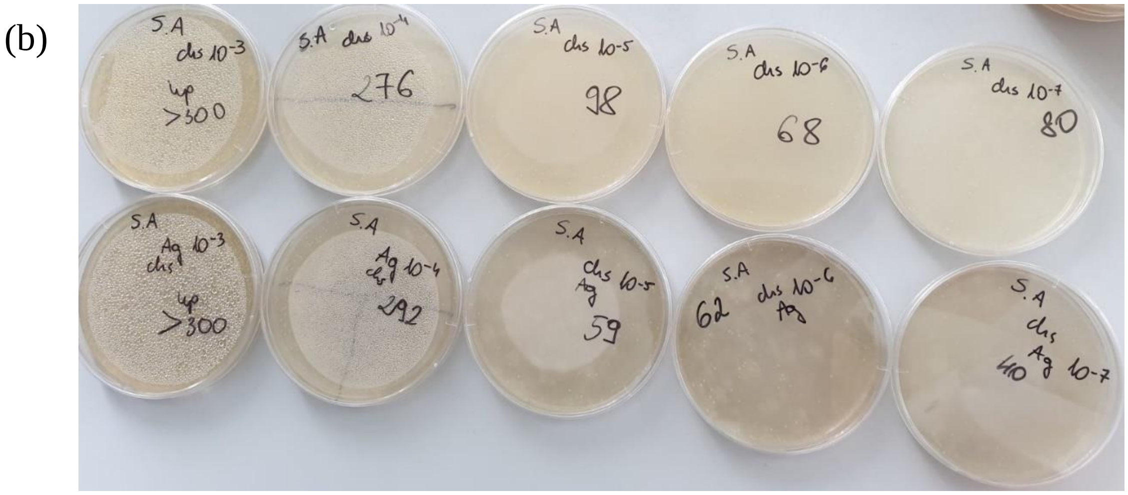

Figure 9.9. Dilution series of tested samples: up row chitosan solution; down row – chitosan+Ag saturated by *Escherichia coli* (a) and *Staphylococcus aureus* (b) bacteria colonies after drying in the oven.

Table 9.1. Comparison of the results obtained after the dilution series method for bacteria colonies protected by chitosan and chitosan+Ag nanoparticle coatings

Reference strain	**Sequential dilutions/sum of colonies on the plate**						
0.5 McF 0.1 ml on the plate	**10^{-1}**	**10^{-2}**	**10^{-3}**	**10^{-4}**	**10^{-5}**	**10^{-6}**	**10^{-7}**
Escherichia coli* *ATCC 25922	› 300	› 300	› 300	136	110	23	7
Chitosan *Escherichia coli*	**› 300**	**› 300**	**› 300**	**118**	**24**	**10**	**14**
Chitosan+Ag nanoparticles *Escherichia coli*	**› 300**	**› 300**	126	4	1	0	3
Staphylococcus aureus* *ATCC 29213	› 300	› 300	› 300	› 300	59	40	37
Chitosan *Staphylococcus aureus*	**› 300**	**› 300**	**› 300**	**276**	**98**	**68**	**80**
Chitosan+Ag nanoparticles *Staphylococcus aureus*	**› 300**	**› 300**	**› 300**	**292**	**59**	**62**	**40**

Summarizing the results obtained, it can be clearly stated that the addition of silver nanoparticles to the chitosan solution increases its antibacterial properties against *Escherichia coli* bacteria. This effect was not present when *Staphylococcus aureus* bacteria were used (Table 9.1).

9.2. Structure of the chitosan coating containing silver nanoparticles

The results of antimicrobial tests showed a relatively poor antibacterial performance of chitosan coatings containing silver and zinc oxide nanoparticles (NPs). Therefore, to explain the reason for this behavior, an analysis of chitosan coatings containing silver and zinc oxide nanoparticles was performed using XPS. These coatings were applied to the surface of the Mg19Zn1Ca alloy. Table 9.2 shows the chemical composition expressed in atomic % of the chitosan coatings. The chitosan + Ag (NPs) coating contains 3.6 at. % of silver, while the chitosan + ZnO (NPs) coating contains 4.4 at. % of zinc. The high content of magnesium (16.6 at. %) and calcium (6.0 at. %) at the surface of chitosan + ZnO coating suggests the dissolution of the Mg19Zn1Ca substrate. Moreover, the significantly lower content of carbon and nitrogen in the chitosan + ZnO coating compared to the chitosan coating with the silver nanoparticles, Table 9.2, suggests the possible interaction of ZnO nanoparticles with the chitosan molecules.

The values of the binding energy of peaks present in the individual bands are presented in Table 9.2. The binding energy of the peaks present in the C1s spectrum are related to the chemical bonds present in the chitosan molecule. Incorporation of silver nanoparticles to the chitosan matrix caused their oxidation to Ag_2O. In the case of the chitosan matrix modified by the addition of ZnO (NPs), only one peak at the binding energy 1021.37 eV in the 2p band was found. This peak is assigned to ZnO nanoparticles. Moreover, the coating (chitosan + ZnO) contained the $Mg(OH)_2$ (binding energy at 1302.6 eV) formed during the dissolution of the substrate.

Table 9.2. Chemical composition (at.%) of chitosan coatings containing Ag (NPs) and ZnO (NPs)

	C	**N**	**O**	**Mg**	**Zn**	**Ca**	**Ag**
Chitosan + Ag (NPs)	60.1	5.0	28.5	2.5	0.2	0.9	3.6
Chitosan + ZnO (NPs)	23.4	1.6	48.0	16.6	4.4	6.0	-

Table 9.3. Binding energy in the individual bands obtained from XPS measurements for chitosan coatings with Ag and ZnO (NPs).

	C1s	**O1s**	**N1s**	**Zn2p**	**Ag3d**	**Ca2p**
Chitosan + Ag (NPs)	284.68 eV 286.15 eV 287.7 eV	529.5 eV 531.12 eV	398.10 eV		366.6 eV	350.21 eV 353.35 eV
Chitosan + ZnO (NPs)	284.53 eV 286.01 eV 287.88 eV 289.2 eV	530.92 eV 532.43 eV	399.04 eV	1021.37 eV	-	350.87 eV 353.51 eV

Figure 9.10. shows the FTIR spectrum of the chitosan + Ag (NPs) (red curve) and chitosan + ZnO (NPs) (blue curve) coatings compared to the chitosan coating without additions (black curve). The main band that appears on all three curves in between the range from 3700 cm^{-1} to 3000 cm^{-1} corresponds to O-H (hydroxyl) and (N-H) amide stretching vibrations indicating the chitosan molecule. The bands at the 2930 cm^{-1} and 2875 cm^{-1} regions correlated with C-H bonds –CH_2, -CH_3 respectively. The band at 1560 cm^{-1} was assigned to the amide N-H group [168]. Moreover, the bands at the 1376 cm^{-1} and 1061 cm^{-1} regions were assigned to C-O stretching vibrations of the carbonyl group. Until that step, the spectrums for all three tested samples corresponded to the chitosan molecule. In the case of chitosan + Ag (NPs) (red curve), all the peaks were more intensive than in other cases. A hump at 1640 cm−1 appears in the band between 1700 cm−1 and 1500 cm−1, and it originates from the bending and stretching modes of the OH groups. The band at the 590 cm-1 region could be attributed to C–Cl stretching, which is characteristic of alkyl halides. This could be explained by the interaction with Ag^{+} ions or nanoparticles [265].

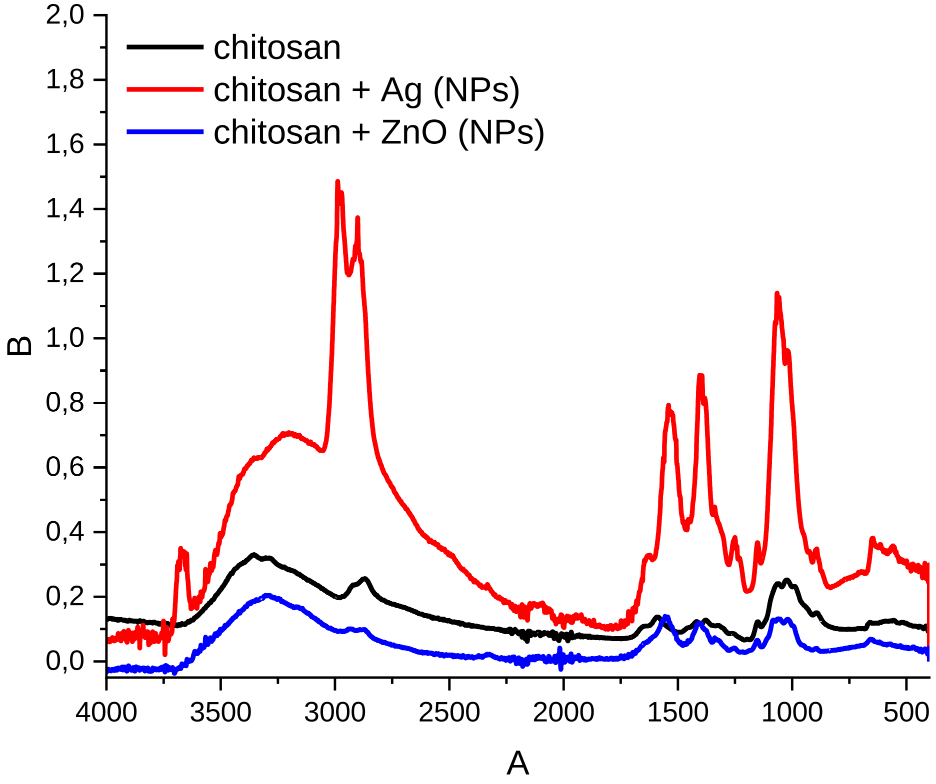

Fig.9.10. FTIR spectra measured for chitosan + Ag (NPs) and chitosan + ZnO (NPs) coatings.

9.3. Corrosion behavior of Mg19Zn1Ca alloy coated by antibacterial coatings.

In Figure 9.11, a comparison of LSV curves obtained for uncoated and coated Mg19Zn1Ca alloy is presented. The current density in the anodic branch of the Mg19Zn1Ca bare alloy increases sharply with increasing applied potential, exhibiting active behavior. In the case of the coated samples, the current density in the anodic branch increases significantly, but the values are lower than those obtained on the Mg19Zn1Ca substrate. These results show that the presence of these coatings slows down the anodic reaction and has a beneficial influence on the corrosion resistance of the Mg19Zn1Ca alloy. We can see that the chitosan and the chitosan+ZnO coatings perform slightly better than the chitosan+Ag coating. It should be noted that the lowest values of anodic current density are shown by the alloy coated only with a chitosan coating.

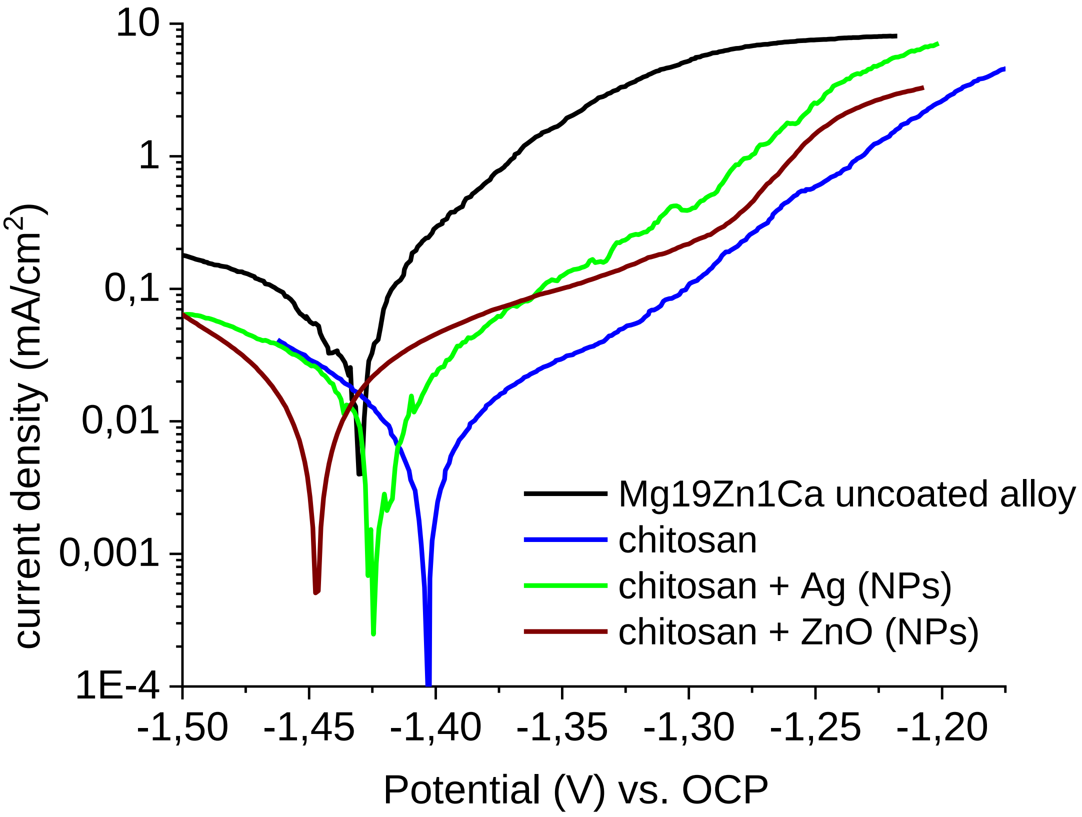

Figure 9.11. Comparison of polarization curves between bare MgZnCa alloy and coated samples in Hanks' solution.

From the polarization curves, the values of corrosion current and corrosion potential were determined for uncoated and chitosan-coated magnesium alloy. The values of corrosion current were determined as: 70 µA/cm^2, 20 µA/cm^2, 14 µA/cm^2, 7 µA/cm^2 for bare Mg19Zn1Ca alloy, magnesium alloy coated by chitosan +Ag (NPs), chitosan+ZnO (NPs), and chitosan coatings, respectively. Meanwhile, the values of corrosion potential were: -1.433 V, -1.417 V, -1.449 V, -1.403 V for bare Mg19Zn1Ca alloy, magnesium alloy coated by chitosan +Ag (NPs), chitosan+ZnO (NPs), and chitosan coatings, respectively. The lowest values of corrosion current density and the highest for corrosion potential were obtained for the Mg19Zn1Ca alloy covered by the chitosan coating. This result suggests that the magnesium alloy coated by the chitosan coating has the best corrosion resistance. The addition of Ag and ZnO NPs to chitosan matrix slightly enhance the corrosion activity of the Mg19Zn1Ca alloy in Hanks' solution. As expected, the most active corrosive behavior is exhibited by the uncoated alloy (bare Mg19Zn1Ca alloy).

Electrochemical impedance spectroscopy (EIS) was used to investigate the mechanisms of corrosion of MgZnCa coated by the chitosan/Ag (NPs) coating. Fig.9.12 shows the EIS spectra for the coated MgZnCa alloy immersed in Hanks' solution for 2 and 7 hours. These spectra were fitted using the electrical equivalent circuit presented in Fig. 9.13. Rs stands for the solution resistance, Rct is the charge transfer resistance, L is inductance, and R_L is inductance resistance. CPE is the constant phase element (corresponding to the formation of oxides at the interface solution/surface of electrode) The constant phase element (CPE) is used to simulate the capacitive response of a non-ideal capacitor, due to the heterogeneous nature of the electrode surface. The equation which represents the impedance of the constant phase element (CPE) is described in Chapter VIII. The values of the parameters obtained after fitting the electrical equivalent circuit are presented in Table 9.4. The EIS spectra show a capacitive reactance arc in the high frequency region and an inductive reactance arc in the low frequency region, Fig.9.12. An increase of the charge transfer resistance (Rct) and the inductance resistance (R_L) is observed with increasing immersion time by a factor of 2.6 and 4.5, respectively.

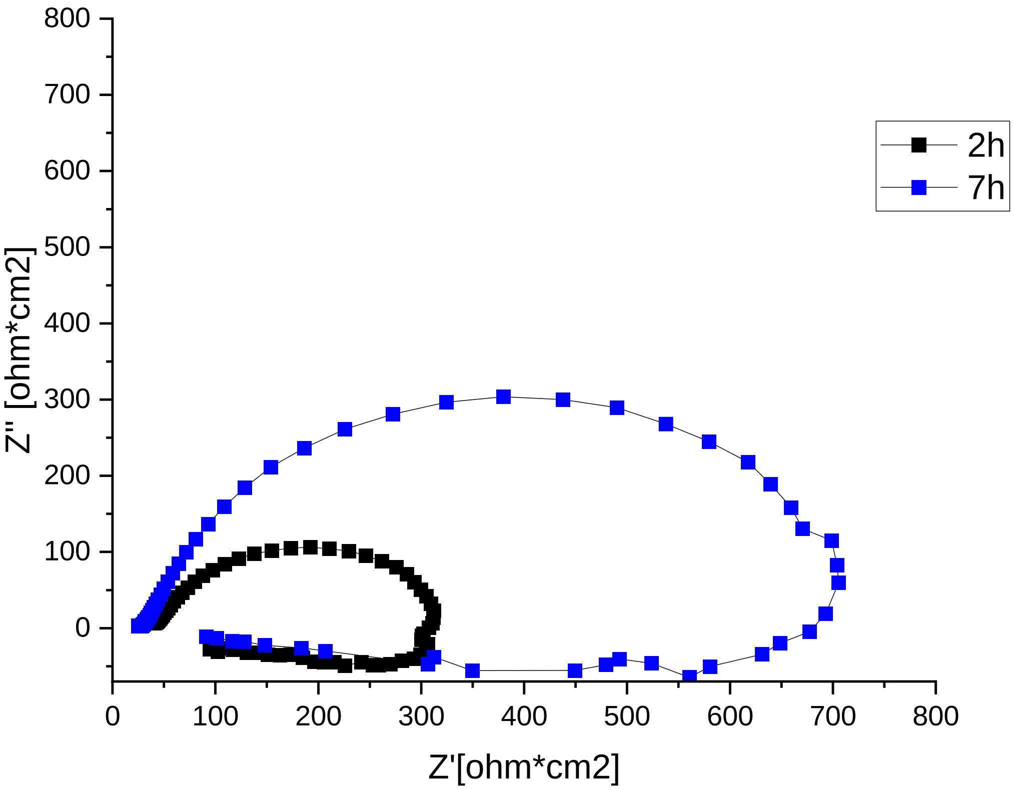

Figure 9.12. EIS spectra obtained after exposition of MgZnCa alloy coated by chitosan/Ag (NPs) in Hanks' solution for 2 hours and 7 hours, respectively.

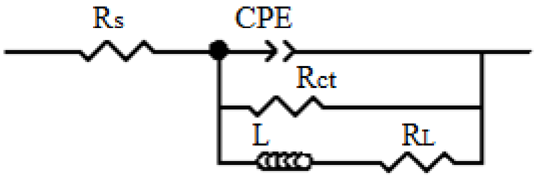

Figure 9.13. The electrical equivalent circuit used for fitting the experimental spectra.

Table 9.4. The values of fitting parameters obtained from the EIS spectra of MgZnCa coated by chitosan/Ag (NPs).

Immersion time	**R_s (Ω·cm^2)**	**R_{ct} (Ω·cm^2)**	**Y (S·cm^{-2}·s^n)**	**n**	**R_L (Ω·cm^2)**	**L (H·cm^2)**
2 hours	40.8	268.0	$4.6 \cdot 10^{-5}$	0.8	165.3	1117.0
7 hours	28.7	704	$1.1 \cdot 10^{-4}$	0.8	741.0	2229

The presence of an inductive loop indicate that the corrosion products undergo adsorption on the surface of the coated MgZnCa alloy. The adsorption of corrosion products on the specimen surface can slow down the dissolution of the substrate.

Summary of Chapter IX

The anti-antibacterial properties and corrosion resistance of chitosan coatings modified with the addition of silver and ZnO nanopartilces (NPs) was investigated. It was shown that the coating containing silver (NPs) exhibits an antibacterial effect against *Escherichia coli* (E. C.) and *Staphylococcus aureus* (S. A.) bacteria. The chitosan coating containing ZnO (NPs) exhibited very weak antibacterial properties only against the *Staphylococcus aureus* (S. A.) bacteria. The polarization curves obtained for the coated and uncoated specimens showed higher current density in the anodic branch compared to the specimen coated only by the pure chitosan coating. However, the current density in the cathodic and anodic branches and corrosion current for the specimen coated by the chitosan coatings with the silver and zinc oxide nanoparticles were much lower than for the uncoated substrate (Mg19Zn1Ca alloy).

Conclusions

The corrosion mechanism of binary (Mg20Zn) and ternary (Mg19Zn1Ca) magnesium alloys in Hanks' solution was investigated. To enhance the corrosion resistance of magnesium alloys, protective chitosan-based coatings were deposited on their surface. Based on the microstructural, corrosion, and electrochemical tests carried out, the following conclusions were drawn:

1. The addition of Ca to MgZn alloy refines its microstructure. The corrosion of both (Mg20Zn and Mg19Zn1Ca) proceeds preferentially in the α-Mg matrix. The galvanic coupling between the α-Mg matrix and intermetallic phase $Mg_{51}Zn_{20}$ (in the case of binary alloy) and Mg_2Ca, $Ca_2Mg_6Zn_3$ (in the case of ternary alloy) is a driving force for corrosion of Mg20Zn and Mg19Zn1Ca alloys.
2. The intermetallic phases for uncoated and coated magnesium alloys after corrosion tests were not dissolved.
3. Chitosan-based coatings deposited on the surface of magnesium alloys enhance their corrosion resistance in Hanks' solution. Uniform chitosan-based coatings were deposited by using a spin-coater. Spin-coating is the perfect method for deposition of polymeric (chitosan-based) coatings.
4. The best corrosion resistance in Hanks' solution was exhibited by the magnesium alloys coated with a double layer coating Ca-P/chitosan_WG. During the deposition of the Ca-P/ chitosan_WG coating, the insoluble compound $CaSiO_3$ ($CaO \bullet SiO_2$) was formed. Deposition of $CaSiO_3$ on the surface of magnesium alloy impedes the alloy's dissolution. Moreover, during the corrosion test, $Mg(OH)_2$ and $Mg_3(PO_4)_2$, were deposited on the surface of the Mg alloy. These corrosion products formed on the surface of the magnesium alloy form a barrier layer. This layer slows down the further dissolution of the alloy. Corrosion products formed at the surface of uncoated and coated magnesium alloys were porous.
5. Chitosan/TiO_2 coatings deposited on the surface of the Mg19Zn1Ca alloy significantly enhance its corrosion resistance in Hanks' solution. The interaction of TiO_2 nanoparticles with the amine groups present in the chitosan molecules ensures their uniform distribution in the polymer matrix. The chitosan/TiO_2 coating limits the contact of the substrate with Hanks' solution and limits its corrosion.

6. EIS measurements revealed that the corrosion of pure magnesium alloy (Mg19Zn1Ca) proceeds in two steps: dissolution of the matrix and deposition of corrosion products on its surface. During coating degradation, the alloy is dissolved, and corrosion products are deposited on the electrode surface. In contrast, corrosion of the coated alloy occurs through dissolution of the alloy, and diffusion of species involved in the chemical-electrochemical reaction mechanisms from the bulk of the solution to the electrode/solution interface.

7. The antibacterial chitosan coatings containing silver and ZnO nanoparticles (NPs) improved the corrosion resistance of Mg19Zn1Ca alloy in Hanks' solution. The current density in the anodic branch was lower than for bare magnesium alloys. Antibacterial tests revealed that the coating containing silver (NPs) exhibited an antibacterial effect against *Escherichia coli* (E. C.) and *Staphylococcus aureus* (S. A) bacteria. In turn, the chitosan coating containing ZnO (NPs) exhibited very weak antibacterial properties only against the *Staphylococcus aureus* (S. A) bacteria.

8. The antibacterial properties of the chitosan-based coatings can be improved by optimization of concentration of nanoparticles or by addition of other compounds.

References:

1. Kuifeng Bai, et.al, Fabrication of chitosan/magnesium phosphate composite coating and the in vitrodegradation properties of coated magnesium alloy, Materials Letters 73 (2012) pp. 59–61.
2. https://en.wikipedia.org/wiki/Magnesium
3. Jingren Lia, et.al, Microstructure and mechanical property of multi-pass low-strain rolled Mg-Al-Zn-Mn alloy sheet, Journal of Alloys and Compounds (2020), pp. 155228
4. K.U. Kainer, Magnesium and its alloys in technologies, Wiley-VCH, 2003
5. H. Zreiqat, et.al, Mechanisms of magnesium-stimulated adhesion of osteoblastic cells to commonly used orthopaedic implants, Journal of Biomedical Materials Research 62 (2002), pp. 175–184
6. Yu Fan, et.al, Influence of cerium on the microstructure, mechanical properties and corrosion resistance of magnesium alloy, Materials Science and Engineering A 433 (2006) pp. 208–215
7. Y. Huang, et.al, Role of multi-microalloying by rare earth elements in ductilization of magnesium alloys, J. Magnesium Alloys 2 (2014)
8. A. Boby, et.al, Mechanical characterization and corrosion behavior of newly designed Sn and Y added AZ91 alloy, Mater. Des. 88 (2015) 871-879,
9. Hiba Azzeddine, et. al., Impact of rare-earth elements on the corrosion performance of binary magnesium alloys, Journal of Alloys and Compounds 829 (2020) 154569
10. D. Liu, et.al,, Mechanical properties, corrosion resistance and biocompatibilities of degradable Mg-RE alloys: a review, J. Mater. Res. Technol. 8 (2019) 1538-1549
11. E. Willbold, et,al., Effect of the addition of low rare earth elements (lanthanum, neodymium, cerium) on the biodegradation and biocompatibility of magnesium, Acta Biomater. 11 (2015) 554-562
12. W. Liu, et.al., Effect of rare earth element Ce and La on-corrosion behavior of AM60 magnesium alloy, Corrosion Sci. 51 (2009) pp. 1334-1343
13. Z. Shi, et.al., Corrosion behaviour in salt spray and in 3.5% NaCl solution saturated with Mg(OH)2 of as-cast and solution heat-treated binary MgeRE alloys: RE¼Ce, La, Nd, Y, Gd, Corrosion Science. 76 (2013) 98-118
14. J. Chang, et.al, Investigation of the corrosion for MgexGde3Ye0.4Zr (x¼6,8,10,12wt%) alloys in a peak-aged condition, Corrosion Science. 50 (2008) 166 - 177
15. Lei Zhang, et.al., Advances in microarc oxidation coated AZ31 Mg alloys for biomedical applications, Corrosion Science 91 (2015) pp. 7-28
16. Institute of Medicine (IOM). Food and Nutrition Board. Dietary Reference Intakes: Calcium, Phosphorus, Magnesium, Vitamin D and Fluoride. Washington, DC: National Academy Press, 1997.
17. Oriane Baulin, et.al., A new, toxic element-free Mg-based metallic glass for biomedical applications, Journal of Non-Crystalline Solids Volume 481, (2018), pp. 397-402
18. J. Degner, et.al, Electrochemical investigations of magnesium in DMEM with biodegradable polycaprolactone coating as corrosion barrier, Appl. Surf. Sci. 282 (2013) 264–270.
19. G.E.J. Poinern, et.al, Biomedical Magnesium Alloys: A Review of Material Properties, Surface Modifications and Potential as a Biodegradable Orthopaedic Implant, Am. J. Biomed. Eng. 2 (2013) 218–240

20. S. Heise, et.al, Tackling Mg alloy corrosion by natural polymer coatings - A review, J. Biomed. Mater. Res. Part A. 104 (2016) 2628– 2641.
21. J.E. Gray, B. Luan, Protective coatings on magnesium and its alloys — a critical review, J. Alloys Compd. 336 (2002) 88–113
22. F. Witte, et.al, Degradable biomaterials based on magnesium corrosion, Curr. Opin. Solid State Mater. Sci. 12 (2008) 63–72.
23. S. Virtanen, Biodegradable Mg and Mg alloys: Corrosion and biocompatibility, Mater. Sci. Eng. B Solid-State Mater. Adv. Technol. 176 (2011) 1600–1608.
24. J.V. Rau, et.al., Glass-ceramic coated Mg-Ca alloys for biomedical implant applications, Materials Science and Engineering C-64 (2016) 362-369
25. F. Witte, et.al, In vitro and in vivo corrosion measurements of magnesium alloys Windhagen Biomaterials, 27 (2006), pp. 1013-1018
26. Shi Jin, et.al, Mechanical properties, biodegradability and cytocompatibility of biodegradable Mg-Zn-Zr-Nd/Y alloys, Journal of Materials Science & Technology Volume 47, 15 June 2020, Pages 190-2
27. Yufeng Zheng, Magnesium alloys as degradable biomaterials, CRC Press 2016
28. Y. Chen, et.al., Recent advances on the development of magnesium alloys for biodegradable implants Acta Biomater., 10 (2014), pp. 4561-4573
29. S. E. Harandi, et.al, Effect of forging process on microstructure, mechanical and corrosion properties of biodegradable Mg-1Ca alloy, Materials and Design 23 (5) (2011) 2596-2603
30. Chaoyong Zhao, et.al, Preparation and characterization of as-extruded Mg-Sn alloys for orthopedic Applications, Materials and Design, (2015), pp. 60-67
31. Erlin Zhang, et.al, Microstructure, mechanical properties and bio-corrosion properties of Mg–Si(–Ca, Zn) alloy for biomedical application. Acta Biomaterialia, (2010), pp. 1756-1762
32. Erlin Zhang, et.al, Microstructure, mechanical properties and bio-corrosion properties of Mg–Si(–Ca, Zn) alloy for biomedical application, Acta Biomaterialia, 6 (2010) 1756-1762
33. H.F. Li, et.al, Development of biodegradable Zn-1X binary alloys with nutrient alloying elements Mg, Ca and Sr Sci. Rep., 5 (2015), pp.1-13
34. Yang Min, et.al, Microstructure and Properties of Mg-3Zn- 0.2Ca Alloy for Biomedical Application, Rare Metal Materials and Engineering 47 (2018) Online English edition of the Chinese language journal
35. Lichen Zhao, et.al, Mechanical properties and in vitro biodegradation of newly developed porous Zn scaffolds for biomedical applications, Materials & Design Volume 108, 15 October 2016, Pages 136-144
36. Da-peng ZHAO, et.al, Effects of Sr incorporation on surface structure and corrosion resistance of hydroxyapatite coated Mg−4Zn alloy for biomedical applications, Trans. Nonferrous Met. Soc. China 28(2018) 1563−1570
37. Mingbo Yang,Fusheng Pan, Effects of Sn addition on as-cast microstructure, mechanical properties and casting fluidity of ZA84 magnesium alloy, Materials & Design 31 (2010), pp. 68-75
38. J. Kubásek, et.al, Structure, mechanical properties, corrosion behavior and cytotoxicity of biodegradable Mg–X (X = Sn, Ga, In) alloys, Materials Science and Engineering: C33 (2013), pp. 2421-2432
39. Inorganic Tin in Drinking-water, Background document for development of WHO for Guidelines Drinking-water Quality (2004),

http://www.who.int/water_sanitation_health/dwq/chemicals/tin.pdf, last accessed, 20.2.2013

40. R. Radha, et.al, Mechanical and corrosion behaviour of hydroxyapatite reinforced Mg-Sn alloy composite by squeeze casting for biomedical applications, Journal of Magnesium and Alloys 8, (2020), pp. 452-460
41. R.G. Li, et.al, Effect of Sn on the microstructure and compressive deformation behavior of the AZ91D aging alloy, Mater Charact, 59 (2008), pp. 1643-1649
42. Qiuyue Yang, et.al, Atomic layer deposited ZrO_2 nanofilm on Mg-Sr alloy for enhanced corrosion resistance and biocompatibility, Acta Biomaterialia 58, (2017), pp. 515-526
43. Ming-Hung Tsai, et.al, Effect of heat treatment on the microstructures and damping properties of biomedical Mg–Zr alloy, Journal of Alloys and Compounds 59, (2011), pp. 813-819
44. H. R. Bakhsheshi-Rad, et.al, Mechanical and bio-corrosion properties of quaternary Mg–Ca–Mn–Zn alloys compared with binary Mg–Ca alloys, Materials & Design 53, (2014), pp. 283-292
45. M. Bobby Kannan, et.al, In vitro degradation and mechanical integrity of calcium-containing magnesium alloys in modified-simulated body fluid, Biomaterials, 29, (2008), pp. 2306-2314
46. Zijian Li, et.al, The development of binary Mg–Ca alloys for use as biodegradable materials within bone, Biomaterials 29, (2008), pp. 1329-1344
47. J.V. Rau, et.al, Hydroxyapatite coatings on Mg-Ca alloy prepared by Pulsed Laser, Deposition: Properties and corrosion resistance in Simulated Body Fluid Ceramics International 44 (2018) pp. 16678–16687
48. K Hirai, et al. Effects of Ca and Sr addition on mechanical properties of a cast AZ91 magnesium alloy at room and elevated temperature, Materials Science and Engineering: 403, (2005), pp. 276-280
49. Shuhua Cai, et.al, Effects of Zn on microstructure, mechanical properties and corrosion behavior of Mg–Zn alloys, Materials Science and Engeenering C 32 (2012) pp. 2570-2577
50. Junxiu Chen, et.al, Mechanical properties of magnesium alloys for medical application: A Review, Journal of the Mechanical Behavior of Biomedical Materials 87 (2018) pp. 68–79
51. Mihriban O.P., et al., Fundamentals of magnesium alloy metallurgy, Woodhead Publishing limited, (2013), ISBN 978-0-85709-088-1 (print), ISBN 978-0-85709-729-3 (online)
52. Larionova, T. V., et.al, A ternary phase observed in rapidly solidified Mg-Ca-Zn alloys. Scripta Materialia 45 (2001) pp.7–12.
53. Bakhsheshi-Rad, et.al, Relationship between the corrosion behavior and the thermal characteristics and microstructure of Mg-0.5Ca-xZn alloys. Corrosion Science 64 (2012) pp.184–97.
54. B. Zberg, et al., MgZnCa glasses without clinically observable hydrogen evolution for biodegradable implants, Nature Materials 8 (2009) 887–891.
55. Mihriban O.P., et al., Fundamentals of magnesium alloy metallurgy, Woodhead Publishing limited, 2013, ISBN 978-0-85709-088-1 (print), ISBN 978-0-85709-729-3 (online)

56. H. Ibrahim et al., “Mechanical and In Vitro Corrosion Properties of a Heat-Treated Mg-Zn-Ca-Mn Alloy as a Potential Bioresorbable Material”, Advances in Metallurgical and Material Engineering, 2017, pp.1-7
57. Q. Chen., et. al., Metallic implant biomaterials, Materials Science and Engineering R 87 (2015) pp.1–57
58. Nurettin Sezer et.al., Review of magnesium-based biomaterials and their applications, Journal of Magnesium and Alloys 6 (2018) pp. 23–43
59. Edward Ghali, Corrosion Resistance of Aluminum and Magnesium Alloys Understanding, Performance, and Testing, John Wiley & Sons, Inc.(2010), ISBN 978-0-471-71576-4
60. Roberge, Pierre R., Handbook of Corrosion Engineering, ISBN 0-07-076516-2, McGraw-Hill Companies (2000).
61. Edited By Philippe Marcus, Corrosion Mechanisms in Theory and Practice Third Edition, CRC Press (2011), ISBN 9780429143564
62. Gerhard Kreysa, et.al., Encyclopedia of Applied Electrochemistry, ISBN 978-1-4419-6995-8, Springer Science+Business Media New York (2014)
63. Mars G. Fontana, Corrosion Engineering, ISBN 0-07-021463-8, McGraw-Hill Companies (1987).
64. E. McCafferty, Introduction to Corrosion Science, ISBN 978-1-4419-0454-6, Springer New York Dordrecht Heidelberg London.
65. M. Pourbaix, Atlas of Electrochemical Equilibria in Aqueous Solutions, National Association of Corrosion Engineers, Houston, TX (1974).
66. Guan Ling Song, Corrosion of magnesium alloys, Woodhead Publishing Limited (2011).
67. Andrej Atrens, et.al., Corrosion mechanism applicable to biodegradable magnesium implants, Materials Science and Engineering: B, 176 (2011) pp. 1609-1636
68. G.L. Song, et. al., Understanding magnesium corrosion: a framework of improved alloy performance, Adv. Eng. Mater. 5 (2003) pp. 837–858
69. G.L. Song, et. al., Corrosion mechanisms of magnesium alloys, Adv. Eng. Mater. 1 (1999) pp. 11–33
70. Ming Liu, et.al., Calculated phase diagrams and the corrosion of die-cast Mg–Al alloys, Corrosion Science 51 (2009) 602-619
71. Sebastián Feliu Jr., et.al., Atmospheric corrosion of magnesium alloys AZ31 and AZ61 under continuous condensation conditions, Corrosion Science, 53 (2011) pp. 1865-1872
72. Jinsun Liao, et.al., Atmospheric corrosion behavior of field-exposed magnesium alloys: Influences of chemical composition and microstructure, Corrosion Science 100 (2015) pp.353 -364
73. Jinsun Liao, Makoto Hotta, Shin-ichi Motoda, Tadashi Shinohara, Atmospheric corrosion of two field-exposed AZ31B magnesium alloys with different grain size, Corrosion Science 71 (2013) 53–61
74. Song G.-L., Control of biodegradation of biocompatible magnesium alloys Corrosion Science 49: (2007) 1696–1701.
75. Song G.-L., Recent Progress in Corrosion and Protection of Magnesium Alloys, Advanced Engineering Materials 7 (2005) 563–586
76. R. Winston Revie, CORROSION AND CORROSION CONTROL. An Introduction to Corrosion Science and Engineering, FOURTH EDITION, ISBN 978-0-471-73279-2, John Wiley & Sons (2008).

77. Nordlien J H, et.al., Morphology and structure of oxide films formed on MgAl alloys by exposure to air and water, Journal of the Electrochemical Society, 142 (1995) pp. 3320–3322
78. Zhiming Shi, et.al., Corrosion resistance of anodised single-phase Mg alloys, Surface & Coatings Technology 201 (2006) 492–503
79. Rosalbino F, et. al., Effect of erbium addition on the corrosion behaviour of Mg–A1 alloys, Intermetallics 13, (2005) pp. 55–60.
80. Zhou X H, et. al., Improvement of corrosion resistance of AZ91D magnesium alloy by holmium addition, Corrosion. Science 48, (2006) pp. 4223–4233.
81. Wu G H, et. al., Differentiation of bone marrow mesenchymal stem cells transplanted into the brain in rats with cerebral infarction and its effect on the recovery of nerve functions, Material Science Engineering A 408, (2005) pp. 255–257.
82. Huang Z H, et.al., Effects of Ce on corrosion resistance of AZ91D magnesium alloy, Acta Metall. Sin. 18, (2005), pp. 129–136.
83. Liu S F, et. al., Using Hajós construction to generate hard graph 3-colorability instances, J. Chin. Earth Soc. 24, (2006), pp. 211–225.
84. Hiba Azzeddine et al. Impact of rare-earth elements on the corrosion performance of binary magnesium alloys, Journal of Alloys and Compounds 829 (2020) 154569
85. Dong Bian, et. al., Design of single-phased magnesium alloys with typically high solubility rare earth elements for biomedical applications: Concept and proof, Bioactive Materials 22 (2023) pp. 180–200
86. Einar Bardal, Corrosion and protection., ISBN: 1-85233-758-3, Springer-Verlag London Berlin Heidelberg (2004).
87. Branko N. Popov, Corrosion Engineering Principles and Solved Problems., ISBN: 978-0-444-62722-3, Copyright © Elsevier B.V. (2015).
88. C. Dilon, Forms of Corrosion: Recognition and Prevention, NACE International, Houston, TX, 1982.
89. Philip A. Schweitzer, Metallic materials. Physical, Mechanical and Corrosion Properties., ISBN: 0-8247-0878-4 Marcel Dekker, Inc. (2003)
90. V. S. Sastri, Green corrosion inhibitors. Theory and Practice, ISBN: 978-1-118-01543-8 John Wiley & Sons, Inc. (2011).
91. F. Czerwinski, Magnesium alloys - Corrosion and Surface Treatments, Edited by Frank Czerwinski, ISBN 978-953-307-972-1, InTech (2011).
92. Kot I., Krawiec H., The use of a multiscale approach in the electrochemistry to study the corrosion behaviour of as – cast AZ91 magnesium alloy, Journal of Solid-State Electrochemistry 19 (2015) pp. 2379 – 2390
93. Dieter Landolt Corrosion and Surface Chemistry, EPFL Press, New York (2007), ISBN9780429146602
94. Bahadori, Alireza, Corrosion and Materials Selection. A Guide for the Chemical and Petroleum Industries, ISBN 978-1-118-86922-2, Wiley (2014).
95. Burstein G.T, et. al., Origin of pitting corrosion, Corrosion Engineering, Science and Technology 39 (2004) 25 – 30.
96. Pistorius P.C., et.al., Growth of corrosion pits on stainless steel in chloride solution containing dilute sulfate, Corrosion Science 33 (1992) pp. 1885 – 1897.
97. Frankel G.S., Pitting corrosion of metals: a review of critical factors, Journal of the Electrochemical Society 145 (1998) 2186 – 2198.

98. Wilde B.E., et. al., The use of current/voltage curves for the study of localized corrosion and passivity breakdown on stainless steels in chloride media, Electrochimica Acta 16 (1971) pp. 1971 – 1985.
99. Wilde B.E., et. al., On the correspondence between electrochemical and chemical accelerated pitting corrosion tests, Journal of the Electrochemical Society 117 (1970) pp. 775 – 779.
100. Szklarska-Smialowska Z., et. al., Electron spectroscopy analysis of in-depth profiles of passive films formed on iron in Cl containing solutions, Corrosion Science 16 (1976) pp. 649 – 652.
101. Frankel G.S., et. al., Metastable pitting of stainless steel, Corrosion 43 (1987) pp. 429 – 436.
102. Baroux B., Further insights on the pitting corrosion of stainless steels, in: P. Marcus (Ed.), Corrosion Mechanism in Theory and Practice, second ed., Marcel Dekker Inc., New York, (2004).
103. Strehblow H.H., Nucleation and reapassivation of corrosion pits for pitting on iron and nickel, Werkstoffe und Korrosion 27 (1976) pp. 792 – 799
104. Wua, H., et. al., Crevice corrosion – A newly observed mechanism of degradation in biomedical magnesium, Acta Biomaterialia, 15 (2019) pp. 152 – 159.
105. Evert D.D. During, Corrosion Atlas. Third, Expended and Revised Edition, ISBN: 978-0-444-64269-1, Copyright © Elsevier B.V. (2018)
106. Cuie Wen, Surface Coating and Modification of Metallic Biomaterials, ISBN 978-1-78242 303-4 (print), ISBN 978-1-78242-316-4 (online) Woodhead Publishing Series in Biomaterials: Number 94, Elsewier,
107. Jingxin Yang, et. al., Plasma surface modification of magnesium alloy for biomedical application, Surface & Coatings Technology 205 (2010) S182-S187, Elsevier
108. Zhi-Ye Qiu, et. al., Advances in the surface modification techniques of bone-related implants for last 10 years, Regenerative Biomaterials, 2014, 67–79, OXFORD
109. Dhaval Makwanaa, P.P.Bhingole, Electrochemical and Plasma Surface Modification of Magnesium and its Alloy: Review, Materials Today: Proceedings 5 (2018) 18260–18267, Elsewier
110. Surface modification of Magnesium and its alloys for Biomedical applications Volume II, Woodhead Publishing Series in Biomaterials: Number, 89 (2015)
111. G.E.J Poinern, et. al., Biomedical magnesium alloys: a review of material properties, surface modifications and potential as biodegradable orthopaedic implant, Journal Biomedical Engineering 2 (2012) pp. 218-240
112. H. Hornberger, et. al., Biomedical coatings on magnesium alloys – a review, Journal Acta Biomaterials, 8 (2012), pp. 2442-2455
113. Z. Panahi, et. al., Surface modification of biodegradable AZ91 magnesium alloy by electrospun polymer nanocomposite: Evaluation of in vitro degradation and cytocompability, Journal Surface and Coatings Technology, 386 (2020) 125461
114. Wei Gan, et. al., Study on surface modification and properties of the AZ91D magnesium alloys used for automobile engine, Journal of Materials Research and Technology, available online 4 May 2020
115. K.Holmberg, A. Matthews, “Coatings Tribology”, Ed.D.Dowson, Tribology Series, 28, Elsevier, 1994

116. Yoshiki Oshida, Surface Engineering and Technology for Biomedical Implants Momentum Press, ISBN: ISBN-13: 978-1-60650-627-1 (2014)
117. Surface modification of biomaterials Methods, Analysis and Applications, Edited by Rachel Williams Woodhead Publishing Limited (2011), ISBN 978-1-84569-640-5 (print) ISBN 978-0-85709-076-8 (online)
118. Harry, J. E. Introduction to plasma technology: Science, engineering and applications. Weinheim, Germany: Wiley-VCH Verlag GmbH & Co. KGaA. (2010).
119. Liston, E. M., et. al., Plasma surface modification of polymers for improved adhesion ± a critical review. Journal of Adhesion Science and Technology, 7, (1993) pp. 1091-1127
120. Friedrich, J. Plasma, the plasma chemistry of polymer surfaces. Weinheim, Germany: Wiley-VCH Verlag GmbH & Co. (2012) KGaA.
121. Wu E. Y., et. al., Enhancement of biocompatibility on bioactive Ti Nb based alloy by high-density plasma modification. Materials Transactions, (2007) 48(12), pp. 3164-3169.
122. Lombardi, A. V., et. al., Survivorship of 2000 tapered titanium porous plasma-sprayed femoral components. Clinical Orthopaedics and Related Research, 467(1), (2009), pp. 146-154
123. Chu, P. K., Bioactivity of plasma implanted biomaterials. Nuclear Instruments and Methods in Physics Research, Section B: Beam Interactions with Materials and Atoms, 242(1-2), (2006) pp. 1-7.
124. Chu, P. K., et. al., Plasma-surface modification of biomaterials. Materials Science and Engineering R: Reports, 36(5-6), (2002) pp. 143-206.
125. Dongdong Zhang, et. al., Protection of magnesium alloys: From physical barrier coating to smart self-healing coating, Journal of Alloys and Compounds, 853 (2021) 157010
126. Mir Saman Safavi, et. al., Electrodeposited Hydroxyapatite-Based Biocoatings: Recent Progress and Future Challenges, Coatings 11, (2021), pp. 1-63
127. K.L. Choy, Chemical vapour deposition of coatings, Progress in Materials Science 48 (2003), pp. 57-170, Elsevier Science Ltd.
128. Mahan, J. E., Physical vapor deposition of thin films. Wily-interscience, (2013), ISBN: 0471-33001. DOI: http://eu.wiley.com/WileyCDA/WileyTitle/productCd-0471330019.html.
129. Peter M. Martin, et. al., Handbook of Deposition Technologies for Films and Coatings, Third Edition: Science, Applications and Technology, William Andrew (2009), pp. 13-14.
130. O. Zaytseva, et. al., Carbon nanomaterials: Production, impact on plant development, agricultural and environmental applications. Chemical and Biological Technologies in Agriculture. 3. (2016)
131. M. Ohring (Ed.), Materials Sciences of Thin Film: Deposition and Structure, Academic Press Ltd., USA, (2002)
132. X. Liu, et. al., Surface modification of titanium, titanium alloys, and related materials for biomedical applications, Materials Science and Engineering, 47 (2004) pp. 49–121.
133. Diederik Depla, Sputter deposition with powder targets: An overview, Vacuum, 184 (2021) 109892.

134. M.V.Shandrikov, et. al., Deposition of Cu-films by a planar magnetron sputtering system at ultra-low operating pressure, Surface and Coatings Technology, 389 (2020), 125600

135. Z. Wang, et.al, Effects of assisting and sputtering ion current on ion beam assisted deposition textured yttria stabilized zirconia buffer layers of coated conductors, Applied Surface Science, 257, (2010) pp.1769-1773

136. F. Zeng, et. al., Ion beam induced grows of amorphous alloy films in Co-Nb system during ion beam assisted deposition, Journal of alloys and Compounds, 335 (2002) pp. 181-187.

137. F.Z. Cui, et. al., Biomaterials modification by ion-beam processing, Surface Coating Technology, (1999), pp. 278-285.

138. L.S. Lee, et.al, Biocompatibility and charge injection property of iridium film formed by ion beam assisted deposition. Biomaterials (2003), pp. 2225-2231.

139. J.X. Yang, et. al., Modification of degradation behavior of magnesium alloy by IBAD coating of calcium phosphate, Surface and Coatings Technology 202 (2008), pp. 5733-5736

140. X. Yao, et. al., Surface modification of biomedical Mg-Ca and Mg-Zn-Ca alloys using selective laser melting: Corrosion behavior, microhardness and biocompability, Journal of Magnesium and Alloys (2020) available online.

141. A. A. Siddiqui, et. al., Optimization of geometrical and mechanical characteristics in laser surface alloying, Materials today: Proceeding (2021) Available online

142. A. A. Siddiqui, et. al., Recent trends in laser cladding and surface alloying, Optics & Laser Technology, 134 (2021), 106619

143. J.V. Rau, et. al., Hydroxyapatite coatings on Mg-Ca alloy prepared by Pulsed Laser Deposition: Properties and corrosion resistance in Simulated Body Fluid, Ceramics International, 44 (2018) pp. 16678-16687

144. R. A. Surmenev, A review of plasma-assisted methods for calcium phosphate-based coatings fabrication," Surface and Coatings Technology (2012) pp.2035–2056.

145. T.S. Hin, Engineering materials for biomedical applications, World Scientific (2004), pp. 6-19, ISBN 981-256-061-0.

146. M. Sankar, et. al., Comparison of electrochemical behavior of hydroxyapatite coated onto WE43 Mg alloy by electrophoretic and pulsed laser deposition, Surface and Coatings Technology, 309 (2017), pp. 840-848.

147. Y. K. Xiao, et. al., Microstructure, heat treatment and mechanical properties of TiB2/Al–7Si–Cu–Mg alloy fabricated by selective laser melting, Materials Science and Engineering 809 (2021), 140951.

148. N. Pulido-González, et. al., High Power Diode Laser (HPDL) surface treatments to improve the mechanical properties and the corrosion behaviour of Mg-Zn-Ca alloys for biodegradable implants, Surface and Coatings Technology, 402 (2020), 126314

149. M. Ali, et. al., Surface modification and cytotoxicity of Mg-based bio-alloys: An overview of recent advances, Journal of Alloys and Compounds, 825 (2020), 154140.

150. R. Maurya, et. al., An environment-friendly phosphate chemical conversion coating on novel Mg-9Li-7Al-1Sn and Mg-9Li-5Al-3Sn-1Zn alloys with remarkable corrosion protection, Applied Surface Science, 443 (2018), pp. 429-440.

151. Y. Song, et. al., Formation mechanism of phosphate conversion film on Mg-8.8Li alloy, Corrosion Science 51 (2009) 62–69.

152. H. Liu, et. al., Preparation of phosphate conversion coating on laser surface textured surface to improve corrosion performance of magnesium alloy, Journal of Alloys and Compounds 865 (2021) 158701.
153. X.C. Zhao, et. al., Ultrasonic induced rapid formation and crystal refinement of chemical conversed hopeite coating on titanium, Physical Chemistry, 118 (2014), pp. 1910-1918.
154. D. B. Prabhu, et. al., Morphological studies on the development of chemical conversion coating on surface of Mg–4Zn alloy and its corrosion and bio mineralization behaviour in simulated body fluid, Journal of Alloys and Compounds, 812, (2020), 152146.
155. R. C. Alkire, et. al., Electrochemical Surface Modification Thin Films Functionalization and Characterization, Wiley (2008), ISBN 978-3-527-31419-5.
156. A. Bahatibieke, et. al., In vivo and in simulated body fluid degradation behavior and biocompatibility evaluation of anodic oxidation-silane-chitosan-coated Mg-4.0Zn-0.8Sr alloy for bone application, Materials Science & Engineering C 120 (2021) 111771.
157. L. Mohan, et. al., Formation of nanostructures on magnesium alloy by anodization for potential biomedical applications, Materials today communications 25, (2020), 101403.
158. Yu-Lian Lai, et. al., Electrolytic deposition of hydroxyapatite/calcium phosphate-heparin/gelatin-heparin tri-layer composites on NiTi alloy to enhance drug loading and prolong releasing for biomedical applications, Thin Solid Films 649, (2018), pp. 192-201.
159. H. Sampatirao, et. al., Developments in plasma electrolytic oxidation (PEO) coatings for biodegradable magnesium alloys, Materials Today: Proceedings (2021).
160. R. Manoj Kumar, et. al., Electrophoretic deposition of hydroxyapatite coating on Mg–3Zn alloy for orthopaedic application, Surface and Coatings Technology 287, (2016), pp. 82-92.
161. R. Rojaee, et. al., Electrophoretic deposition of bioactive glass nanopowders on magnesium based alloy for biomedical applications, Ceramics International 40/6, (2014), pp. 7879-7888.
162. F. Gebhardt, et. al., Characterization of electrophoretic chitosan coatings on stainless steel, Materials Letters, 66 (2012), pp. 302-304.
163. S. Singh, et. al., Corrosion behavior and characterization of HA/Fe_3O_4/CS composite coatings on AZ91 Mg alloy by electrophoretic deposition, Materials Chemistry and Physics 237 (2019), 121884.
164. I. Narkevica, et. al., Electrophoretic deposition of nanocrystalline TiO_2 particles on porous TiO2-x ceramic scaffolds for biomedical applications, Journal of the European Ceramic Society 37, (2017), pp. 3185-3193.
165. G.Chandra, et. al., Preparation Strategies for Mg-alloys for Biodegradable Orthopaedic Implants and Other Biomedical Applications: A Review, IRBM
166. Robert B. Heimann, Magnesium alloys for biomedical application: Advanced corrosion control through surface coating, Surface & Coatings Technology 405 (2021) 126521.
167. Matheus S. Gularte, et. al., Synthesis of chitosan derivatives with organoselenium and organosulfur compounds: Characterization, antimicrobial properties and application as biomaterials, Carbohydrate Polymers (2019), S0144-8617(19)30545-4.

168. Rahimi, M., et. al., Improving biocompatibility and corrosion resistance of anodized AZ31 Mg alloy by electrospun chitosan/mineralized bone allograft (MBA) nanocoatings. Surf. Coat. Technol. 2021, 405, 126627.

169. Yang Chen, et. al., Layer by layer assembled chitosan (TiO2)-heparin composite coatings on MAO-coated Mg alloys, Materials Letters 281 (2020) 128640.

170. Abdel Salam Hamdy Makhlouf Nedal Y. Abu-Thabit Stimuli, Responsive Polymeric Nanocarriers for Drug Delivery Applications Advanced Nanocarriers for Therapeutics.

171. Egemen Avcua, et. al., Electrophoretic deposition of chitosan-based composite coatings for biomedical applications: A review, Progress in Materials Science 103 (2019) 69–108

172. Crini G, et. al., Application of chitosan, a natural aminopolysaccharide, for dye removal from aqueous solutions by adsorption processes using batch studies: a review of recent literature. Prog Polym Sci 33(2008) 399–447.

173. El Kadib A. Chitosan as a sustainable organocatalyst: a concise overview. Chem Sus Chem 8 (2015) 217–44.

174. V.K. Mourya, et. al., Chitosan-modifications and applications: Opportunities galore, Reactive and Functional Polymers 68 (2008) 1013-1051.

175. Agata Sotniczuk, et. al., Chitosan/bioactive glass coatings as a protective layer against corrosion of nanocrystalline titanium under simulated inflammation, Materials Letters 264 (2020) 127284

176. S.N. Pleskova, et. al., Bactericidal activity of titanium dioxide ultraviolet-induced films, Mater. Sci. Eng., C 59 (2016) 807–817.

177. Giuseppe Perale and Jons Hilborn, Bioresorable Polymers for Biomedical applications, From Fundamentals to Translational Medicine Woodhead Publishing Series in Biomaterials: Number 120 2017, ISBN: 978-0-08-100262-9 (print), ISBN: 978-0-08-100266-7 (online)

178. https://pubchem.ncbi.nlm.nih.gov/compound/Stearic-Acid

179. Paurnima Talele et.al., Hydroquinone loaded solid lipid nanoparticles comprised of stearic acid and ionic emulsifiers: Physicochemical characterization and in vitro release study, Journal of Molecular Liquids, Volume 368, Part A, 15 (2022), 120590

180. Patrícia Severino et. al., Polymorphism, crystallinity and hydrophilic–lipophilic balance of stearic acid and stearic acid–capric/caprylic triglyceride matrices for production of stable nanoparticles, Colloids and Surfaces B: Biointerfaces, Volume 86, (2011), 125-130

181. Antonella Patti et. al., The universal usefulness of stearic acid as surface modifier: applications to the polymer formulations and composite processing, Journal of Industrial and Engineering Chemistry 96, (2021), 1-33

182. Ng W. F, Stearic acid coating on magnesium for enhancing corrosion resistance in Hank's solution, Surface and Coatings Technology 204 (2010) 1823 – 1830.

183. Zhifeng Huang et. al., Stearic acid modified porous nickel-based coating on magnesium alloy AZ31 for high superhydrophobicity and corrosion resistance, Corrosion Communications 10 (2023), 38-47

184. S. Karnnet et. al., Preparation and properties of biodegradable stearic acid-modified gelatin films, Polymer Degradation and Stability Volume 90, Issue 1, October 2005, Pages 106-110

185. Xin Li, Ultrasonic treatment regulates the properties of gelatin emulsion to obtain high-quality gelatin film, Food Chemistry (18) 2023 100673
186. Sapna Sethi et. Al., A review on chitosan-gelatin nanocomposites: Synthesis, characterization and biomedical applications, Reactive and Functional Polymers 179, (2022), 105362
187. Xu X, et. al., Cross-linked gelatin/nanoparticles composite coating on micro-arc oxidation film for corrosion and drug release, Applied Surface Science 256 (2010) 2367 – 2371
188. Rui L. Reis et.al., Natural-based polymers for biomedical applications, Woodhead Publishing Limited (2008), ISBN 978-1-84569-481-4 (e-book)
189. I.A.Kurzina, et, al., Surface property modification of biocompatible material based on polylactic acid by ion implantation, Surface and Coatings Technology 388 (2020).
190. Amirouche Bouamer, et. al., Characterization of polylactic acid ceramic composites synthesized by casting method, Materials today: Proceeding Volume 42, Part 5, 2021, Pages 2959-2962
191. Volova, T. G. et.al., NATURAL-BASED POLYMERS FOR BIOMEDICAL APPLICATIONS, Apple Academic Press, (2017), ISBN 978-1-315-36603-6 (PDF)
192. Xian Jun Loh, In-Situ Gelling Polymers For Biomedical Applications, Springer (2015), ISBN 978-981-287-152-7 (eBook)
193. Alabbasi A, et. al., Polylactic acid coating on biodegradable magnesiu alloy: an in vitro degradation study by electrochemical impedance spectroscopy, Thin Solid Films 520 (2012) 6841 – 6844
194. Sangamesh Kumbar, et.al., Natural and Synthetic Biomedical Polymers, Elsevier Science (2014), ISBN:9780123972903, ISBN:0123972906
195. Roger Narayan, Encyclopedia of Biomedical Engineering, Elsevier (2019), ISBN 9780128051443, ISBN 0128051442
196. Paul Ducheyne, et.al., Comprehensive biomaterials II, Elsevier (2017), ISBN:9780081006924, ISBN: 0081006926
197. Laurence W. McKeen, The Effect of Long Term Thermal Exposure on Plastics and Elastomers, Second Edition, William Andrew Publishing (2021), ISBN 978-0-323-85436-8
198. Ashok Pandey et.al., Current developments in biotechnology and bioengineering: production, isolation and purification of industrial products, Elsevier (2017), ISBN 978-0-444-63662-1
199. Fereshteh Sharifi, et.al., Polycaprolactone/carboxymethyl chitosan nanofibrous scaffolds for bone tissue engineering application, International Journal of Biological Macromolecules 115, (2018), pp. 243-248
200. Miroslav Huskić, et.al., The synthesis and characterization of multiarm star-shaped graft copolymers of polycaprolactone and hyperbranched polyester, European Polymer Journal 70, (2015), pp. 384-391
201. Beom-SuKim, et.al., Incorporation of BMP-2 nanoparticles on the surface of a 3D-printed hydroxyapatite scaffold using an ε-polycaprolactone polymer emulsion coating method for bone tissue engineering, Colloids and Surfaces B: Biointerfaces 170, (2018), pp. 421-429

202. Julia Degner, et.al., Electrochemical investigations of magnesium in DMEM with biodegradable polycaprolactone coating as corrosion barrier, Applied Surface Science 282, (2013), pp. 264-270

203. Susmita Bose, et.al., Effects of polycaprolactone on alendronate drug release from Mg-doped hydroxyapatite coating on titanium, Materials Science and Engineering: C 88, (2018), pp. 166-171

204. Geng Wu, et.al., Enhanced biological properties of biomimetic apatite fabricated polycaprolactone/chitosan nanofibrous bio-composite for tendon and ligament regeneration, Journal of Photochemistry and Photobiology B: Biology 178 (2018), Pages 27-32

205. Nasiruddin Usmaniya et. al., Effect of polycaprolactone coating on the corrosion and biological characteristics of plasma electrolytic oxidised ZM21 magnesium alloy, Surface and Coatings Technology 471 (2023), 129915

206. Bin Lin et. al., Microstructure, corrosion behavior and hydrogen evolution of USSP processed AZ31 magnesium alloy with a surface layer containing amorphous Fe-rich composite, International Journal of Hydrogen Energy Available online 21 January 2021, Elsevier

207. Song, G., et. al., An hydrogen evolution method for the estimation of the corrosion rate of magnesium alloys, New Orlean

208. B. Stypuła, M. Starowicz, M. Hajos, E. Olejnik, Electrochemical synthesis of ZnO nanoparticles during anodic dissolution of zinc in alcohols solvents, Archives of Metallurgy and Materials 56 (2011) 287–292

209. Maria Starowicz, Barbara Stypuła, Jacek Banaś, Electrochemical synthesis of silver nanoparticles, Electrochemistry Communications 8 (2006) 227–230

210. Kozina, I.; Krawiec, H.; Starowicz, M.; Kawalec, M. Corrosion Resistance of MgZn Alloy Covered by Chitosan-Based Coatings. Int. J. Mol. Sci. 2021, 22, 8301.

211. H. Krawiec, I. Kozina, M Starowicz, et al. Corrosion Rate and Mechanism of Degradation of Chitosan/TiO_2 Coatings Deposited on MgZnCa Alloy in Hank's Solution, Int. J. Mol. Sci. 2024, 25(10), 5313

212. J.R. Deepak, et. al., XRD investigation of biodegradable magnesium rare earth alloy, Materials Today, Proceedings 47 (2021) 4676 – 4681

213. Andrea Gil-Santos, et. al., Microstructure and mechanical characterization of cast Mg-Ca-Si alloys, Journal of Alloys and Compounds 694 (2017) 767 - 776

214. Clemens Burda, et. al., Enhanced Nitrogen Doping in TiO2 Nanoparticles, Nano Letters, 3 (no. 8) (2003), 1049 – 1051

215. Pawlak, A., et. al., Thermogravimetric and FTIR studies of chitosan blends. Thermochim. Acta 2003, 396, 153-166.

216. A.Leon, et. al., FTIR and Raman Characterization of TiO2 Nanoparticles Coated with Polyethylene Glycol as Carrier for 2-Methoxyestradiol, Appl. Sci. 2017, 7, 49

217. Mehrnaz Gharagozlou, Sanaz Naghibi, Preparation of vitamin B12–TiO_2 nanohybrid studied by TEM, FTIR and optical analysis techniques, Materials Science in Semiconductor Processing, 35 (2015) 166-173

218. Y. Xing, et. al., Effects of different TiO_2 nanoparticles concentrations on the physical and antibacterial activities of chitosan-based coating film, Nanomaterials, 10 (2020), p. 1365

219. Elham M. Hussein, et. al., Effect of TiO_2 nanoparticles on the structural configurations and thermal, mechanical, and optical properties of chitosan/TiO2 nanoparticle composites, Journal of Physics and Chemistry of Solids, 152 (2021) 109983

220. Bobrowski, A., et. al., FTIR spectroscopy of water glass–the binder moulding modified by zno nanoparticles. Metalurgija 2012, 51, 477–480.

221. Ma, J. et. al., Textural and structural studies of sol–gel derived SiO2–CaO–P2O5–MgO glasses by substitution of MgO for CaO. Mater. Sci. Eng. C 2012, 30, 886–890.

222. Bobrowski, A., et. al., Effect of Magnesium Oxide Nanoparticles on Water Glass Structure, Arch. Found. Eng. 2012, 12, 9–12.

223. Wu. C., et. al., Fabrication of calcium phosphate/chitosan coatings on AZ91D magnesium alloy with a novel method. Surf. Coat. Technol. 2010, 204, 3336–3347.

224. Rodrigo S. Vieira, et. al., Copper, mercury and chromium adsorption on natural and crosslinked chitosan films: An XPS investigation of mechanism, Colloids and Surfaces A: Physicochem. Eng. Aspects 374 (2011) 108–114

225. Yao, W., et. al., Effect of Zn^{2+} and its addition sequence on flotation separation of scheel-ite from calcite using water glass. Colloids Surf. A Physicochem. Eng. Asp. 2020, 588, 124394.

226. XPS data base. Available online: https://srdata.nist.gov/xps. (30.07.2021).

227. Kiran, John, U. et. al., XPS and thermal studies of silver doped SiO2 matrices for plasmonic applications. Mater. Today Proc. 2020, 33, 1263–1267.

228. Kazek-Kęsik, A., et. al., Influence of Alkali Treatment on Anodized Titanium Alloys in Wollastonite Suspension. Metals 2017, 7, 322.

229. Hong Wang, et. al., Nitrogen-doped TiO2 nanoparticles better TiO2 nanotube array photo-anodes for dye sensitized solar cells, Electrochimica Acta 137 (2014) 744-750

230. Zhang Y. at al. In situ growth of Sn nanoparticles confined carbon-based TiO2 /TiN composite with long-term cycling stability for sodium-ion batteries, Electrochimica Acta 367 (2021) 137450

231. M.V. Kuznetsov, et. al., XPS study of the nitrides, oxides and oxynitrides of titanium, J. Electron Spectros. Relat. Phenomena 58 (1992) 1–9.

232. Katja Andrina Kravanja et al., The synthesis, surface analysis, and cellular response of titania and titanium oxynitride nanotube arrays prepared on TiAl6V4 for potential biomedical applications, Journal of Materials Research and Technology 24 (2023) 4074-4090

233. S. Fajardo, et.al., Corrosion resistance of pulsed laser modified AZ31 Mg alloy surfaces, J. Magnes. Alloy. 10 (2022) 756–768

234. Q. Zou, et.al., The influence of Ga alloying on Mg-Al-Zn alloys as anode material for Mg-air primary batteries, Electrochim. Acta 401 (2022) 139372

235. Z. Li, et.al., Abnormal Blood Glucose Concentration on Degradation Behavior of AZ31 Magnesium Alloy, Chem. Res. Chinese Universities, 2020, 36(6), 1217—1226

236. S. Shetty, et.al., Influence of sulfate ion concentration and pH on the corrosion of Mg-Al-Zn-Mn (GA9) magnesium alloy, J. Magnes. Alloy. 3 (2015) 258–270

237. N. Wang, et. al., Discharge behaviour of Mg-Al-Pb and Mg-Al-Pb-In alloys as anodes for Mg-air battery, Electrochim. Acta 149 (2014) 193–205

238. S. Li, et.al., Effects of Ca addition on microstructure, electrochemical behavior and magnesium-air battery performance of Mg-2Zn-xCa alloys, J. Electroanal. Chem. 904 (2022) 115944

239. E. Ghali, et.al., Testing of general and localized corrosion of magnesium alloys: A critical review. J. Mater. Eng. Perform. 2004, 13, 517-529

240. S.W. Ha, et.al., Surface activation of polyetheretherketone (PEEK) and formation of calcium phosphate coatings by precipitation, J. Mater. Sci. Mater. Med. 8 (1997) 683–690

241. J.L. Ong, et.al., Osteoblast precursor cell activity on HA surfaces of different treatments, J. Biomed. Mater. Res. 39 (1998) 176–183

242. J.L. Ong, et.al., Surface characterization of ion-beam sputter-deposited Ca-P coatings after in vitro immersion, Colloids Surfaces A Physicochem. Eng. Asp. 87 (1994) 151–162

243. J.G. Acheson, et.al., TOFSIMS and XPS characterisation of strontium in amorphous calcium phosphate sputter deposited coatings, Mater. Charact. 171 (2021) 110739

244. S.A. Omar, et.al., Micro Raman and XPS surface analysis to understand the electrochemical behaviour of AZ31 and AZ91 magnesium alloys as temporary implant materials, Mater. Today Commun. 31 (2022) 103557

245. Jarnail Singh, et.al., Characterization and corrosion behavior of plasma sprayed calcium silicate reinforced hydroxyapatite composite coatings for medical implant applications. Ceram. Int. 2021, 47, 782–792.

246. G. Geisberger, E.B. Gyenge, C. Maake, G.R. Patzke, Trimethyl and carboxymethyl chitosan carriers for bio-active polymer–inorganic nanocomposites, Carbohydr. Polym. 91 (2013) 58–67.

247. V. Patrulea, L.A. Applegate, V. Ostafe, O. Jordan, G. Borchard, Optimized synthesis of O-carboxymethyl-N,N,N-trimethyl chitosan, Carbohydr. Polym. 122 (2015) 46–52.

248. T. Xu, M. Xin, M. Li, H. Huang, S. Zhou, Synthesis, characteristic and antibacterial activity of N,N,N-trimethyl chitosan and its carboxymethyl derivatives, Carbohydr. Polym. 81 (2010) 931–936.

249. Z.J. Fan, B. Liu, J.Q. Wang, S.Y. Zhang, Q.Q. Lin, P.W. Gong, L.M. Ma, S.R. Yang, A novel wound dressing based on Ag/graphene polymer hydrogel: effectively kill bacteria and accelerate wound healing, Adv. Funct. Mater. 24 (2014) 3933–3943.

250. F. Wahid, H.-S. Wang, C. Zhong, L.-Q. Chu, Facile fabrication of moldable antibacterial carboxymethyl chitosan supramolecular hydrogels cross-linked by metal ions complexation, Carbohydr. Polym. 165 (2017) 455–461.

251. W. Dong, B. Han, Y. Feng, F. Song, J. Chang, H. Jiang, Y. Tang, W. Liu, Pharmacokinetics and biodegradation mechanisms of a versatile carboxymethyl derivative of chitosan in rats: in vivo and in vitro evaluation, Biomacromolecules 11 (2010) 1527–1533.

252. Soheila Rahmani at al., Methylated 4-N,N dimethyl aminobenzyl N,O carboxymethyl chitosan as a new chitosan derivative: Synthesis, characterization, cytotoxicity and antibacterial activity, Carbohydrate Polymers 149 (2016) 131-139

253. Mark P. Staigera, Alexis M. Pietak, Jerawala Huadmai, George Dias, Magnesium and its alloys as orthopedic biomaterials: A review; Biomaterials 27 (2006) 1728-1734, Elsevier

254. Ping-Li Jiang, Rui-Qing Hou, Cheng-Dong Chen, Lan Sun, Shi-Gang Dong, Jin-Shan Pan, Controllable degradation of medical magnesium by electrodeposited composite

films of mussel adhesive protein (Mefp-1) and chitosan, Journal of Colloid and Interface Science 478 (2016) 246-255

255. R. Kumar, A. Umar, G. Kumar, H.S. Nalwa, Antimicrobial properties of ZnO nanomaterials: a review, Ceramics International 43 (2017) 3940–3961
256. N. Jones, B. Ray, K.T. Ranjit, A.C. Manna, Antibacterial activity of ZnO nanoparticle suspensions on a broad spectrum of microorganisms, FEMS Microbiology Letters 279 (2008) 71–76
257. C. Guo, Z. Zheng, Q. Zhu, X. Wang, Preparation and characterization of polyurethane/ZnO nanoparticle composite, Polymer-Plastics Technology and Engineering 46 (2007) 1161 – 1166
258. H.R. Bakhsheshi-Rad, E. Hamzah, In vitro corrosion behavior, bioactivity, and antibacterial performance of the silver-doped zinc oxide coating on magnesium alloy, Mater. Corros. 8 (2017) 1228–1236.
259. H.R. Bakhsheshi-Rad, E. Hamzah, Synthesis of a novel nanostructured zinc oxide/baghdadite coating on Mg alloy for biomedical application: in-vitro degradation behavior and antibacterial activities, Ceram. Int. 43 (2017) 14842–14850.
260. Dongwei Wei, Wuyong Sun, Weiping Qian, Yongzhong Ye, Xiaoyuan Ma, The synthesis of chitosan-based silver nanoparticles and their antibacterial activity, Carbohydrate Research, 344, (2009) 2375-2382
261. J. Betzabé González-Campos et al. New insights into the bactericidal activity of chitosan-Ag bionanocomposite: The role of the electrical conductivity, Colloids and Surfaces B: Biointerfaces 111 (2013) 741– 746
262. Sensitivity of ESBL-Producing Gram-Negative Bacteria to Essential Oils, Plant Extracts, and Their Isolated Compounds Gy. Horváth, ... B. Kocsis, in Antibiotic Resistance, 2016
263. Tendencia, E. A. (2004). Disk diffusion method. In Laboratory manual of standardized methods for antimicrobial sensitivity tests for bacteria isolated from aquatic animals and environment (pp. 13-29). Tigbauan, Iloilo, Philippines: Aquaculture Department, Southeast Asian Fisheries Development Center.
264. https://asm.org/getattachment/2594ce26-bd44-47f6-8287-0657aa9185ad/Kirby-Bauer-Disk-Diffusion-Susceptibility-Test-Protocol-pdf.pdf (10.11.2023)
265. Characterization of silver nanoparticles synthesized using Urtica dioica Linn. leaves and their synergistic effects with antibiotics.